

Magnetic Proximity Effects in Highly-ordered Transition Metal Oxide Heterosystems studied by Soft X-Ray Photoemission Electron Microscopy

Vom Fachbereich Physik der Universität Duisburg-Essen
zur Erlangung des akademischen Grades eines
Doktors der Naturwissenschaften (Dr. rer. nat.)
genehmigte Dissertation

von

Ingo Peter Krug

aus

St. Wendel

Referent: PROF. DR. CLAUS M. SCHNEIDER

Korreferent: PROF. DR. HEIKO WENDE

Tag der Einreichung: 18.10.2007

Tag der mündlichen Prüfung: 21.02.2008

Thesis Supervisors:

Prof. Dr. Franz Ulrich Hillebrecht & Prof. Dr. Claus M. Schneider

in memoriam Franz Ulrich Hillebrecht, † 08/08/2006

to his wife and children in deep compassion for the great loss

Abstract

In this thesis, the magnetic proximity effect (MPE) in highly-ordered transition metal oxide (TMO) heterosystems composed of single crystals of ferrimagnetic (FIM) Fe_3O_4 and thin antiferromagnetic (AF) NiO layers has been investigated by Photoelectron Emission Microscopy using polarized soft x-rays (X-PEEM). The systems have been prepared *in-situ* by Molecular Beam Epitaxy on single crystalline Fe_3O_4 substrates polished to various crystallographic surface orientations and conditioned by Ar sputtering and annealing in O_2 background. The magnetic order was determined by vectorial magnetometry exploiting XMCD and anisotropic XMLD for single crystalline systems of cubic symmetry.

Two major contributions to the MPE were identified: First, short-ranged interfacial exchange interactions create an ultrathin zone of altered magnetic structure near the interface. Second, long-ranged magnetoelastic interactions lead to a change of the magnetic structure on a larger scale, affecting the whole NiO ad-layer. The influence of directional lattice strain on the magnetic order via magnetoelastic coupling was studied by means of samples with different crystallographic interface orientations. The strain appears to affect the AF stacking-directions in NiO as well as the coupling behaviour at the NiO/ Fe_3O_4 interface. Additionally, the in-plane bonding anisotropy of the films leads to variations of the uncompensated magnetization induced in the NiO AF layer via exchange coupling. It was found, that the uncompensated magnetization resides directly at the interface, and the bulk of the NiO layers is compensated. XMCD sum-rule analysis of a NiO wedge on Fe_3O_4 (110) revealed extremal values for the Fe and Ni orbital moments for 1 ML, possibly related to the reconstruction of the interface layer to NiFe_2O_4 . Temperature-dependent measurements of the XMD contrast reveal lowered critical temperatures for both NiO and Fe_3O_4 due to finite size effects and interfacial coupling.

Fits of the theoretically expected XMLD contrast to profiles of the exchange-induced AF domain walls yielded a wall structure consistent with a simple coherent in-plane rotation model of the NiO spin-axis. In magnetically-annealed samples, the anisotropy of the Fe_3O_4 (110)/NiO interface was found to be altered, leading to non-crystallographic easy-axes. In a simple picture, the effect may be explained as a superposition of bulk and interfacial magnetocrystalline and magnetoelastic anisotropies. A highly-ordered Fe_3O_4 (110)/NiO[51 Å]/Co[15 Å] trilayer-system was found to exhibit the same composite anisotropy as mentioned before, and in addition a possibly roughness-driven perpendicular interlayer coupling between Co and Fe_3O_4 .

Zusammenfassung

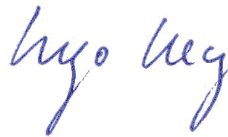
In dieser Arbeit wurde der Magnetische Proximitätseffekt in hochgeordneten Übergangsmetalloxid-Heterosystemen bestehend aus ferrimagnetischen (FIM) Fe_3O_4 Einkristallen und dünnen antiferromagnetischen (AF) NiO Schichten mittels Weichröntgen-Photoemissions-Elektronenmikroskopie untersucht. Die Schichtsysteme wurden *in-situ* mittels Molekularstrahlepitaxie auf einkristallinen Fe_3O_4 -Substraten hergestellt, welche durch Ar-Sputtern und Tempern in Sauerstoff vorbereitet wurden. Die magnetische Ordnung wurde mittels vektorieller Magnetometrie unter Ausnutzung des Magnetischen Zirkulardichroismus (XMCD) und des anisotropen Lineardichroismus (XMLD) bestimmt.

Zwei Hauptbeiträge zum Magnetischen Proximitätseffekt konnten identifiziert werden: Erstens wird durch kurzreichweitige Austauschwechselwirkung eine ultradünne Zone veränderter magnetischer Struktur nahe der Grenzfläche induziert. Zweitens führen magnetoelastische Wechselwirkungen zu einer Veränderung der magnetischen Ordnung auf größerer Skala, wodurch meist die gesamte NiO Schicht betroffen ist. Der Einfluss gerichteter Gitterverzerrungen auf den Magnetismus mittels magnetoelastischer Kopplung wurde an Hand von Proben mit verschiedenen kristallographischen Grenzflächenorientierungen untersucht. Die Verzerrung scheint sowohl die AF Stapelrichtungen in NiO als auch das Kopplungsverhalten an der Fe_3O_4 /NiO Grenzfläche zu beeinflussen. Des weiteren führt die Bindungsanisotropie in der Grenzflächenebene zu Variationen der durch den Grenzflächenaustausch induzierten unkompensierten Magnetisierung in NiO. Ferner wurde beobachtet, dass die unkompensierte Ni-Magnetisierung direkt an der Grenzfläche lokalisiert ist, während das Innere der NiO Schichten kompensiert ist. Analyse der XMCD Summenregeln in einem NiO-Keil auf Fe_3O_4 (110) zeigte extremale Werte für das Fe- und Ni- Bahnmoment für etwa 1 ML Schichtdicke, möglicherweise in Verbindung mit der Rekonstruktion der Grenzflächenlage zu NiFe_2O_4 . Temperaturabhängige Messungen des dichroischen Kontrastes zeigen erniedrigte kritische Temperaturen sowohl für NiO als auch für Fe_3O_4 , in Folge von Finite-Size Effekten und Grenzflächenaustauschkopplung.

Fits des theoretisch erwarteten XMLD Kontrastes an Linienprofile der austauschinduzierten AF Domänenwände in NiO ergaben, dass die Wandstruktur konsistent ist mit einem einfachen Modell einer kohärenten Spinachsenrotation in der Schichtebene. In magnetisch getemperten Proben wurde eine veränderte Anisotropie der Fe_3O_4 (110)/NiO Grenzfläche festgestellt, welche nichtkristallographische leichte Achsen aufwies. In einem einfachen Modell könnte dieser Effekt als eine Überlagerung von Volumen- und Grenzflächenanisotropien magnetokristalliner und magnetoelastischer Natur angesehen werden. Schließlich wurde in einem Fe_3O_4 (110)/NiO[51 Å]/Co[15 Å] Dreifachschichtsystem die gleiche zuvor erwähnte Gesamtanisotropie gefunden, zusätzlich jedoch eine möglicherweise rauhgkeitsinduzierte senkrechte Zwischenschichtkopplung von Cobalt und Fe_3O_4 .

Erklärung

Ich versichere, dass ich die von mir vorgelegte Dissertation selbständig angefertigt, die benutzten Quellen und Hilfsmittel vollständig angegeben habe. Ferner versichere ich, dass ich die anderen Werken dem Sinn oder Wortlaut nach entnommenen Textpassagen, Abbildungen oder Tabellen in jedem Einzelfall kenntlich gemacht habe; dass dieser Promotion kein erfolgloser Promotionsversuch vorausging und dass diese Dissertation noch keiner Fakultät oder Universität zur Prüfung vorgelegen hat; dass sie – abgesehen von den angegebenen Teilpublikationen – noch nicht veröffentlicht worden ist sowie, dass ich eine solche Veröffentlichung vor Abschluss des Promotionsverfahrens nicht vornehmen werde. Die Bestimmungen der Promotionsordnung sind mir bekannt. Die von mir vorgelegte Dissertation ist von Prof. Dr. Claus Michael Schneider betreut worden.



Ingo Krug

Contents

Introduction	xv
I. Theoretical and Experimental Background	1
1. Magnetic spectroscopy using X-rays	3
1.1. Classical description of absorption and magneto-optical phenomena	3
1.1.1. Absorption	3
1.1.2. Dielectric tensor and optical effects	4
1.1.3. Link between electrodynamics and quantum mechanics - the Kubo-formula	8
1.2. X-ray absorption spectroscopy (XAS) and its application to mag- netism	9
1.2.1. The x-ray absorption process	9
2. Dichroism	11
2.1. Circular Dichroism	11
2.1.1. X-ray natural circular dichroism (XNCD)	11
2.1.2. X-ray magnetic circular dichroism (XMCD)	11
2.1.3. XMCD sum rules – charge, orbital- and spin-moment	15
2.2. Linear Dichroism	18
2.2.1. Introduction and Terminology	18
2.2.2. X-ray Natural Linear Dichroism (XNLD)	19
2.3. X-ray Magnetic Linear Dichroism (XMLD)	21
2.3.1. X-ray Magnetic Linear Dichroism by exchange-correlation effects	21
2.3.2. XMLD in the presence of orbital degrees of freedom	23
2.3.3. "Anisotropic" XMLD in 3d transition metal compounds . .	25
2.3.4. Angular dependence of XMLD - a phenomenological de- scription	28
2.3.5. "Isotropic" XMLD	29
2.3.6. "Anisotropic" XMLD in cubic symmetry	31

3. Transition Metal Oxides - Electronic and magnetic properties	35
3.1. NiO: Electronic structure and magnetic interactions	35
3.2. Antiferromagnetic structure and magnetoelastic domains in NiO .	36
3.2.1. Antiferromagnetic Domain walls	37
3.3. Fe ₃ O ₄ : Electronic and magnetic structure	39
4. Experimental Methods	41
4.1. Generation of polarized x-rays – synchrotron radiation	41
4.2. Photoemission microscopy using soft x-rays	42
5. Magnetic Proximity Effect and Related Phenomena	47
5.1. Interfacial exchange coupling and exchange bias	48
5.1.1. Models and their limits	48
II. Experimental results	57
6. Proximity effect in Fe₃O₄ (110)/NiO	59
6.1. Introduction	59
6.2. Sample preparation	59
6.3. Vectorial magnetometry using PEEM microspectroscopy	61
6.3.1. Determination of the substrate magnetization map	62
6.3.2. Coupling of the interfacial Ni-moments to Fe ₃ O ₄	64
6.3.3. Orientation of the spin-axis in NiO – determination of the coupling type	67
6.3.4. Ultrathin proximity zone at the interface	77
6.4. Temperature-dependence of the magnetic contrast	82
6.4.1. Introduction	82
6.4.2. Experimental procedure	82
6.5. Summary	87
7. Influence of interface orientation on the coupling type	89
7.1. Introduction	89
7.2. Sample preparation	90
7.2.1. Substrate and interface conditioning	91
7.2.2. NiO deposition by MBE	96
7.3. Experimental results	97
7.3.1. (110)-interface	97
7.3.2. (001)-interface	97
7.3.3. (111)-interface	101
7.3.4. Amount of uncompensated magnetization in the three ori- entations	101

7.4. Discussion of the results	104
7.4.1. Magnetoelastic influence on the coupling type	104
7.4.2. Amount of uncompensated magnetization	109
7.5. Summary and Conclusion	109
8. Tailoring antiferromagnetic domain walls and anisotropy	111
8.1. Motivation	111
8.2. Results of the fitting process	113
8.3. Origin of the perpendicular FM orientation	120
8.4. Summary	123
9. Conclusions and Outlook	125
A. Appendix	129
A.1. Epitaxial strain and magnetoelastic distortions in different inter- face orientations of the $\text{Fe}_3\text{O}_4/\text{NiO}$ system	129
A.1.1. Epitaxial strain of the NiO layer	129
A.1.2. Magnetoelastic coupling	130
A.2. Confusion and conversion – the SI and CGS systems	132
Danksagung	151
Curriculum Vitae	155

List of Figures

1.1. influence of exchange and correlation – multiplets	10
2.1. On the XMCD transition intensities	12
2.2. About the XMCD sum rules	17
2.3. Crystal field splitting in cubic symmetry	19
2.4. Crystal field splitting in tetragonal symmetry	20
2.5. XNLD in strained NiO	20
2.6. p-and d-orbitals: Nodal features	21
2.7. On the XMLD transition intensities	23
2.8. 3d High-spin configurations in cubic symmetry	25
2.9. XMLD: Fundamental spectra	32
2.10. Anisotropic XMLD for several spin-quantization axes	34
3.1. 180° superexchange interaction.	35
3.2. NiO AF structure	36
3.3. Antiferromagnetic domains in NiO	37
3.4. NiO AF structure	38
3.5. Crystal structure of magnetite	40
4.1. Energy spread of secondary electrons and PEEM transmission	43
4.2. PEEM	44
5.1. Exchange-bias: Various scenarios	51
5.2. Spin-flop coupling: transversal instability	53
6.1. Stoichiometry of Magnetite	61
6.2. R-factor for the determination of the vectormap	63
6.3. Magnetite magnetization map	64
6.4. Ni-XMCD	66
6.5. Low crystal field dichroism	70
6.6. Fe ₃ O ₄ (110)/NiO - Anisotropic XMLD	72
6.7. Fe ₃ O ₄ (110)/NiO interface structure	76
6.8. Thickness dependent XMD	79
6.9. Thickness dependent XMD	80
6.10. NiO wedge on magnetite(110):XMCD sum-rule analysis	81

6.11. Temperature dependent domain contrast	83
6.12. Mean-field behaviour of $\langle \boldsymbol{\mu} \rangle, \langle \boldsymbol{\mu} \rangle^2$ and $\langle \boldsymbol{\mu}^2 \rangle$	85
7.1. Fe_3O_4 (111)/NiO - islands at 1100 K	92
7.2. XAS Spectra of FeO islands	93
7.3. Magnetite: Sample stoichiometry by XMCD analysis	94
7.4. Quasidomains at the Fe_3O_4 surface	95
7.5. Fe_3O_4 (001)/NiO – theory	99
7.6. Fe_3O_4 (001)/NiO – angular dependent XMLD	100
7.7. Fe_3O_4 (111)/NiO coupling	102
7.8. Interface orientation and uncompensated magnetization	103
7.9. Magnetoelastic situation at the (110)-interface	105
7.10. Magnetoelastic deformations in NiO and magnetite in (001) orientation	106
8.1. Different XMLD spectra for magnetite	114
8.2. Schematic view of the fitting process	116
8.3. Antiferromagnetic domain walls in magnetite(110)/NiO	117
8.4. Co domain axes	119
8.5. $\text{Fe}_3\text{O}_4/\text{NiO}/\text{Co}$ sandwich	120
A.1. On the calculation of the shear strain.	131

List of Tables

2.1. Spin and orbital polarization of photoelectrons excited from a 2p core level	15
6.1. Values for the L_2 ratio for various spin directions	75
7.1. Magnetoelastic distortions in Fe_3O_4 (001)/NiO	108
A.1. Elastic and magnetoelastic properties of NiO, NFO and magnetite.	132
A.2. Units conversion and confusion	133

Introduction

Within 5000 years, mankind has taken a giant leap in information technology. Since the development of writing, a search for better and denser recording technologies has continued over the centuries. In short: Papyrus, parchment¹, paper², print³, PDF⁴. The latter has become a symbol for the digital era, where information is decomposed into combinations of only two values – 0 and 1. About 2500 years ago, first signs of another marvelous development emerged: The discovery of magnetism. THALES OF MILETUS observed about 600 B.C. that iron is attracted by "lodestone" (or more commonly known as magnetite)[151, 156]. Around 100 B.C., lodestone was used in China for geomantic purposes, and around 1100, first navigation devices are reported by Chinese astronomers – the compass was born [156].

About 50 years ago, both branches of human progress should mingle in a most fascinating manner. It was the birth of digital magnetic storage technology, which caused a boost of storage density and velocity unprecedented in human history. Since the end of the 19th century, magnetic media were used to record analogous signals, for example for voice recording. In the 20th century, the step towards digital recording was made. In 1940 magnetic core memory was used for nonvolatile storage and fast processing of data in IBM's first computing machines. The use of magnetic tapes for data archiving was first introduced in 1951. Finally, 1952 the first device comparable to the modern harddisk was constructed, the IBM RAMAC, a set of 50 magnetic disks with a total capacity of 5 MByte, corresponding to a data density of about 5 kBit/square-inch. For the first time, random data access was achieved by means of read/write heads hovering the surface of the rotating disc stack on an air cushion[109].

¹In the middle age, papyrus was replaced by the more durable parchment.

²The first paper was manufactured around 100 A.D. in China [113, 117].

³Printing technology by letters was invented in the 15th century by JOHANNES GUTENBERG and subsequently became the main reproduction method for written documents [58]. Earlier attempts to implement this technique have been reported from China and Korea (11th-12th century), but obviously did not prevail [118].

⁴The Portable Document Format, nowadays the most widespread format for electronic documents.

The next milestone was marked by the discovery of *Interlayer Exchange Coupling* by GRÜNBERG *et al.* [56] in 1986, and two years later the *Giant Magnetoresistance* (GMR), which was independently confirmed by the groups of GRÜNBERG (BINASCH *et al.* [13]) and FERT (BAIBICH *et al.* [11]). It should not take long until the first harddisk read head based on this phenomenon would enable a multiplication of the storage density to more than 1 GBit/square-inch. Briefly sketched, the GMR effect manifests, when a current is passed through a stack of two ferromagnetic layers separated by a nonmagnetic conducting spacer, and the *relative* orientation of the magnetization in the two ferromagnets is changed. It was found that antiparallel alignment increases resistance as compared to parallel alignment, typically by a few tens of percent. In a magnetic field sensor, one of the two layers must be a stable reference in terms of magnetization direction, while the other should rotate freely with external field. In order to achieve this, both ferromagnets must be different in some way, which first was achieved by different thicknesses and/or materials. The ferromagnet with the higher coercivity then served as reference for a limited range of external field strengths. However, the need for miniaturization of magnetic read heads soon put limits to this design, since the demagnetizing fields made the reference layer unstable.

To overcome this obstacle, it was not necessary to invent something new, but rather make use of an "old" effect discovered already in 1956 by MEIKLEJOHN and BEAN [97]. For magnetic Cobalt particles superficially oxidized, they found that cooling them down from high-temperature in a magnetic field resulted in a unidirectional anisotropy along the cooling field direction. This means that even after the field was switched off, the particles resisted the attempt to turn the magnetization out of this direction, manifesting in a shifted hysteresis loop. The authors concluded that the effect was caused by interfacial exchange interaction, and called the loop shift "*exchange bias*". Exchange bias was subsequently used to pin the magnetization of the reference layer to a fixed direction, returning to the same orientation even after disturbance by a strong external field. The technological potential motivated a great number of studies aimed at finding a comprehensive microscopic description [107]. The present situation is probably most strikingly and humorously described by a statement of IVAN K. SCHULLER and GERNOT GÜNTHERODT in the "Exchange Bias Manifesto" [133]:

There is a time in the life of scientists when it is important to consider: What is the Grand Purpose of it all? In this case, we started wondering, why all papers in Exchange Bias start by stating something like: "Although exchange bias was discovered more than 40 years ago, the origin of this phenomenon is still not clear."

The reason may be that there is not a single origin, and that highly material-specific mechanisms are often at work. This thesis touches the field of exchange

bias, as it is aimed at investigating the more general phenomenon called the *magnetic proximity effect*, i. e. the alteration of the magnetic structure of two magnetic materials in contact with respect to the uncoupled case. The latter can have various origins, and exchange-interaction at the interface is only one of them. To name a few others: The first and most important is the breaking of translational symmetry near the interface, which introduces additional electronic states not present in the bulk materials, and which can also lead to new higher-order exchange interactions as, for example, the DZVALOSHINSKY-MORIYA interaction [37]. A second mechanism is interfacial hybridization between compatible electronic states in the two materials. Besides the aforementioned effects, which tend to be short-ranged, there are longer-ranged contributions arising from the mechanical coupling of the two layers: The epitaxial lattice strain and magnetostriction lead to a mutual influence of the two materials in contact. It is important to note, that the latter effects up to now have not found their way into the theoretical framework describing exchange-bias. In this thesis, we will present evidence that the magnetoelastic influences cannot be neglected in the description of magnetic interface coupling, and may even be a vital factor in some cases.

The advance in a comprehensive understanding of the magnetic proximity effect is often hampered by the difficulties in manipulating and analyzing the antiferromagnet – due to its vanishing net moment. However, its secrets can be unveiled by using *polarized* neutrons or x-rays. While neutrons possess a magnetic moment, which can be oriented by *spin-filtering* at the cost of flux, in order to become sensitive to the spin-order inside the solid, x-ray photons can be *generated* with high fluxes and a well-defined polarization of their electromagnetic field. While both techniques allow for suitable scattering experiments on bulk-like samples in order to determine magnetic form- and structure factors, x-rays generated in modern synchrotron sources have three big advantages over neutrons: (i) The available photon energies cover a wide range, allowing for spectroscopy and chemical sensitivity; (ii) They exhibit a much higher interaction cross section with matter. (iii) Their degree of polarization is usually higher than the one of neutrons, and polarization can be manipulated more conveniently. This opens the way for a wide range of *magnetic spectroscopies*, addressing different types of magnetic order. While X-ray Magnetic Circular Dichroism (XMCD) is suitable for ferromagnets, since it requires a nonvanishing average over atomic magnetic moments, X-ray Magnetic Linear Dichroism (XMLD) is not bound to this restriction, being sensitive to the square of the magnetic moment per atom. Thus, sufficiently collinear magnetic structures can be investigated, too, among them many types of antiferromagnets.

All the aspects mentioned above allow to focus the investigation down to single magnetic layers, surfaces, interfaces and nanostructures. The latter can be conve-

niently addressed by the growing field of x-ray microscopy and microspectroscopy, allowing to collect spatially resolved information down to nanometer-resolution. This is the reason for the choice of X-ray Photoelectron Emission Microscopy (X-PEEM) as primary investigation technique throughout this thesis. Combining microscopy with magnetic spectroscopies, *vectorial magnetometry* can be performed on a spatial-resolved basis, i.e. the true orientation of the spin-order in real space can be determined for both ferro- and antiferromagnetic domains. Being able to study the latter is a vitally important factor, since by XMLD spectromicroscopy, one can directly look at the antiferromagnetic domain state, which has a major influence on exchange bias. However, particularly the analysis of the antiferromagnetic order by XMLD is still a hard and demanding task, as will be sketched in the following.

Scope

This thesis is organized as follows: In Chap. 1, we thoroughly discuss magnetic spectroscopy using x-rays, since it is the key to unravel the magnetic structure of a solid. Especially, the x-ray magnetic linear dichroism (XMLD) allows to investigate the structure of antiferromagnets, which is only accessible to few techniques due to the vanishing net moment. We put explicit weight on incorporating the recent insights into the effect for crystalline systems, which show that the XMLD is "anisotropic" [82, 32, 8, 9], therefore rendering many studies based on an "isotropic" modelling of the effect questionable (see, for example, the discussion of ARENHOLZ *et al.* on this issue in Ref. [9]). We avoid this pitfall by a thorough analysis of the experimental geometry and the crystalline orientation of the sample. Consequently, we are, for the first time, in the position to perform reliable *vectorial magnetometry* in crystalline antiferromagnets.

Chap. 3 gives some details about the electronic and magnetic properties of the materials used in this thesis, namely NiO and Fe₃O₄. For NiO the concept of *antiferromagnetic domain walls* will be introduced, which in bulk NiO are of magnetoelastic origin. The antiferromagnetic domain walls found in exchange coupled NiO layers, however, are determined by exchange anisotropy rather than magnetoelasticity and thus represent a new type of antiferromagnetic domain wall, which has not been modelled up to now.

In Chap. 4, we will briefly explain, how polarized x-rays are generated, and how Photoelectron Emission Microscopy (PEEM) employing soft x-rays works. Subsequently, we give a brief overview about the magnetic proximity effect in Chap. 5, putting some weight on the question about the occurrence of spin-flop coupling, which is a main subject of our investigation.

We will commence the presentation of our results with the Magnetite/NiO (110)-interface in Chap. 6, where it will be shown that the interfacial proximity zone is ultrasharp and comprises only a few monolayers near the interface. The surprising result is that the interface, which should be compensated, exhibits no spin-flop coupling as predicted by the theory of KOON [75]. This finding is discussed in detail in terms of the magnetocrystalline structure of the interface. Temperature-dependent measurements are presented, which show that the ordering temperatures in both NiO and the interfacial region of magnetite are lowered, possibly due to finite size effects and an altered magnetic structure near the interface.

In Chap. 7 we will compare the magnetic proximity effect for different crystalline interface-orientations. Strong variations in the uncompensated magnetization are found, which will be discussed with respect to the particular bonding situation and magnetic anisotropy expected for the three orientations. The coupling scheme (collinear or spin-flop) is not always consistent with the current theoretical framework and we will give an explanation in terms of magnetoelastic interactions.

After this comparative analysis, we will come back to the (110) interface in Chap. 8 and focus our view on the constrained antiferromagnetic domain walls that form in the exchange-coupled NiO adlayer. The fitting of the domain wall profiles by a simple model yields valuable information not only about the walls themselves, but also about the general magnetic anisotropy in the coupled system. Finally, a system corresponding to a trilayer with an AF spacer is formed by deposition of a Co layer on top of NiO. The Co layer inherits part of the magnetic anisotropy of the $\text{Fe}_3\text{O}_4/\text{NiO}$ system, but shows a strict spin-flop configuration with respect to the magnetite substrate. We will provide two explanations for this behaviour, one in accordance with roughness-driven interlayer coupling, the other basically assuming a completely separable coupling of magnetite and Co to the NiO spacer.

Finally, we will conclude our analysis and stress the main results, whereafter we will dare a glimpse into the future in order to show potential applications and experimental roadmaps in Chap. 9.

Part I.

**Theoretical and Experimental
Background**

1. Magnetic spectroscopy using X-rays

In the following chapter the physics of X-ray Absorption Spectroscopy (XAS) and magneto-optical effects in the x-ray regime will be explained. Since the focus of this thesis lies on *vectorial magnetometry*, i.e. the extraction of the orientation of magnetic moments in space from the spectroscopic data, special weight is put on the symmetry properties of the dielectric tensor and the XAS process. This can be conveniently done in a classical approach, and the link to quantum mechanics is finally made by the KUBO-formula [20, 36], which relates the dielectric tensor to the quantum mechanical transition matrix elements.

1.1. Classical description of absorption and magneto-optical phenomena

The formal description of the x-ray absorption and dichroism roots in the classical theory of electromagnetism in continuous media. Although "classical", they can be combined with the quantum description by first calculating the dielectric tensor from quantum mechanical principles and then applying the classical formalism to describe scattering and absorption as derived by electrodynamics. For simplicity, we will here mostly concentrate on the absorptive processes.

1.1.1. Absorption

The following sections make use of the CGS system, which is a convenient choice for electrodynamics. For conversion of the relevant quantities into the SI system, please refer to Appendix A.2. If energy dissipation occurs, i.e. in an absorptive medium, then the dissipated or absorbed energy is given by the divergence of the POYNTING vector (POYNTING's theorem – see, for example,

[1]):

$$\frac{1}{4\pi} \left(\mathbf{E} \frac{\partial \mathbf{D}}{\partial t} + \mathbf{H} \frac{\partial \mathbf{B}}{\partial t} \right) = -\frac{c}{4\pi} \operatorname{div}(\mathbf{E} \times \mathbf{H}) \quad (1.1)$$

$$\frac{1}{4\pi} \int_V \mathbf{E} \frac{\partial \mathbf{D}}{\partial t} + \mathbf{H} \frac{\partial \mathbf{B}}{\partial t} dV = -\frac{c}{4\pi} \oint (\mathbf{E} \times \mathbf{H})_n d\mathbf{S} \quad (1.2)$$

Assuming no magnetic losses, the absorption intensity of a XAS spectrum can then be calculated from the imaginary part of the dielectric tensor like:

$$\begin{aligned} \mu_{XAS} &= \frac{1}{4\pi V} \int \mathbf{E} \frac{\partial \mathbf{D}}{\partial t} dV \\ &= \frac{i\omega}{16\pi} (\mathbf{E}_0 \mathbf{D}_0^* - \mathbf{E}_0^* \mathbf{D}_0) \\ &= -\frac{\omega}{8\pi} \operatorname{Im} \{ \mathbf{E}_0^* \hat{\epsilon} \mathbf{E}_0 \} . \end{aligned} \quad (1.3)$$

In the last steps we have substituted the plane wave solutions for \mathbf{E} and \mathbf{D} ¹ with the complex amplitudes \mathbf{E}_0 and \mathbf{D}_0 , carried out the high-frequency averaging $\overline{\dots}$, which corresponds to dropping all terms containing $e^{\pm 2i\omega}$, and finally used the MAXWELL dielectric displacement field in a medium, which is commonly written as

$$\mathbf{D} = \hat{\epsilon} \mathbf{E} \quad (1.4)$$

where $\hat{\epsilon}(\omega, \mathbf{k})$ is the complex dielectric tensor.

1.1.2. Dielectric tensor and optical effects

The dielectric tensor can be generally written as an expansion including higher order optical effects (see, for example, [116]). The expansion is made in terms of \mathbf{E} and \mathbf{H} , but we will here use \mathbf{M} , the magnetization, instead of \mathbf{H} , the internal magnetic field, i. e. the magnetic induction $\mathbf{B} = \mathbf{H} + 4\pi\mathbf{M}$ is set to zero. Note that in contrast to the optical regime, for x-ray absorption, the quantity \mathbf{M} does *not* represent the magnetization, but the atomic magnetic moment, which is why for x-ray absorption, the expansion is only valid on the atomic scale. To lowest orders, the series expansion then looks as follows:

$$\epsilon_{ik} = \underbrace{\kappa_{ik}^{(s)}}_{\text{isotr.} + \text{NLB} + \text{NLD}} + \underbrace{\alpha_{ikl}^{(a)} k_l}_{\text{NCB} + \text{NCD}} + \underbrace{\beta_{ikl}^{(a)} M_l}_{\text{MCB} + \text{MCD}} + \underbrace{\gamma_{iklm}^{(s)} M_l M_m}_{\text{MLB} + \text{MLD}} \dots \quad (1.5)$$

¹ $\mathbf{E} = \frac{1}{2}(\mathbf{E}_0 e^{i(\mathbf{k}\cdot\mathbf{r}-\omega t)} + \mathbf{E}_0^* e^{-i(\mathbf{k}\cdot\mathbf{r}-\omega t)})$, \mathbf{D} analogous.

²Here we have omitted higher-order terms in \mathbf{k} and \mathbf{M} , which are responsible for additional contributions to dichroism and birefringence. For example, terms with odd products of the

In the following, we will explain the meaning of the tensors of this expansion:

- $\kappa_{ik}^{(s)}$ is a complex symmetric tensor and contains the isotropic part and additional anisotropic effects like natural linear birefringence (NLB) and natural linear dichroism (NLD) in its real and imaginary part, respectively.
- $\alpha_{ikl}^{(a)}$ is a totally antisymmetric third rank tensor which contains *gyrotropic* effects caused by spatial dispersion, i.e. the inhomogeneity $\frac{\partial \mathbf{E}}{\partial x_l} = k_l \mathbf{E}$ of the electromagnetic field on a length scale a/λ , i.e. if the wavelength λ is in the order of the lattice constant a . Spatial dispersion is responsible for Natural Circular Birefringence (NCB) and Dichroism (NCD). Note that this term goes beyond the dipole approximation, since the condition $\lambda \gg a$ is not fulfilled. We will see later on that spatial dispersion is responsible for X-ray Natural Circular Dichroism, which originates from mixtures of E1 (dipole) and E2 (quadrupole) transitions. In terms of symmetry, the effects of natural circular dichroism can be formally described in a very similar manner as the effects of magnetic circular dichroism, which is why we explicitly included them into our discussion, although all magneto-optic effects important for this thesis are well described within the dipole approximation.
- $\beta_{ikl}^{(a)}$, totally antisymmetric, is a magneto-optic contribution caused by *gyrotropic* effects $\beta_{ikl}^{(a)} M_l$, which are *linear* in the magnetic field $\mathbf{H} = \mathbf{B} - 4\pi \mathbf{M}$, or simply the magnetization \mathbf{M} when no external field is applied.
- $\gamma_{iklm}^{(s)}$ is a symmetric fourth rank tensor, which describes effects that are *quadratic* in \mathbf{M} and therefore responsible for the quadratic magneto-optic effects like Magnetic Linear Birefringence (MLB) and Dichroism (MLD)³.

We will now carry out the contraction of the tensors in Eq. 1.5, in order to derive a compact form of the dielectric tensor comprising all magneto-optic effects. The magneto-optic tensor β_{ikl} can be contracted by the definition of a so-called complex *gyration pseudotensor* g_{ml} and the definition of the magnetization vector $\mathbf{M} = MM' = M[x, y, z]$:

$$M\beta_{ikl} = M\mathcal{E}_{ikm}g_{ml} \quad (1.6)$$

magnetization vector components will contribute to the MCB/MCD, whereas even products will contribute to the MCB/MLD. Mixtures of \mathbf{k} and \mathbf{M} describe so-called magneto-spatial dispersion effects, as for example magneto-chiral dichroism (M χ D).

³Note that for XMLD, the macroscopic value of the magnetization cannot be used. Since XAS is a *local* probe, the XMLD is proportional to the square of the *local* magnetic moment in the excited atom. For a collinear ferromagnet, averaging over all atoms in a test volume, one yields $1/V \sum_{i=1}^N \boldsymbol{\mu}^2 = N/V \boldsymbol{\mu}^2 \neq \mathbf{M}^2 = (1/V \sum_{i=1}^N \boldsymbol{\mu})^2$. For collinear ferri- or antiferromagnetic systems, analogous inequalities can be derived.

and a complex gyration pseudovector by

$$g_i = g_{ik}M'_k \quad . \quad (1.7)$$

It is interesting to see the analogy between gyration by spatial dispersion (NCD) and magnetic effects (MCD), so we show here for comparison the contribution in terms of \mathbf{k} : For a plane wave with $\mathbf{k} = \mathbf{k}'\omega/c$, one can define a similar gyration pseudotensor, which is defined as

$$\frac{\omega}{c}\alpha_{ikl} = \frac{\omega}{c}\mathcal{E}_{ikm}f_{ml} \quad (1.8)$$

and a complex gyration pseudovector by

$$f_i = f_{ik}k'_k \quad . \quad (1.9)$$

For practical purposes (with respect to the materials NiO and Fe₃O₄ used in this thesis) we write down g_{ik} in cubic symmetry, which is diagonal with only one element g . We then yield the important relation,

$$\mathbf{g} = g[x, y, z] \quad , \quad (1.10)$$

i.e. the gyration vector is always parallel to the magnetization unit vector. This has important consequences for the angular dependence of circular dichroism, which in cubic symmetry can be described by a simple relationship (). If the symmetry is lower than cubic, \mathbf{g} and \mathbf{M} are not necessarily parallel any more, and the angular dependence gets more complicated. Finally, we contract the tensor $\gamma_{ik(l)(m)}M_{(l)}M_{(m)}$, and for cubic symmetry it takes the form (in VOIGT notation):

$$\begin{aligned} M^2\hat{\gamma}(\mathbf{M}') &= M^2 \begin{bmatrix} \gamma_{11} & \gamma_{12} & \gamma_{12} & 0 & 0 & 0 \\ \gamma_{12} & \gamma_{11} & \gamma_{12} & 0 & 0 & 0 \\ \gamma_{12} & \gamma_{12} & \gamma_{11} & 0 & 0 & 0 \\ 0 & 0 & 0 & \gamma_{44} & 0 & 0 \\ 0 & 0 & 0 & 0 & \gamma_{44} & 0 \\ 0 & 0 & 0 & 0 & 0 & \gamma_{44} \end{bmatrix} \begin{bmatrix} x^2 \\ y^2 \\ z^2 \\ yz \\ xz \\ xy \end{bmatrix} \\ &= M^2 \begin{bmatrix} \gamma_{12} + (\gamma_{11} - \gamma_{12})x^2 & \gamma_{44}xy & \gamma_{44}xz \\ \gamma_{44}xy & \gamma_{12} + (\gamma_{11} - \gamma_{12})y^2 & \gamma_{44}yz \\ \gamma_{44}xz & \gamma_{44}xz & \gamma_{12} + (\gamma_{11} - \gamma_{12})z^2 \end{bmatrix} \end{aligned} \quad (1.11)$$

Equation 1.11 is very important, since it contains the angular dependence of the MLD upon rotation of the magnetization \mathbf{M} , which must be known, if one wants to perform vectorial magnetometry using MLD, i.e. if one wants to conclude back

on the orientation of the spin-axis \mathbf{M} from measurements of the dielectric tensor components. Furthermore it is important to know that if $\gamma_{44} = (\gamma_{11} - \gamma_{12})$, the MLD is "isotropic"⁴, i.e. does not depend on the orientation of \mathbf{M} with respect to the cubic principal axes. We will come back to this important aspect later. Fully contracted, equation 1.5 then takes the form

$$\mathbf{D} = \hat{\boldsymbol{\kappa}}\mathbf{E} - i\frac{\omega}{c}\mathbf{f} \times \mathbf{E} - iM\mathbf{g} \times \mathbf{E} + M^2\hat{\boldsymbol{\gamma}}\mathbf{E} \quad (1.12)$$

$$= \hat{\boldsymbol{\epsilon}}\mathbf{E} \quad , \quad (1.13)$$

and we can now write down the dielectric tensor for cubic crystal symmetry and optical activity due to magnetism as follows:

$$\hat{\boldsymbol{\epsilon}}(\mathbf{M}') = \begin{bmatrix} \kappa + M^2\{\gamma_{12} + (\gamma_{11} - \gamma_{12})x^2\} & M^2\gamma_{44}xy + iMgz & M^2\gamma_{44}xz - iMgy \\ M^2\gamma_{44}xy - iMgz & \kappa + M^2\{\gamma_{12} + (\gamma_{11} - \gamma_{12})y^2\} & M^2\gamma_{44}yz + iMgx \\ M^2\gamma_{44}xz + iMgy & M^2\gamma_{44}yz - iMgx & \kappa + M^2\{\gamma_{12} + (\gamma_{11} - \gamma_{12})z^2\} \end{bmatrix} . \quad (1.14)$$

The antisymmetric non-diagonal elements are responsible for the MCD, which is only observed using circularly polarized radiation. With the polarization \mathbf{e} defined as $\mathbf{E}(\mathbf{k}, t) = E_0\mathbf{e}e^{i(\mathbf{k}\cdot\mathbf{r} - \omega t)}$, $\mathbf{e}^+ = -\frac{1}{\sqrt{2}}(\mathbf{x} + i\mathbf{y})$ means right circular and $\mathbf{e}^- = \frac{1}{\sqrt{2}}(\mathbf{x} - i\mathbf{y})$ means left circular polarization for photons incident along positive \mathbf{z} direction⁵. Using Eq. 1.3, one finds that the complex gyration vector g will cause a contribution to the absorption, but differently for left and right circularly polarized light. The difference in absorption, the MCD signal, is then

$$\mu_{\text{MCD}} = \mu^+ - \mu^- = -\text{Im}(-2Mgz) \quad . \quad (1.15)$$

Apparently, in cubic symmetry, the angular dependence of the MCD can be described by the simple relationship

$$\mu_{\text{MCD}} = 2Mg\mathbf{k}' \cdot \mathbf{M}' \quad , \quad (1.16)$$

which means that the size of the MCD signal depends on the *cosine between the wave-vector and the magnetization*. Remind, that this simple relationship is only strictly valid for cubic or higher symmetry. In the x-ray regime, deviations in other symmetries are related to the magnetic dipole operator (see Sec. 2.1.3).

⁴We write the terms "isotropic" and "anisotropic" XMLD, which are used now throughout in literature in quotation marks, for the following reason: By definition, any dichroism is an anisotropic property, so the XMLD can, in principle, not be called isotropic. However, the term isotropic is used in literature whenever it is meant that it does not depend on the crystalline symmetry of the sample, i. e. the XMLD yields the same value for arbitrary choice of the quantization axis \mathbf{S} , and otherwise orienting \mathbf{E} in the same way. The "isotropic" XMLD then depends only on $(\mathbf{E} \cdot \mathbf{S})^2$.

⁵the \mathbf{e}^\pm are eigenfunctions of the angular momentum operator $L_z\mathbf{e}^\pm = \pm\hbar\mathbf{e}^\pm$.

Whereas the antisymmetric non-diagonal elements are responsible for the MCD, the imaginary symmetric elements are the origin of the linear dichroism, since for linear polarization, which is a real quantity, all the antisymmetric non-diagonal elements will cancel.

1.1.3. Link between electrodynamics and quantum mechanics - the Kubo-formula

If we redefine the dielectric tensor $\hat{\epsilon}$ using the complex optical conductivity tensor $\hat{\sigma}$ we obtain

$$\hat{\epsilon}(\omega) = \widehat{\delta}_{kl} + \imath \frac{4\pi}{\omega} \hat{\sigma}(\omega) \quad (\text{CGS}) \quad (1.17)$$

According to linear response theory, $\hat{\sigma}$ is the response function of the current density within the solid to a driving external electric field (see for example [36]). The KUBO-formula then relates the elements of the conductivity tensor to the FOURIER transformation of current densities within the solid [20]:

$$\sigma_{kl} = \imath \frac{Ne^2}{m\omega} \delta_{kl} + \frac{1}{\omega} \int_0^\infty \langle [j_k(t), j_l(0)] \rangle e^{\imath\omega t} dt \quad (1.18)$$

This many-particle relation can be transformed into a single-particle form using a HARTREE-FOCK approximation, where the wavefunctions are composed of SLATER-determinants of single-particle wavefunctions. Expressing the current operator in terms of the single-particle momentum operator, one arrives at the form [112]

$$\sigma_{kl}(\omega) = -\imath \frac{e^2}{m^2 V \hbar} \sum_{nn'} \frac{f(E_n) - f(E_{n'})}{\omega_{nn'}} \frac{\Pi_{n'n}^k \Pi_{nn'}^l}{\omega + \imath/\tau - \omega_{nn'}} \quad (1.19)$$

where $\Pi_{nn'}^k = \langle n | p_k | n' \rangle$ are the matrix elements of the k-component of the momentum operator and $|n\rangle$ are single-particle states with energies E_n , which are occupied according to the FERMI-DIRAC distribution $f(E_n)$. Furthermore, $\hbar\omega_{nn'} = E_n - E_{n'}$ is the excitation energy, and τ was added as a relaxation time to assure convergence. If discrete states are involved, Eq. 1.19 can be rewritten as a sum over initial and final states:

$$\sigma_{kl}(\omega) = -\frac{\imath e^2}{m^2 V \hbar} \sum_i^{\text{occ.}} \sum_f^{\text{unocc.}} \frac{1}{\omega_{fi}} \left(\frac{\Pi_{if}^k \Pi_{fi}^l}{\omega + \imath/\tau - \omega_{fi}} \right), \quad (1.20)$$

which in the limit of $\tau \rightarrow \infty$ together with the LORENTZian representation of the DIRAC δ -distribution yields a more general version of FERMI's Golden Rule

$$\sigma_{kl}(\omega) = -\frac{ie^2\pi}{m^2V\hbar\omega} \sum_i^{\text{occ.}} \sum_f^{\text{unocc.}} \Pi_{if}^k \Pi_{fi}^l \delta(\omega - \omega_{fi}) \quad , \quad (1.21)$$

If we now describe the optical processes in dipole approximation, the Π 's become the familiar dipole transition matrix elements $\Pi_{fi}^k = im\omega \langle f | \mathbf{e}_k \cdot \mathbf{r} | i \rangle$, which enter in this way into the dielectric tensor.

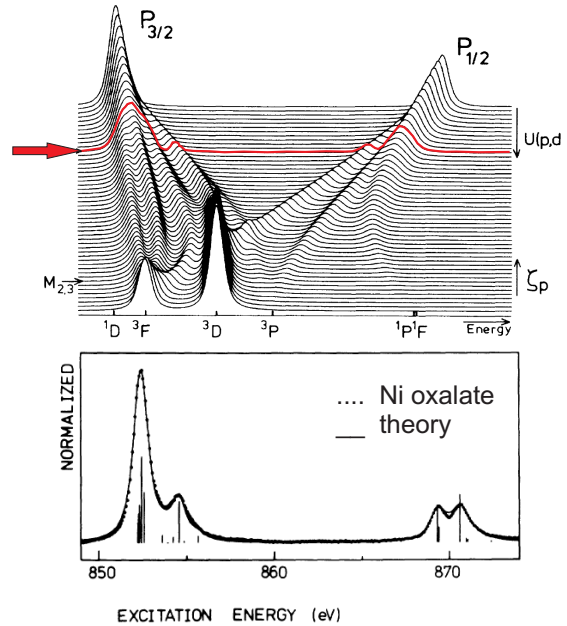
1.2. X-ray absorption spectroscopy (XAS) and its application to magnetism

When an x-ray photon is absorbed by an atom, its energy and momentum is transferred to the inner shell electron distribution around this atom in the first place. This is the most important thing to realize – the x-ray absorption process is a *local* probe. By choosing the right excitation energies, element-specific quantities can be determined, such as the number of electrons/holes in specific shells, or in case of magnetic atoms the atomic spin- and orbital momenta. Moreover, if the atoms are embedded into a solid, solid state properties influencing the local atomic environment can be analyzed, such as crystal fields, orbital symmetry and magneto-crystalline anisotropy. In the following, the relevant mechanisms that both help and hamper the analysis of the solid will be discussed, with special weight on the magnetic spectroscopies.

1.2.1. The x-ray absorption process

Simply spoken the x-ray absorption process can be described by the promotion of a single electron from its ground state, let's say a localized core level, into an excited state of higher energy (see Fig. 1.1). The drawback of this picture is that it neglects the influence of the remaining electrons, simply assuming that they don't participate in the process. This single particle picture is thus not always an appropriate approximation, albeit it may serve as a "rule of thumb" due to its simplicity. In general, it is better to argue in a "configuration picture", where the whole atomic arrangement of electrons/holes before and after the excitation process is taken into account. For example in a Nickel atom (which is also a subject of this thesis), an absorption process from the $2p$ core levels into the $3d$ states will be labelled $2p^6 3d^8 \rightarrow 2p^5 3d^9$. In this case, the transition can be conveniently described by holes instead of electrons ($2\underline{p}^0 3\underline{d}^2 \rightarrow 2\underline{p}^1 3\underline{d}^1$). One can imagine that

Figure 1.1: Atomic multiplet calculations for Nickel. The top spectrum corresponds to a case without exchange and correlation effects ($U(p, d) = 0$). The bottom case is the other extreme where the spin-orbit interaction of the core hole is zero. While metals resemble the topmost spectra due to their efficient screening, insulators like NiO are located in the intermediate region, as shown by the small arrow in a). b) Experimental spectrum of Ni-oxalate, where Ni^{2+} is high-spin in an O_h -crystal field. (picture taken from [162]).



both holes in the final state will influence each other – by Coulomb and exchange interactions. Furthermore, the core hole will have an angular momentum and thus exhibit a spin-orbit splitting, in contrast to the closed $2p$ shell in the initial state. Looking at the XAS spectra, one will thus find a so-called multiplet structure due to exchange and correlation effects in addition to the spin-orbit splitting. The interplay of spin-orbit and multiplet splitting is modelled in Fig. 1.1, where the top spectrum corresponds to the case where exchange-correlation is turned off and the bottom spectrum is valid for zero spin-orbit coupling of the core hole. Due to the better screening of the Coulomb interaction in metals, their spectra will look more like the top spectrum, while, for example, the insulator NiO represents an intermediate case shown by the small horizontal arrow. Multiplet effects play an important role in magnetic XAS, since they can *enhance* magnetic effects like linear or circular dichroism.

Another important aspect is the polarization (or: angular momentum) of the photon. During the absorption process, it is transferred to the initial electronic configuration, leaving behind a (spin-, orbitally) *polarized core hole* and producing (spin-, orbitally) *polarized photoelectrons*. Selection rules (dipole radiation), symmetry and spin orientation of the final states then decide over which of the final states can be reached by those electrons. Thus the clever choice of the light polarization is the essence of magnetic x-ray spectroscopy.

2. Dichroism

Dichroism is a term derived from Greek and basically means "two colours". In the optical regime it describes the effect of a solid changing its color when irradiated with light of different incidence angle or polarization. It is a consequence of optical anisotropy in the material, i.e. of an optical symmetry lower than cubic. Depending on the light polarization one distinguishes *linear* or *circular dichroism*. Besides the optical regime, both effects also occur under excitation with x-rays. Depending on the symmetry breaking element, one distinguishes x-ray nonmagnetic (natural, XNCD) and magnetic circular dichroism (XMCD).

2.1. Circular Dichroism

2.1.1. X-ray natural circular dichroism (XNCD)

In the x-ray regime, XNCD is observed in optical biaxial crystals without a center of inversion. The main source are interference terms between electrical dipole (E1) and quadrupole (E2) transitions [55, 23] in the presence of an anisotropic charge density of lower than cubic symmetry. The effect is parity odd and time even. In contrast to the mechanisms described in the following, XNCD is an effect beyond the dipole approximation and thus generally much less pronounced than the first order effects.

2.1.2. X-ray magnetic circular dichroism (XMCD)

XMCD is caused by directional symmetry breaking of magnetic origin, for example in a material with spontaneous spin-alignment like a ferromagnet or a paramagnetic substance in high magnetic fields. It is parity even and time odd, i.e. the effect reverses also when the magnetization is inverted, which is of great practical use. Theoretically, it has first been predicted in 1975 by ERSKINE and STERN for the $M_{2,3}$ edges of Nickel [39]. Experimentally, XMCD was first found in 1983 by SCHÜTZ *et al.* at the iron K edge (see [135] and references therein).

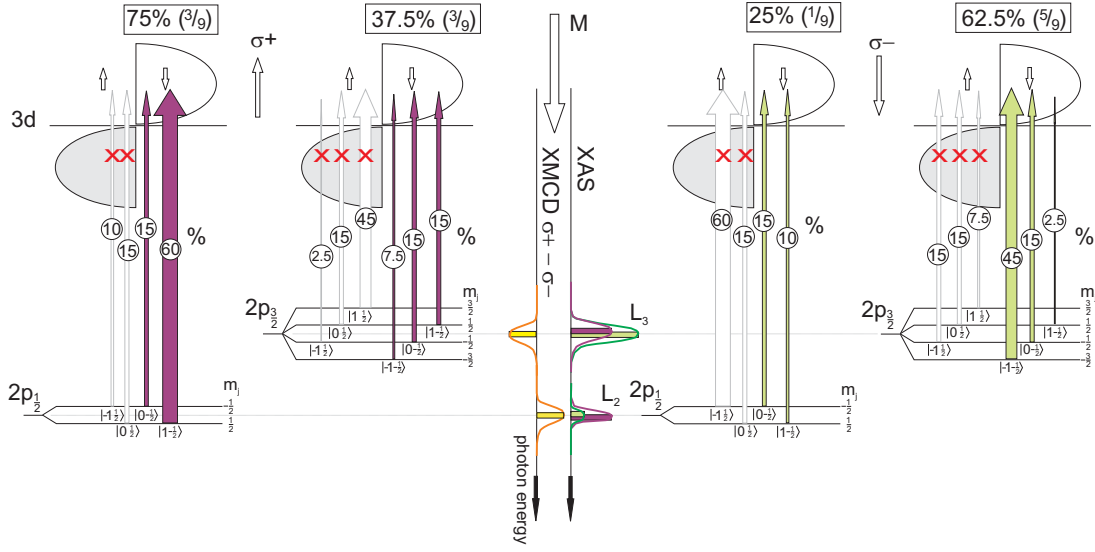


Figure 2.1.: XMCD transition intensities in a single electron picture with large exchange-splitting in the d-bands (majority-band full, minority-band empty). This special electronic configuration produces only a spin-moment, but the atomic orbital moment vanishes because the d-shell is exactly half filled. The left and right side of the diagram show transitions excited by photons with positive (σ^+) and negative (σ^-) helicity, respectively. For each of the spin-orbit split core-levels, the XAS initial states are drawn with a hypothetical core-valence exchange-splitting. They are labelled in $|m_c m_s\rangle$ basis, mainly for pedagogic reasons, since the correct basis-set consists of spin-orbit wavefunctions $|j m_j\rangle$. Allowed transitions into existing final states are symbolized by colored arrows, transitions forbidden due to missing final states by white arrows bearing a red "x". For every transition, the relative XAS intensity calculated by Eq. 2.8 is given in % of the total cross section, i.e. the sum over transitions into the *complete* set of final states (empty d-shell). For simplicity the exchange-splitting of the core-hole has been neglected when calculating the XAS spectra and the XMCD signal (shown in the center plot on the vertical energy axis).

In a simple one electron model¹, the effect can be thought of as a two step process, where circularly polarized x-rays excite spin-polarized photoelectrons from a core level, which in turn are transferred to an exchange split higher shell, acting as a spin-detector for those electrons. In the following, we will look at this process in detail.

The first issue is to briefly sketch how a net spin-polarization is created when exciting photoelectrons out of let's say a 2p core level: The photon transfers its angular momentum to the photoelectron. Without consideration of further

¹For its limitations, see Sec. 1.2.1.

effects, the electron spin could have an arbitrary orientation with respect to the orbital momentum. It is only by spin-orbit interaction that the spin orientation is related to this angular momentum.

To quantify the effects of spin-polarization, we will calculate the relative transition intensities $2p_{1/2,3/2} \rightarrow 3d$ in an atomic single-particle model and have to invoke the selection rules for dipole radiation $\Delta l = \pm 1$, $\Delta m_l = 0, \pm 1$, $\Delta m_s = 0$ as well as the Fermi's golden rule for x-ray absorption:

$$\mu_{\text{abs}} = \mathcal{A} M_{fi}^2 \delta(\omega_f - \omega_i - \omega), \quad \mathcal{A} = 4\pi^2 \alpha \omega \quad (2.1)$$

where M_{fi} is the dipole transition matrix element $\langle f | \mathbf{e} \cdot \mathbf{r} | i \rangle$, \mathcal{A} is a normalization factor containing α , the fine structure constant. Based on the atomic wavefunctions, one can carry out a separation into a radial and angular part

$$M_{fi} = \delta(m'_s, m_s) \langle n' l | r | n c \rangle \langle l m_l | \mathbf{e} | c m_c \rangle, \quad (2.2)$$

where c , m_c are the angular momentum quantum numbers of the core level and l , m_l the ones for the final state. One finds that the radial part does not depend on the polarization effects, which change m_l , and the important physics inherent in the dichroic effects is contained in the angular part. Using the spherical tensor notation for the angular part of the dipole operator, one ends up with the evaluation of matrix elements consisting of spherical harmonics only. These can be conveniently solved using the GAUNT-formula [33]

$$\langle Y_{lm_l} | Y_{\lambda q} | Y_{cm_c} \rangle = (-1)^{m_l} \sqrt{\frac{(2l+1)(2\lambda+1)(2c+1)}{4\pi}} \begin{pmatrix} l & \lambda & c \\ m_l & q & m_c \end{pmatrix} \begin{pmatrix} l & \lambda & c \\ 0 & 0 & 0 \end{pmatrix}, \quad (2.3)$$

where the last two terms are WIGNER $3j$ symbols. With $l = c + 1$ for a $2p \rightarrow 3d$ transition, $\lambda = 1$ and $q = +1$, (-1) and $m_l = m_c + 1$, $(m_c - 1)$ for circular right (left) polarization we end up evaluating

$$\begin{aligned} \langle c+1 m_c+1 | C_{+1}^{(1)} | c m_c \rangle &= \sqrt{\frac{(c+m_c+2)(c+m_c+1)}{2(2c+3)(2c+1)}} \\ \langle c+1 m_c-1 | C_{-1}^{(1)} | c m_c \rangle &= \sqrt{\frac{(c-m_c+2)(c-m_c+1)}{2(2c+3)(2c+1)}} \end{aligned}, \quad (2.4)$$

where $C_{+1}^{(1)}$ and $C_{-1}^{(1)}$ are RACAH's spherical tensor operators for circularly polarized light[28].

But we are not finished yet, since the final state of the transition will be spin-orbit split. Thus we have to describe the spin-orbit split $|j m_j\rangle$ states with total angular momentum j by the uncoupled basis states $|c m_c s m_s\rangle$ using the CLEBSCH-GORDAN coefficients:

$$|j m_j\rangle = \sum_{m_c, m_s = m_j - m_c} C_{j m_j | c m_c s m_s} |c m_c s m_s\rangle \quad . \quad (2.5)$$

Those can be derived recursively by application of the angular momentum ladder operators, or can alternatively be described in terms of WIGNER $3j$ symbols like

$$C_{j; m_j | c; m_c; s; m_s} = (-1)^{-(c-s-m_j)} \sqrt{2j+1} \begin{pmatrix} c & s & j \\ m_c & m_s & m_j \end{pmatrix} \quad . \quad (2.6)$$

With the special values $c = 1, s = 1/2, j = c \pm 1/2$ these can be simplified as [136]:

$m_s \rightarrow$	$\frac{1}{2}$	$-\frac{1}{2}$.	(2.7)
$j \downarrow$				
$c + \frac{1}{2}$	$\sqrt{\frac{c+m+1/2}{2c+1}}$	$\sqrt{\frac{c-m+1/2}{2c+1}}$		
$c - \frac{1}{2}$	$-\sqrt{\frac{c-m+1/2}{2c+1}}$	$\sqrt{\frac{c+m+1/2}{2c+1}}$		

Every transition matrix element from a $|c m_c\rangle$ state must thus be weighted by its CLEBSCH-GORDAN coefficient and then be squared to get the relative intensity contribution:

$$I_{c m_c q} \propto |C_{j m_j | c m_c s m_s} \langle Y_{c+1 m_c+q} | Y_{1 q} | Y_{c m_c} \rangle|^2 \quad (2.8)$$

The relative intensities are summarized in Fig. 2.1. There we have assumed a scenario of a strong ferromagnet with completely filled majority band. Since transitions are only allowed to the minority band in this case, the relative transition intensities are the same as in the atomic model, and have to be multiplied by the integrated unoccupied DOS in the spin-down band, which is equivalent to the number of holes per atom n_h . For RCP light, we then get for the L_2 edge ($2p_{1/2}$) $I_{L_2} = 3/9$ and also for the L_3 edge $I_{L_3} = 3/9^2$. Using LCP light or reversing the magnetization yields $I_{L_2} = 1/9$ and $I_{L_3} = 5/9$. If we now calculate the difference intensity $I_{\text{MCD}} = I^{(-)} - I^{(+)}$ at both edges, we see that $I_{\text{MCD}}(L_2) = 2/9$, while $I_{\text{MCD}}(L_3) = -2/9$.

²Values are in units $\mathcal{A}R^2 n_h$, where $\mathcal{A} = 4\pi^2 \alpha \omega$

2.1.3. XMCD sum rules – charge, orbital- and spin-moment

In the last paragraph we have seen that we can probe the unoccupied density of states in the exchange-split d-bands in a ferromagnet by polarized photoelectrons via a XAS-process. This mechanism can be used to conclude back on properties of the occupied density of states in the d-bands, for example to extract the spin- and orbital moment per atom. Therefore, we have to calculate integrals over spin-orbit split edges, which are defined as follows:

$$A = \int_{L_3} (\mu^+ - \mu^-) dE \quad (2.9)$$

$$B = \int_{L_2} (\mu^+ - \mu^-) dE \quad (2.10)$$

$$(2.11)$$

For convenience, the spin- and orbital polarizations of the photoelectrons created by σ^+ -light in the $2p_{1/2}$ and $2p_{3/2}$ manifolds are summarized again in Table 2.1 (they can also be extracted from Fig. 2.1. There we directly see that the spin-

	$2p_{3/2}$	$2p_{1/2}$
multiplicity	4	2
spin pol.	1/4	-1/2
orbital pol.	3/4	3/4

Table 2.1.: Spin and orbital polarization parameters $(I \uparrow - I \downarrow)/(I \uparrow + I \downarrow)$ of photoelectrons created by σ^+ -light.

polarization inverts sign for both edges, and is twice as large for L_2 ($-1/2$) than for L_3 . The orbital polarization is the same, however, for both edges. Since the intensity (multiplicity) is twice as large for L_3 than for L_2 , the spin-part of the XMCD spectrum shows a dip for L_3 and a peak for L_2 , which are of equal intensity. The orbital part, however, shows two peaks of the same sign, the L_3 peak being twice as high as the L_2 peak. To cancel out the orbital part of the spectrum, we thus have to subtract twice the L_2 edge integral ($2B$) from the L_3 edge integral (A), which leads us to the spin-momentum sum rule. Consequently, to cancel the spin-part, we only have to integrate over both edges ($A + B$), which yields then only the orbital momentum. The sum rules can therefore be summarized as

follows:

$$-\langle A - 2B \rangle = \frac{K}{\mu_B} \cdot m_{\text{spin}} \quad (2.12)$$

$$-\langle A + B \rangle = \frac{3K}{2\mu_B} \cdot m_{\text{orb}} \quad . \quad (2.13)$$

To remove the unknown constant K and to compute the magnetic moment per hole, we have to divide by the integral over the isotropic intensity, which is defined as:

$$\begin{aligned} \langle C \rangle &= \langle \mu_{\text{iso}}^{(L_3)} + \mu_{\text{iso}}^{(L_2)} \rangle \\ &= \frac{1}{3} \int_{L_3+L_2} (\mu^{(0)} + \mu^+ + \mu^-) dE \\ &= \frac{1}{2} \int_{L_3+L_2} (\mu^+ + \mu^-) dE \\ &= K n_h \quad , \end{aligned} \quad (2.14)$$

where (0), +, - defines z-linear, right and left circular polarization, respectively. Thus, we arrive at the sum rules for the $2p \rightarrow 3d$ transition:

$$m_{\text{orb}} = -\frac{4}{3} \frac{\langle A + B \rangle}{\langle C \rangle} \cdot n_h \quad (2.15)$$

$$m_{\text{spin}} = -2 \frac{\langle A - 2B \rangle}{\langle C \rangle} \cdot \left(1 + \frac{7}{2} \frac{\langle T_z \rangle}{\langle S_z \rangle} \right) \cdot n_h \quad . \quad (2.16)$$

$\langle T_z \rangle$ is the expectation value of the z-component of the magnetic dipole operator $\mathbf{T} = \mathbf{S} - 3\mathbf{r}'(\mathbf{r}' \cdot \mathbf{S})$, which reflects a quadrupole term in the anisotropic spin density of the $3d$ final states [150]. This term is zero in absence of a charge quadrupole moment, which is the case for systems with cubic or higher symmetry. For lower symmetry, for example at surfaces or epitaxially strained films, \mathbf{T} can contribute to the magnetic dichroism. The equations Eq. 2.15 have been derived in more general form by THOLE *et al.* [153] for the orbital moment in 1992 and CARRA *et al.* [24] for the spin moment one year later. Experimentally, the sum rules have been first confirmed by CHEN *et al.* for the transition metals iron and cobalt [26].

Limitations of the sum rules

In the atomic multiplet approach, a number of approximations have been made that can affect the accuracy of the atomic magnetic moments predicted by sum rule analysis, which have been summarized, for example, in [36, 104]. These will

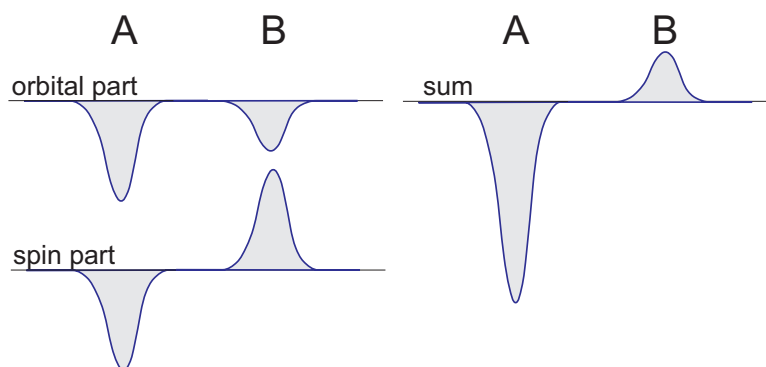


Figure 2.2.: A general XMCD spectrum contains two contributions, one caused by the orbital polarization of the electrons which probe the orbital polarization of the final states, and one from the spin-polarization, which probe the exchange-split spin-density. At each edge, the polarization of the d-states is weighted by the respective spin-polarization of the photoelectrons times the multiplicity of the edge (see Table 2.1). To separate spin- and orbital contribution, one has to integrate both edges separately ($2p_{2/3} \rightarrow A$ and $2p_{1/2} \rightarrow B$) and calculate the sum (A+B) to get the orbital part. Analogously one gets the spin-part by calculating the weighted difference (A-2B).

be discussed in the following. First, dipole transitions $c \rightarrow l = c - 1$ have been neglected. For $3d$ transition metal compounds, this would be $2p \rightarrow 4s$ transitions, for example. A second issue is that intra atomic hybridization is not taken into account. Experimentally, those "parasitary" transitions must be accounted for by subtracting a suitable background from the spectra. This procedure is to some extent arbitrary, since, for example, a branching ratio for the spin-orbit split edges must simply be assumed. In absence of further information, often the standard branching $I(L_3)/I(L_2) = 2 : 1$ is assumed. Due to intra- and interatomic hybridization effects, this is not necessarily correct. A further obstacle is posed by the post-edge background of the edge-jump, which is sometimes difficult to determine due to NEXAFS and EXAFS multiple-scattering resonances in the signal.

A second simplifying assumption by theory is that any energy dependence of the wave functions has been neglected. First, the radial part of the wave functions is assumed energy-independent, which is not exactly true, and second, the prefactor \mathcal{A} is in the transition matrix elements is energy dependent (see Eq. (2.1)). In total, this approximation introduces an error up to 2% for the $3d$ transition metals. A third important limitation is posed by the partial overlap of the spin-orbit split edges, which have been assumed completely separated in the models. The overlap introduces errors mainly in the spin-moment, since its contribution to the XMCD signal has opposite signs at both edges. However, not only overlap,

but also mixing of the two spin-orbit split edges by core-valence exchange and correlation effects affect the accuracy [138], since the branching ratio between $I(L_3)/I(L_2)$ deviates from the ideal atomic value of 2:1. The deviation reduces, however, towards the late transition metals, and is only $\approx 10\%$ for Fe, Co and Ni. Furthermore, the number of holes/electrons in the $3d$ states is unknown *a priori* and must be gained from theoretical calculations, for example by Density Functional Theory. Last but not least we mention the magnetic dipole operator \mathbf{T} , which is zero in all compounds of cubic symmetry *with* inversion center. However, especially at surfaces, symmetry is broken. STÖHR and KÖNIG showed that for a crystal symmetry higher than D_{2h} and small spin-orbit interaction in the $3d$ states, the influence of \mathbf{T} can be eliminated by averaging over measurements with the wavevector \mathbf{k} oriented along three orthogonal directions [150]. A second possibility useful for surfaces is to orient both \mathbf{S} and \mathbf{k} along the "magic" angle of 54.73° with the surface normal, which is a direct consequence of the trace-free quadrupole operator [110]. In this geometry, $\mathbf{T} \perp \mathbf{S}$, thus the size of the spin-moment derived from sum rule analysis is not affected. It currently is common consensus in the scientific community that – because of the limitations stated above – even the most careful evaluation cannot yield orbital moment values with a relative error smaller than $\approx 10\%$.

2.2. Linear Dichroism

2.2.1. Introduction and Terminology

Since several different microscopic mechanisms can cause linear dichroism in x-ray absorption, it is recommendable to discuss the different origins separately. First, the Natural Linear Dichroism is not caused by magnetism and can arise only if the crystalline symmetry is lower than cubic. The term *X-ray Magnetic Linear Dichroism* (XMLD) is a superset for different effects. It can be caused by spin-only effects via exchange-correlation, but also by magnetically (spin-) induced orbital effects via spin-orbit coupling. To summarize, XLD can be caused by:

1. Orbital ordering, i.e. a charge quadrupole moment (XNLD)
2. Spin-induced orbital moments via spin-orbit interaction
3. Orbitally-induced spin-moments via spin-orbit interaction
4. Pure spin effects (exchange-correlation)

2.2.2. X-ray Natural Linear Dichroism (XNLD)

X-ray Natural Linear Dichroism results from a charge quadrupole moment in the initial state, if the crystal symmetry is lower than cubic. In other words certain orbitals are selectively populated, because their energies become nondegenerate, when the symmetry is lowered. In most cases this orbital ordering is caused by a ligand- or crystal-field of lower than cubic symmetry, wherefore the XNLD is also often called *crystal-field dichroism*. The key to understand how linear dichroism works is to know that – in a one electron picture – by orienting the linear polarization \mathbf{e} in space, one can change the transition probability into certain orbitals, thereby probing their unoccupied density of states. One can directly find out the transitions with nonzero intensity, since quantum mechanics and group theory dictate that the parity condition must be fulfilled:

$$\langle f | C_q^{(1)} | i \rangle \neq 0 \Rightarrow P(f)P(C_q^{(1)})P(i) = \text{even} \quad . \quad (2.17)$$

The magnitude of the nonzero matrix elements is computed in analogy to Sec. 2.1, now with the linear polarization operator. Qualitatively, one can state the rule of thumb that the transition intensity will be higher, if \mathbf{E} points along a lobe feature of the final state orbital, and lower along a nodal feature (see Fig. 2.6). This rule of thumb was introduced originally by STÖHR and he called it the *search light effect*[151]. As a practical example, which is of value in our later investigations,

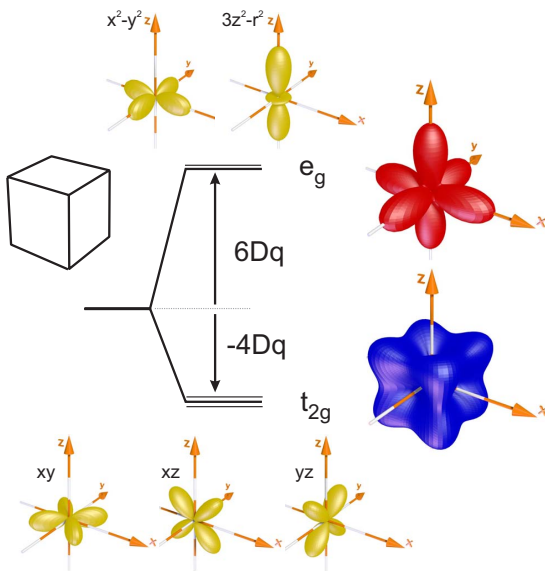


Figure 2.3: Crystal field splitting in a cubic crystal field. On the right hand side, the charge distribution in the irreducible e_g and t_{2g} representations is drawn separately, showing that each representation is of cubic symmetry. Note that the charge distribution in the two irreducible representations is complementary, which means that summing up the two contributions yields spherical symmetry – as is expected for a full shell. Note that electrons in the e_g orbitals are less strongly bound, since their orbit is oriented along the bond direction with the screening electronegative ligands. Conversely the t_{2g} electrons are more strongly bound, since their orbitals point away from the ligands.

we will consider here the crystal field dichroism of a Ni^{2+} ion in a tetragonal crystal field, for example with compression along the z -axis. Then the formerly degenerate orbitals in the e_g representation split into $a_1(d_{z^2}$, higher energy) and b_1

Figure 2.4: Crystal field splitting in a crystal field of tetragonal symmetry. Now the e_g representation splits up into a_1 and b_1 , the t_{2g} representation splits into e and b_2 . In the sketch, a vertical compression is assumed, thus the z^2 and xz, yz orbitals shift up in energy (less strongly bound), since the screening ligands are closer. Conversely, the $x^2 - y^2$ and xy orbitals shift down in energy, since the influence of the ligands gets weaker.

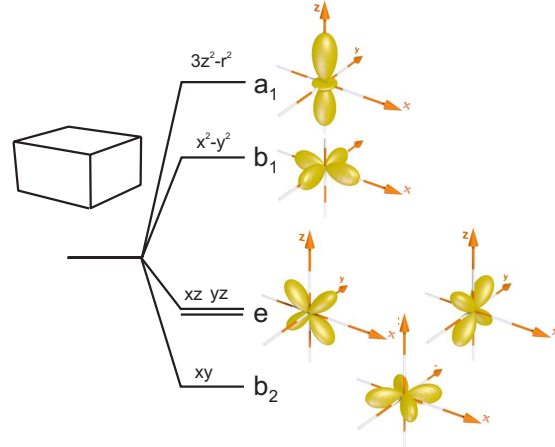
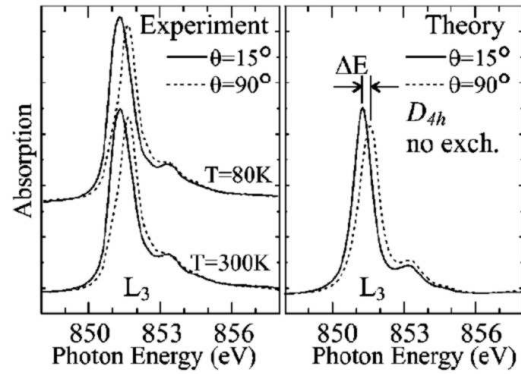


Figure 2.5: Shift of the L_3 peak energy due to a tetragonal crystal field in a strained NiO film on Ag[001] (Taken from [60]).



($d_{x^2-y^2}$, lower energy), while the t_{2g} orbitals split into two degenerate d_{xz}, d_{yz} (e) of higher energy and d_{xy} (b_2) of lower energy (see Fig. 2.4 for details). Assuming a high-spin d^8 state, only the d_{z^2} and $d_{x^2-y^2}$ states will contain holes, i.e. contribute to the XAS spectra. The E and b_2 representations will be completely filled and cannot be reached by optical transitions. Using the GAUNT-formula to calculate the transitions from the $p_{x,y,z}$ orbitals into the d-orbitals, one finds that only the following transitions produce nonvanishing intensity:

$$\begin{aligned}
 |\langle d_{z^2} | C_0^{(1)} | p_z \rangle|^2 &= \frac{4}{15} \\
 |\langle d_{x^2-y^2} | \frac{1}{\sqrt{2}} (C_{+1}^{(1)} + C_{-1}^{(1)}) | p_{x,y} \rangle|^2 &= \frac{3}{15} \\
 |\langle d_{z^2} | \frac{1}{\sqrt{2}} (C_{+1}^{(1)} - C_{-1}^{(1)}) | p_{x,y} \rangle|^2 &= \frac{1}{15} \quad . \quad (2.18)
 \end{aligned}$$

From this we can conclude that using z -polarized light, we probe the d_{z^2} -orbital exclusively. Using light polarized along x or y , we mainly probe the $d_{x^2-y^2}$ -orbital (75 %), but also d_{z^2} with a weight of 25 %. If now the two orbitals are split due to a tetragonal crystal field (see Fig. 2.4), the maximum transition intensity will shift

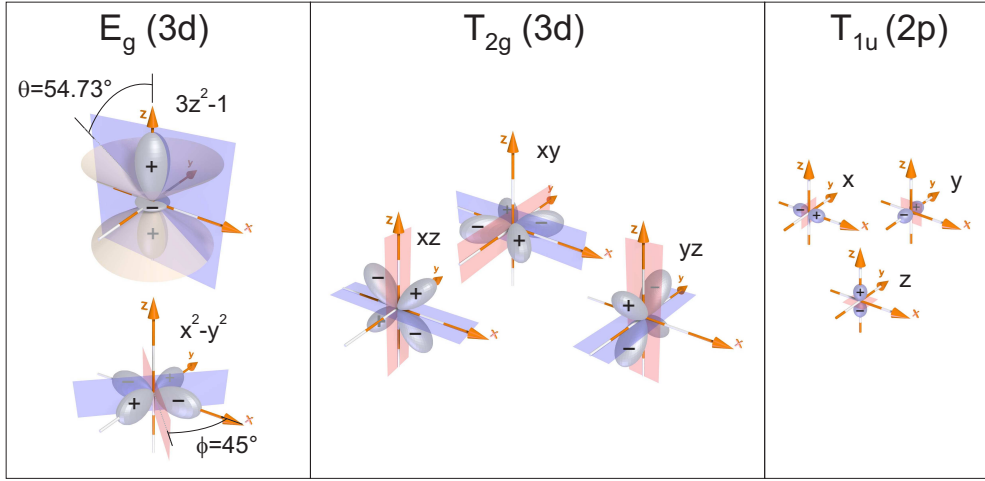


Figure 2.6.: Nodal features of the p- and d-orbitals. By orienting the linear polarization \mathbf{e} of the photons along certain lobe (nodal) features, transitions into certain d-orbitals can be enhanced (suppressed). The core hole will be polarized along the direction of \mathbf{e} .

in energy by approximately the amount of the splitting. This effect has been modelled and measured by HAVERKORT *et al.* [60] (see Fig. 2.5).

2.3. X-ray Magnetic Linear Dichroism (XMLD)

Historically, X-ray Magnetic Linear Dichroism has first been predicted in 1985 by THOLE *et al.* for the $M_{4,5}$ edges of rare earth materials with their localized 4f final states using atomic multiplet theory[154]. Experimentally, the effect was observed one year later by VAN DER LAAN *et al.* for the rare earth material $Tb_3Fe_5O_{12}$ (Terbium Iron Garnet, TbIG) [161]. The first experimental results for 3d transition metal compounds were reported in 1993 by KUIPER *et al.* for antiferromagnetic α - Fe_2O_3 [81]. In 3d transition metals, XMLD was not observed until 1998, where SCHWICKERT *et al.* found a small dichroism signal for Co, Fe, Cr and V [137].

2.3.1. X-ray Magnetic Linear Dichroism by exchange-correlation effects

To understand how magnetic linear dichroism arises from spin-only effects, we can apply again the simple model used already for the XMCD. We assume again

exchange split d-bands in a simple Stoner model, neglecting the crystallographic structure of the sample. Thus the symmetry of the problem will be axial. We will see later that there can be additional effects caused by the site symmetry of the excited atom due to its surrounding neighbours, which lead to the so-called *anisotropic* XMLD, i.e. the shape of the XMLD signal depends on both the orientation of the spin and the photon polarization with respect to the crystal lattice. In our simple model, the XMLD only depends on the angle between the magnetization and the polarization. Since the effect is observed with linearly polarized x-rays, we need the transition matrix elements for polarization parallel to \mathbf{M} , i.e. along z

$$\langle l+1 m_l | C_0^{(1)} | l m_l \rangle = \sqrt{\frac{(l+1)^2 - m_l^2}{(2l+3)(2l+1)}} \quad (2.19)$$

as well as for polarization perpendicular to \mathbf{M} , which can be constructed from Eq. 2.4 as

$$M_{fi}^{(xy)} = \frac{1}{\sqrt{2}} \langle f | C_{+1}^{(1)} + C_{-1}^{(1)} | i \rangle \quad . \quad (2.20)$$

To get the transition intensities depicted in Fig. 2.7, these elements need to be squared and multiplied by the square of the respective CLEBSCH-GORDAN coefficients, which are the same as for the XMCD. The resulting XMLD spectrum $I_{\parallel} - I_{\perp}$ is depicted in the center of Fig. 2.7. The signal closely resembles the energy-derivative of the XMCD signal, however, with a reversed sign at the L_2 edge. According to KUNEŠ and OPPENEER this is a direct consequence of the spherical symmetry of the d-DOS [82] and the core-valence exchange-interaction³.

The spectral integral over the XMLD is zero in this case, since we have neglected 3d spin-orbit coupling. Note that in order to observe XMLD in such a simple system, a sufficiently large energetic splitting of the core hole m_j sublevels is necessary, for example by *core-valence exchange interaction*. For the 3d transition metals, the exchange-splitting of the 2p core hole is in the order of 0.1 eV (for example 266 meV for fcc Co [82]), which makes the effect small ($\approx 1\%$ of the white line). Its observation therefore requires a soft x-ray beamline with good resolution, which is why the XMLD effect in transition metals was detected after the XMCD, and after the more pronounced XMLD in correlated materials. SCHWICKERT *et al.* measured the spectra for Co, Fe, Cr and V in 1998 by TEY XAS[137]. MERTINS *et al.* observed the X-ray magnetic VOIGT effect for

³KUNEŠ and OPPENEER expanded the spin-split unoccupied density of states functions f_{\uparrow} and f_{\downarrow} , which determine the XAS lineshape, into a Taylor series in terms of Δ_{pd} , considering only the linear term ($f(\omega \pm \Delta_{pd}) = f(\omega) \pm \frac{df}{d\omega} \Delta_{pd}$). Computing the XMLD difference spectrum then just yields the energy-derivative of the XMCD spectrum.

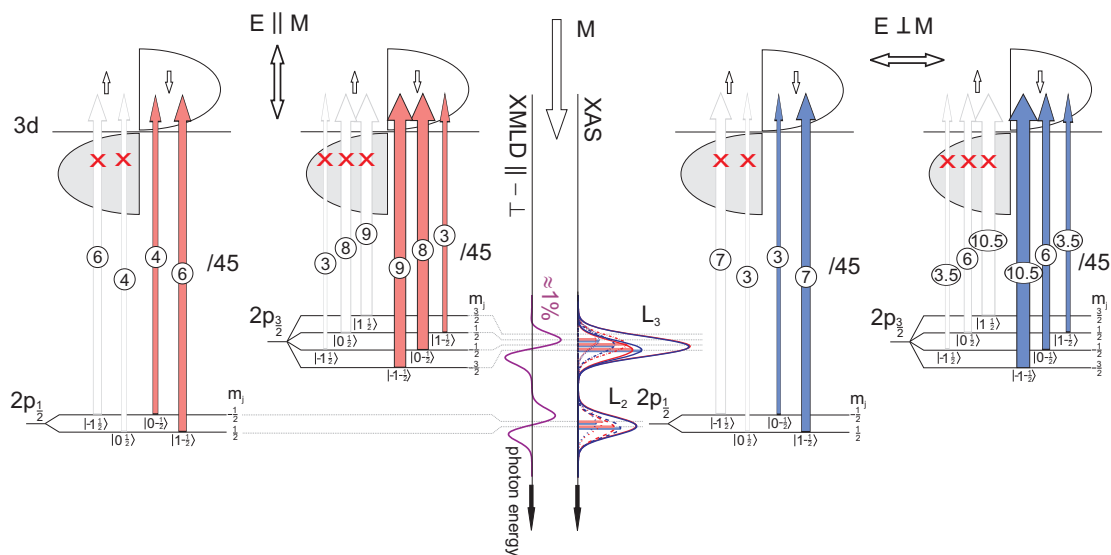


Figure 2.7.: XMLD single particle transition intensities with large exchange-splitting in the d-bands (majority band full).

Cobalt, i.e. the polarization rotation by Magnetic Linear Birefringence in transmission with transversal magnetization [98]. It should be emphasized that this simple model is insofar incomplete, as it introduces the exchange splitting of the core hole as a necessary "ingredient", but does not explain the intrinsic origin of this effect. A configuration interaction approach will lead to a more realistic – and more complicated picture: There, the polarized photon couples to the spatial part of the electron wave function, producing an orbitally polarized core hole, which will also have a spin-polarization due to the spin-orbit splitting. In the final state this core hole interacts via *exchange and correlation* effects with the target shell of the transition, which now contains one extra electron. Both effects together are responsible for the XMLD, and are generally related to the magnetic symmetry (crystal field + spin) of the sample.

2.3.2. XMLD in the presence of orbital degrees of freedom

A magnetic solid which has orbital degrees of freedom can exhibit a repopulation of atomic orbitals by spin-orbit interaction, if the spin is oriented along a particular direction. This effectively corresponds to an electric quadrupole moment, which is caused by and linked to the spin \mathbf{S} . For the cubic high-spin 3d transition metals, orbital degrees of freedom exist for all electronic configurations except high-spin d^3 , d^5 and d^8 . This can be understood qualitatively looking at Fig. 2.8. There, we have assumed that the exchange-splitting is larger than the crystal field

splitting and we have a high-spin ground state. It immediately becomes clear that in all configurations where the exchange-split e_g and t_{2g} subshells (or bands) are not exactly full, half-full or empty, additional holes or electrons exist, which can be located in any of the degenerate orbitals within their irreducible representation. If now the degeneracy is lifted or the orbitals are mixed by a perturbation, the electrons can be relocated, leading to a change in the charge distribution. Let's consider the simple example of a d^1 configuration in the case exchange $>$ crystal field $>$ $3d$ -spin-orbit interaction:

The t_{2g} spin-up subshell contains one electron, the latter can – without spin-orbit-interaction – be in any of the three degenerate d_{xy}, d_{xz}, d_{yz} orbitals, so the overall symmetry is cubic and no linear dichroism is produced. Now we switch on a small spin-orbit perturbation with a spin along \mathbf{z} , and assume for simplicity that due to the large $3d$ exchange interaction, thermally only the energetically most favourable $|j, m_j\rangle$ sublevels with $m_s = 1/2$ are occupied ($|5/2, 5/2\rangle$ and $|3/2, -3/2\rangle$). We can express the perturbed spin-orbit wavefunctions in terms of the (undisturbed) d-orbitals as follows [47, 146]:

$$\left| \frac{5}{2}, \frac{5}{2} \right\rangle = \frac{1}{\sqrt{10}} \frac{1}{\sqrt{5}} \{i |d_{xy} \uparrow\rangle + |d_{x^2-y^2} \uparrow\rangle\} \quad (2.21)$$

$$\left| \frac{3}{2}, -\frac{3}{2} \right\rangle = \frac{1}{\sqrt{10}} \{-2i |d_{xy} \uparrow\rangle + 2 |d_{x^2-y^2} \uparrow\rangle + i |d_{xz} \downarrow\rangle - |d_{yz} \downarrow\rangle\} \quad (2.22)$$

Since the spin-orbit interaction creates complex wavefunctions, a finite orbital moment is reestablished, whereas in the undisturbed case (cubic symmetry), the orbital moment was quenched. From the types of the mixed orbitals it directly becomes clear that spin-orbit interaction favours to orient the electrons within the xy -plane. This is equivalent to the creation of a charge quadrupole moment, i. e. linear dichroism can occur due to a charge symmetry lower than cubic. Since spin-orbit induced orbital mixing is one of the main sources of the magneto-crystalline anisotropy (MCA), x-ray absorption can also deliver information about the MCA. VAN DER LAAN derived a sum rule for linearly polarized XAS, which allows to extract the expectation value of the $3d$ spin-orbit interaction and also its anisotropy by varying the polarization direction [159]. This sum rule was confirmed experimentally by DHESI *et al.* [35]. Finally, it should be mentioned that the inverse effect, the orientation of the spin-moment by orbital ordering, has also been observed experimentally by HAVERKORT *et al.* [31]. There, a tetragonally expanded CoO layer (high-spin d^7) exhibits orbital relocation of the t_{2g} hole in the d_{xz} and d_{yz} orbitals, thereby orienting the spin-moment preferentially along the z -axis. In this case the distortion causes XNLD, but the spin-orbit interaction induces a spin-alignment and thus XMLD. Both contributions can in this case only be separated by temperature dependent measurements.

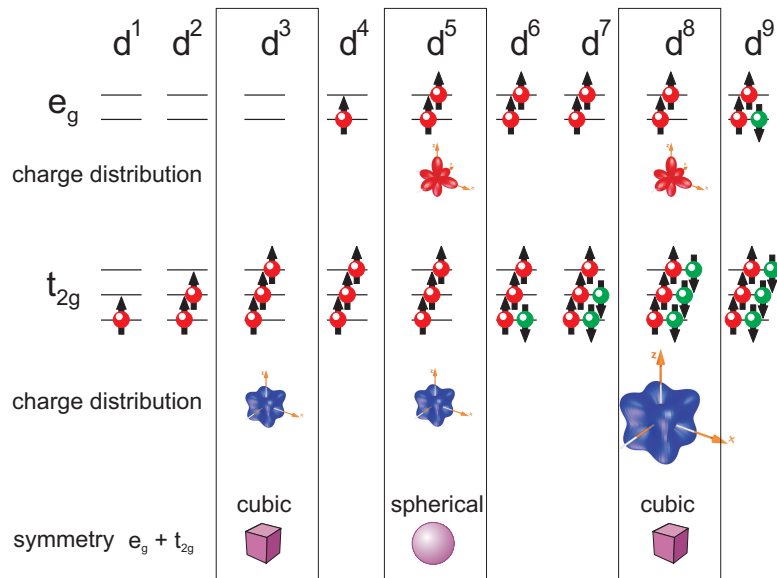


Figure 2.8.: 3d high-spin configurations in a cubic crystal field. The d^3 , d^5 and d^8 configurations are special, since they possess no orbital degrees of freedom. While d^5 is spherically symmetric with zero angular and orbital momentum, in both d^3 and d^8 , the e_g and t_{2g} subshells are exactly full or half full. All other configurations possess extra electrons or holes which can be relocated via spin-orbit interaction. This is the reason why the cubic d^3 , d^5 and d^8 configurations show only XMLD by exchange and correlation effects, (like, for example, NiO), while for other configurations the XMLD is caused both by spin-induced orbital ordering and exchange-correlation.

2.3.3. "Anisotropic" XMLD in 3d transition metal compounds

If the symmetry of the final states is not spherical anymore, the general XAS spectra cannot be described by means of a single angle anymore. While in the spherical case, the angle $\gamma_{\mathbf{E},\mathbf{S}}$ between \mathbf{E} and \mathbf{S} was sufficient to calculate an arbitrary XAS spectrum from two fundamental spectra, in the cubic case, the angles of \mathbf{E} ($\theta_{\mathbf{E}}, \phi_{\mathbf{E}}$) and \mathbf{S} ($\theta_{\mathbf{S}}, \phi_{\mathbf{S}}$) with respect to the *crystal basis frame* have to be considered. Whereas "isotropic" XMLD produces a single XMLD spectrum, which scales with $\cos^2(\gamma_{\mathbf{E},\mathbf{S}})$, the spectral shape and amplitude of "anisotropic"⁴ XMLD has a complicated dependence on the crystallographic angles of \mathbf{E} and \mathbf{S} .

⁴However, in the course of recent scientific publications, the terms "isotropic" and "anisotropic" XMLD have been introduced in order to differentiate between XMLD, which is independent of the material symmetry ("isotropic") and XMLD, which depends on the crystalline symmetry in the sample ("anisotropic"). In principle, XMLD is *by definition* an anisotropic quantity. Therefore, we use quotation marks for "isotropic" and "anisotropic" XMLD.

Simple picture

First, we will discuss the XMLD in the presence of a crystal field of cubic (O_h) symmetry, which causes a splitting of the 3d final states into an e_g and a t_{2g} irreducible representation. Now the "classic" rule of calculating the XMLD spectrum, namely $\mu_{\text{XMLD}} = \mu_{\mathbf{E} \parallel \mathbf{S}} - \mu_{\mathbf{E} \perp \mathbf{S}}$ makes only sense for two special spin-quantization axes, namely [001] (C_4) and [111] (C_3 -symmetry). Only for those cases, a unique $\mu_{\mathbf{E} \perp \mathbf{S}}$ -spectrum exists for arbitrary polarization-directions within the plane perpendicular to \mathbf{S} . For all other quantization axes, this method of calculating the XMLD is of little value, since the results are difficult to interpret. Consequently, Kuneš and Oppeneer [82] calculated the XMLD spectra for the aforementioned two different spin-quantization axes, for the transition metals (Fe, Co, Ni). They found that the XMLD spectra look different in both cases, which was explained in their model by a different weighting of transitions into final states belonging to e_g and t_{2g} representation, respectively. We will now briefly outline their model:

The starting point is again a spin-split, but spherical density of unoccupied states, i.e. zero crystal field. Spin-orbit interaction in the 3d states is not a necessary ingredient to explain anisotropic XMLD and can be neglected⁵. As mentioned earlier, XMLD can only be observed, if the core-levels are split by the *core-valence exchange-interaction* Δ_{pd} . This splitting was considered in a mean field picture of all the d-electrons producing an effective exchange-field acting on the core-electron spin:

$$\Delta_j = \frac{2}{3} \int r^2 R_j^2(r) b(r) dr \quad , j = \frac{1}{2}, \frac{3}{2} \quad (2.23)$$

Δ_j is taken into account by a first order approximation, treating the exchange-interaction as spherically symmetric, i. e. independent of the spin orientation with respect to the crystalline lattice. By the introduction of an exchange-splitting and the fixing of the spin direction, the formerly spherical symmetry is broken, and the quantization axis is consequently chosen along the spin direction. To describe the imaginary part of the dielectric tensor in terms of single-particle transition matrix elements, they applied the KUBO linear response theory and

⁵However, the accordance to experiment is improved by considering it. It is worth noting that, since the spin-orbit interaction is not a necessary ingredient for anisotropic XMLD, the term "magnetocrystalline anisotropy" used in [82] is somewhat misleading, when referring to the anisotropic nature of the XMLD due to the crystal symmetry. Since magnetocrystalline anisotropy is caused by the spin-orbit interaction, it is not a major origin of anisotropic XMLD

arrive at

$$\mu^q(\omega) = \text{Im}\{\epsilon^q(\omega)\} \propto \sum_{m,s} \alpha_{\gamma s}^q(j) f_{ms}(\omega \pm \frac{\gamma}{2}\Delta) \quad (2.24)$$

$$\frac{\gamma}{2} = m - q + s \quad (2.25)$$

$$q = 0, \pm 1 \quad \text{the polarization} \quad . \quad (2.26)$$

The f_{ms} are the d partial densities of unoccupied states (FERMI functions) and the $\alpha_{\gamma s}^q(j)$ denote the angular parts of the transition probabilities $2p_{j\gamma/2} \rightarrow 3d_{ms}$, which are the squared products of the CLEBSCH-GORDAN-coefficients and the transition matrix elements in $|C_{j\gamma/2|1m-q} 1/2 m_s \langle Y_{2m} | Y_{1q} | Y_{1m-q} \rangle|^2$, as already discussed before in Sec.2.1.2. The shift $\pm\gamma/2\Delta$ is caused by the core-valence-exchange-interaction and has different signs for L_2 (+) and L_3 (-) (see [151], Chapter 6.2.2). Approximating the FERMI-function by the linear part of a TAYLOR expansion around $\Delta = 0$, the energy-derivative of the FERMI-function enters the model:

$$f(\omega \pm \frac{\gamma}{2}\Delta) = f(\omega) \pm \frac{\gamma}{2}\Delta \frac{\partial f}{\partial \omega} \quad . \quad (2.27)$$

Calculating now the differences $\mu^{+1} - \mu^{-1}$ (XMCD) and $\mu_{\parallel} - \mu_{\perp} = \mu^{(0)} - 1/2(\mu^{+1} + \mu^{-1})$ (XMLD), one finds that

- the XMCD depends on the difference of the unoccupied partial DOS $\mu_{\text{XMCD}} \propto D_{\uparrow} - D_{\downarrow}$, as we have already seen before, and to first approximation it does not scale with Δ . Note that in experimental XMCD spectra, core-valence exchange interaction *does* change the shape of the spectra.
- the XMLD $\mu_{\text{XMLD}} \propto \Delta \frac{\partial}{\partial \omega} (D_{\uparrow} - D_{\downarrow})$ depends on the *energy derivative* of the unoccupied partial DOS and scales linearly with Δ .

Up to now, the crystalline symmetry is still spherical, and we have no "anisotropic" XMLD. But if a cubic crystal field is "switched on", the d-states will split into e_g and t_{2g} irreducible representations. The consequence is that for different spin directions, i.e. quantization axes, different combinations of the spin-split unoccupied DOS in the e_g and t_{2g} representations will be probed, consequently the XMLD looks like:

$$\mu_{\text{XMLD}} \propto \Delta \frac{\partial}{\partial \omega} \{ \alpha(t_{2g\uparrow} - t_{2g\downarrow}) + \beta(e_{g\uparrow} - e_{g\downarrow}) \} \quad . \quad (2.28)$$

For different quantization axes, the weighting factors will change, for example for $\mathbf{S}||[001]$ $\alpha = -1$, $\beta = 2$ and for $\mathbf{S}||[111]$, $\alpha = 1$, $\beta = -1$ [83]. It should be pointed out that this simple model accounts only for the two particular high-symmetry cases mentioned above, and that no general transformation of the XMLD for

arbitrary quantization axes is given here. Also, the crystal field splitting is assumed *ad-hoc*, and the effect of its size is not considered. Furthermore, the model contains assumptions, which are only true for the two special cases presented, and allow no general formulation [82]. Thus, the model is still not sufficient for vectorial magnetometry, where the XMLD must be predictable for arbitrary spin-quantization axes.

For a comprehensive theory, further aspects have to be taken into account. For example, the single-electron approach has to be replaced by a configuration-interaction picture, where exchange-correlation effects can be treated correctly. Atomic multiplet calculations can thus provide a more accurate picture, as will be shown later. Summarizing, "anisotropic" XMLD is caused by:

1. A crystal field, which lifts the spherical symmetry of the atomic potential.
2. Anisotropic exchange and correlation effects: In the XAS final state the core hole is orbitally polarized (polarized light!) and also spin-polarized due to the $2p$ spin-orbit interaction. It interacts via exchange-correlation effects Δ_{pd} and U_{pd} with the $3d$ states. If the crystalline symmetry is not spherical, Δ_{pd} and U_{pd} will strongly depend on the orientation of the spin-quantization axis.
3. Orbital moment anisotropy: The anisotropy of the $3d$ spin-orbit interaction $\langle \xi_a^{(3d)} \rangle$ and consequently the orbital moment, i.e. the magnetocrystalline anisotropy. Depending on the spin orientation, the orbital moment will generally not be parallel to the spin-moment and also vary in size. In cubic symmetry, both the orbital moment and the spin-orbit interaction in the d -states are small ($m_{\text{orb.}} \approx 0.1 \mu_B$ and $E_{\text{s.o.,d-band}} \propto \frac{\xi_{\text{s.o.}}^4}{W_{\text{d-band}}} = 1 \mu\text{eV/atom}$), so this is only a minor contribution to the XMLD. Nevertheless, sum rule analysis of XMLD spectra as described by VAN DER LAAN *et al.* [159] allows the extraction of the orbital moment anisotropy $\langle \xi_a \rangle$. However, the anisotropies determined in that way are generally much larger than the experimental values and hence not useful to determine the MCA quantitatively.

2.3.4. Angular dependence of XMLD - a phenomenological description

In the following we will try to provide a classic derivation of the "isotropic" XMLD due to a magnetically induced charge quadrupole moment rotating along with the spin. For simplicity, we will consider nongyrotropic media (no XMCD)

with $\mathbf{g} = 0$ (see Eq. 1.12). The formula will then be compared to the angular dependence of the "anisotropic" XMLD found by atomic multiplet calculations.

2.3.5. "Isotropic" XMLD

In the following, we will classically derive the linear dichroism caused by an electric quadrupole moment $\hat{\mathbf{Q}}$ in the ground state, which, for example, is induced via spin-orbit interaction when orienting the spin in an external field. We further make the simplifying assumption that the magnetic anisotropy in the sample is low, i.e., the crystal field and the anisotropy of the spin-orbit interaction is negligible. Then the orbital and spin-moment will be approximately parallel, along the external field direction. In that case, the quadrupole moment $\hat{\mathbf{Q}}$ will follow the spin orientation and its size q will be proportional to the square of the magnetic moment M^2 .

For a system with cubic or higher symmetry without any optical activity, the dielectric tensor will look like

$$\hat{\epsilon}_{\text{iso}} = \begin{bmatrix} \epsilon_{xx} & 0 & 0 \\ 0 & \epsilon_{xx} & 0 \\ 0 & 0 & \epsilon_{xx} \end{bmatrix}, \quad (2.29)$$

and the sample will be optically isotropic. If the crystal symmetry is now reduced below cubic by a magnetic spin-quantization axis, which can be arbitrarily oriented, the problem gets more complicated. However, two fundamental elements of $\hat{\epsilon}$ are sufficient to describe $\hat{\epsilon}$ for all possible orientations of \mathbf{S} .

Since the XMLD may be caused by a (magnetically induced) charge quadrupole moment, we hypothetically represent it by a tensor of rank $k=2$, called the *quadrupole tensor*, which is defined as [46]

$$\begin{aligned} \hat{\mathbf{Q}} &= \begin{bmatrix} Q_{xx} & Q_{xy} & Q_{xz} \\ Q_{xy} & Q_{yy} & Q_{yz} \\ Q_{xz} & Q_{yz} & Q_{zz} \end{bmatrix} \\ &= \begin{bmatrix} 1 - 3x^2 & -3xy & -3xz \\ -3xy & 1 - 3y^2 & -3yz \\ -3xz & -3yz & 1 - 3z^2 \end{bmatrix}, \end{aligned} \quad (2.30)$$

where $\mathbf{S} = (x, y, z)$ is the unit vector along the spin quantization axis. Note that the quadrupole tensor is symmetric and trace-free ($Q_{xx} + Q_{yy} + Q_{zz} = 0$). In the

presence of linear dichroism, $\hat{\epsilon}$ can be written as a combination of the isotropic and quadrupole part like

$$\hat{\epsilon} = \hat{\epsilon}_{\text{iso}} + q \cdot \hat{\mathbf{Q}} \quad (2.31)$$

$$\hat{\epsilon} = \begin{bmatrix} \epsilon_{xx} + q(1 - 3x^2) & -3qxy & -3qxz \\ -3qxy & \epsilon_{xx} + q(1 - 3y^2) & -3qyz \\ -3qxz & -3qyz & \epsilon_{xx} + q(1 - 3z^2) \end{bmatrix} \quad (2.32)$$

Orienting \mathbf{S} along the \mathbf{z} direction makes $\hat{\epsilon}$ diagonal, with only two independent elements:

$$\begin{aligned} \hat{\epsilon}(\mathbf{S}||\mathbf{z}) &= \begin{bmatrix} \epsilon_{xx} + q & 0 & 0 \\ 0 & \epsilon_{xx} + q & 0 \\ 0 & 0 & \epsilon_{xx} - 2q \end{bmatrix} \\ &= \begin{bmatrix} \epsilon_{\perp} & 0 & 0 \\ 0 & \epsilon_{\perp} & 0 \\ 0 & 0 & \epsilon_{\parallel} \end{bmatrix} . \end{aligned} \quad (2.33)$$

Consequently, orienting the spin along the \mathbf{x} direction, we will get:

$$\hat{\epsilon}(\mathbf{S}||\mathbf{x}) = \begin{bmatrix} \epsilon_{\parallel} & 0 & 0 \\ 0 & \epsilon_{\perp} & 0 \\ 0 & 0 & \epsilon_{\perp} \end{bmatrix} . \quad (2.34)$$

Using linear polarization along \mathbf{z} , the two independent elements ϵ_{\parallel} and ϵ_{\perp} can be measured in the geometries $(\mathbf{S}||\mathbf{E}||\mathbf{z})$ and $(\mathbf{x}||\mathbf{S} \perp \mathbf{E}||\mathbf{z})$, respectively. The corresponding XAS spectra are the *fundamental spectra*. Since the dielectric tensor has the same angular dependence as the quadrupole moment, it can now be computed for arbitrary orientations of $\mathbf{S} = (x, y, z)$:

$$\hat{\epsilon}_{\text{MLD}} = \begin{bmatrix} \epsilon_{\perp} + (\epsilon_{\parallel} - \epsilon_{\perp})x^2 & (\epsilon_{\parallel} - \epsilon_{\perp})xy & (\epsilon_{\parallel} - \epsilon_{\perp})xz \\ (\epsilon_{\parallel} - \epsilon_{\perp})xy & \epsilon_{\perp} + (\epsilon_{\parallel} - \epsilon_{\perp})y^2 & (\epsilon_{\parallel} - \epsilon_{\perp})yz \\ (\epsilon_{\parallel} - \epsilon_{\perp})xz & (\epsilon_{\parallel} - \epsilon_{\perp})yz & \epsilon_{\perp} + (\epsilon_{\parallel} - \epsilon_{\perp})z^2 \end{bmatrix} \quad (2.35)$$

Note that replacing $\epsilon_{\parallel} = -2$ and $\epsilon_{\perp} = 1$, one recovers exactly the definition of the quadrupole tensor, i.e. this pair of values corresponds to a purely quadrupolar charge distribution. Comparison of Eq. 2.35 to the general dielectric tensor in cubic symmetry given in Eq. 1.11, one can identify $\gamma_{12} = \epsilon_{\perp}$, $\gamma_{11} = \epsilon_{\parallel}$ and $\gamma_{44}^{(\text{iso})} = +(\epsilon_{\parallel} - \epsilon_{\perp})$. Following the "standard rule" for the calculation of XMLD spectra, namely

$$\mu_{\text{MLD}} = \mu(\mathbf{S}||\mathbf{E}) - \mu(\mathbf{S} \perp \mathbf{E}) \quad , \quad (2.36)$$

we will now always yield the difference of the two fundamental spectra, no matter in which direction \mathbf{S} is pointing:

$$\mu_{\text{MLD}} = \epsilon_{\parallel} - \epsilon_{\perp} \propto q \propto \mathbf{M}^2 \quad , \quad (2.37)$$

\mathbf{M}^2 being the squared magnetization in the sample.

Conclusion: Deriving the XMLD from a quadrupole moment that is locked to the spin direction and does not change its magnitude would imply that the XMLD in cubic or higher symmetry would *only* depend on the *relative* orientation of \mathbf{E} and \mathbf{S} , but *not* on the *crystalline* orientations of \mathbf{E} and \mathbf{S} !. Consequently the "anisotropic" XMLD found experimentally indicates that the situation is more complicated: In general, the charge quadrupole moment is not locked to the spin orientation and additional effects like exchange-correlation are present.

2.3.6. "Anisotropic" XMLD in cubic symmetry

Interestingly, in O_h symmetry one finds both experimentally and by atomic multiplet calculations that XMLD caused by exchange-correlation effects is "anisotropic", i.e. depends on the orientations of both \mathbf{E} and \mathbf{S} relative to the cubic basis frame (and *not* on their relative orientation only). As calculations show, however, still two fundamental spectra are sufficient to describe the effect for arbitrary directions of \mathbf{S} . The approximate⁶ angular transformation of the dielectric tensor as found from the calculations [59] looks as follows:

$$\hat{\epsilon}_{\text{MLD}} = \begin{bmatrix} \epsilon_{\perp} + (\epsilon_{\parallel} - \epsilon_{\perp})x^2 & -(\epsilon_{\parallel} - \epsilon_{\perp})xy & -(\epsilon_{\parallel} - \epsilon_{\perp})xz \\ -(\epsilon_{\parallel} - \epsilon_{\perp})xy & \epsilon_{\perp} + (\epsilon_{\parallel} - \epsilon_{\perp})y^2 & -(\epsilon_{\parallel} - \epsilon_{\perp})yz \\ -(\epsilon_{\parallel} - \epsilon_{\perp})xz & -(\epsilon_{\parallel} - \epsilon_{\perp})yz & \epsilon_{\perp} + (\epsilon_{\parallel} - \epsilon_{\perp})z^2 \end{bmatrix} \quad (2.38)$$

Comparison of Eq. 2.35 to the general dielectric tensor in cubic symmetry given in Eq. 1.11 now yields $\gamma_{12} = \epsilon_{\perp}$ and $\gamma_{11} = \epsilon_{\parallel}$ as for the "isotropic" XMLD, but $\gamma_{44}^{(\text{aniso})} = -(\epsilon_{\parallel} - \epsilon_{\perp})$. The *nondiagonal elements* now have a *negative sign*, which is why the XMLD manifold, i.e. the set of all XMLD spectra for all possible polarizations does not rotate along with \mathbf{S} any more. Currently, the origin of this property cannot be properly explained, but the findings are consistent with measurements and atomic multiplet calculations for various spin quantization axes [82, 83, 32, 8, 9, 77].

Fundamental spectra and important symmetry properties

In Fig. 2.9, the fundamental spectra calculated by HAVERKORT for 0 K are shown for the two cases $C_4^z \parallel \mathbf{S} \parallel \mathbf{E}$ (I (0°)) and $C_4^z \parallel \mathbf{E} \perp \mathbf{S} \parallel C_4^x$ (I(90°)). Clearly, the

⁶Interestingly, the angular transformation is *nearly*, but not *exactly* correct. The degree of deviation depends on crystal field and exchange energies as well as the overall electronic structure in the d-states.

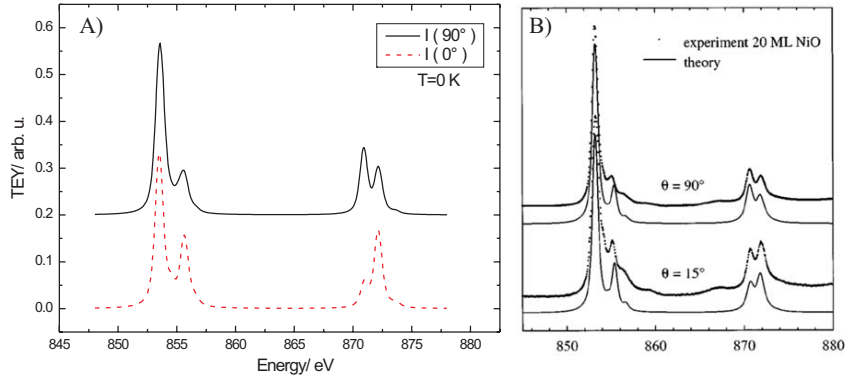


Figure 2.9.: Fundamental spectra. (A) Calculations of HAVERKORT for $T = 0$ K. From these two spectra, it is possible to compute XAS spectra for arbitrary orientations of \mathbf{S} and \mathbf{E} (at 0 K). (B) Experimental results of ALDERS *et al.* for MgO(001)/NiO[20 ML] at room temperature. Coincidentally, ALDERS *et al.* had a NiO domain distribution with only $[\pm 1 \pm 1 \pm 2]$ -type spin-axes, which yields an XMLD signal axially symmetric to the sample normal due to integration over a large number of domains. This is why in their work, the anisotropic nature of the XMLD in single crystalline samples remained undetected [2].

redistribution of spectral weights between the multiplet-split double peaks can be seen. Furthermore, the direction of the weight-transfer is the same for both edges. Comparing to the results of ALDERS *et al.*, the situation is quite similar, however, not as pronounced due to the elevated temperature (300 K) and the fact that a polarization angle of 0° with the sample normal is unfeasible (where should the light come from?). The particular domain distribution in their strained NiO layers on MgO(001) lead to a preference of only $[\pm 1 \pm 1 \pm 2]$ -type spin-axes. Since the experiment was not spatially resolved, the integration over a large number of domains yielded an XMLD characteristics, which was axially symmetric about the sample normal. This is why they could successfully describe the XMLD by an angular dependence of $\cos^2 \angle(\mathbf{E}, \mathbf{n})$, where \mathbf{n} is the sample normal, or, so to speak, an *effective spin-axis*. This is the main reason, why the anisotropic nature of the XMLD in their epitaxial samples remained undetected, because the geometry was similar to the highly symmetric case $\mathbf{S} \parallel C_4$. Generally, one cannot hope to find exactly such a domain distribution, and indeed the simple relation does not hold true in the general case. Many results based on this theory have to be reconsidered, and indeed some of them have already been proven incorrect (see, for example, comments in Ref. [9]).

The first and most important thing in this context is to notice, that the simple rule of calculating "XMLD" spectra, namely Eq. 2.36, in general is not a good choice when dealing with anisotropic XMLD. This is because for arbitrary orientations of \mathbf{S} , there is generally not a unique spectrum for $\mathbf{E} \perp \mathbf{S}$ anymore. Only for the special cases $\mathbf{S} \parallel \langle 111 \rangle$ -type directions and $\mathbf{S} \parallel \langle 001 \rangle$ -type directions the standard rule is recovered. Then and only then, the MLD can be described as a simple $\cos^2(\mathbf{E}, \mathbf{S})$ dependence, as done by ALDERS *et al.* [2]. For all other cases, the situation is unnecessarily complicated when considering differences of two XAS spectra. It is therefore better to use a single XAS spectrum for each geometry, and compare it to atomic multiplet calculations.

In the following, we will now take a closer look at the symmetry properties of the "anisotropic" XMLD. Although, in principle, the system may possess no symmetry at all for an arbitrary spin-quantization axis, one finds that the manifold of XAS spectra for fixed spin direction and arbitrary polarization directions $\mathfrak{M}_{\mathbf{S}}(\mathbf{E})$ generally retains a minimal symmetry, even when the spin does not point along any symmetry direction. This minimum symmetry can be generally described as *mmm* (orthorhombic with inversion centre) (see, for example, the case $\mathbf{S} \parallel [112]$ in Fig. 2.10). This means that XAS measurements along at least three linearly independent polarization directions (ideally along the main axes) allow for a complete determination of the manifold.

Even a complete experimental determination of the XMLD manifold, however, leaves some ambiguity for the spin-axis orientation. Exchanging \mathbf{S} and \mathbf{E} in Fig. 2.10, we can, for example, consider the worst case, namely $\mathbf{E} \parallel [100]$. Then, for all orientations of \mathbf{S} on a cone around the $[100]$ -axis, the same value will result, and only the angle of \mathbf{S} with the $[100]$ -axis can be derived. To find out the actual spin orientation, additional information has to be provided, for example known easy-directions in the material or the confinement of the spins within the sample plane by dipolar (shape-)anisotropy. Generally, choosing \mathbf{E} along non-high-symmetry-directions and measuring along as many different directions as possible reduces the ambiguity by the aforementioned symmetry-reduction of the XMLD manifold.

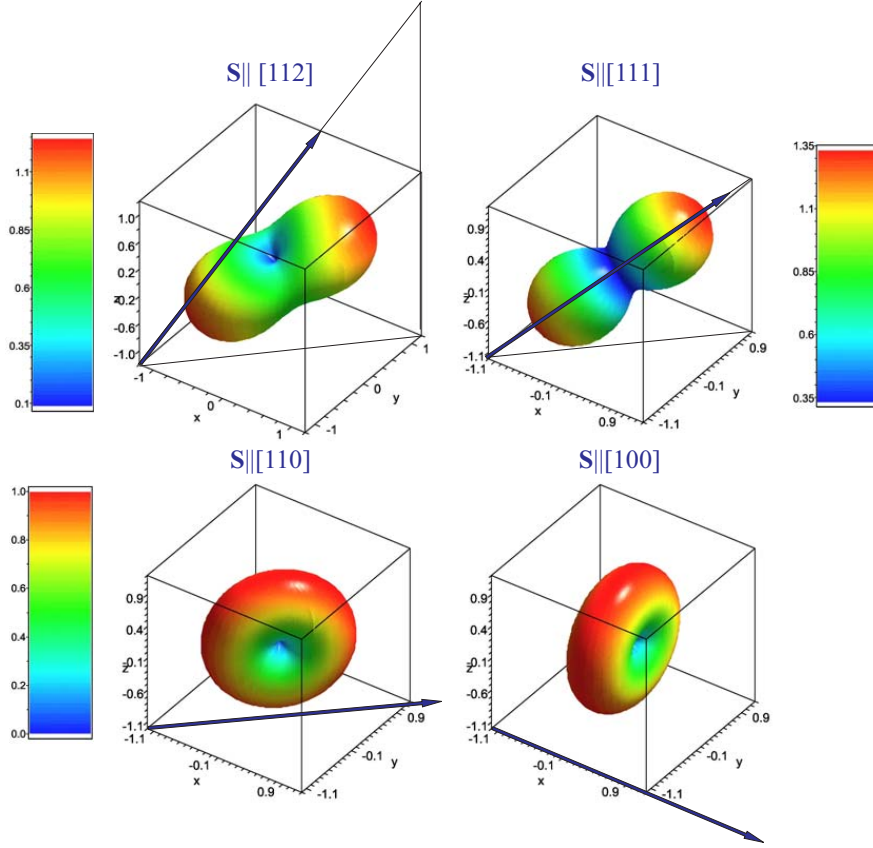


Figure 2.10.: Polarized-XAS-manifold $\mathfrak{M}_{\mathbf{S}}(E)$ in cubic symmetry for several fixed spin directions. The manifold is calculated by setting $\epsilon_{\parallel} = 0$ and $\epsilon_{\perp} = 1$ and represents the XAS intensity at a given energy for the full solid angle of polarization orientations. From the plots, it is directly apparent that the manifold possesses rotation symmetry around the spin direction only for the two cases $\mathbf{S} \parallel \langle 111 \rangle$ and $\mathbf{S} \parallel \langle 100 \rangle$. Thus only for those directions the classical calculation of the XMLD signal makes sense. For a general spin orientation, the symmetry is mmm . Note that in cubic symmetry, \mathbf{E} and \mathbf{S} commute, which means that the manifolds are the same when interchanging both vectors ($\mathfrak{M}_{\mathbf{S}}(\mathbf{E}) = \mathfrak{M}_{\mathbf{E}}(\mathbf{S})$).

3. Transition Metal Oxides - Electronic and magnetic properties

3.1. NiO: Electronic structure and magnetic interactions

NiO is an antiferromagnetic charge transfer isolator with a cubic rocksalt structure above its NÉEL temperature of 523-5 K (lattice parameter $a=4.176 \text{ \AA}$) [103, 148, 95]. If we make the simplifying assumption of NiO being an ionic crystal, it has the formula $\text{Ni}^{2+}\text{O}^{2-}$. The Ni cations are then in a $3d^8$ ground state. In the free ion we can apply HUND's rules and obtain a ground state 3F_4 ($S=1, L=3, J=4$). Neglecting the magnetoelastic distortions, which will be discussed in the next section, we can approximate the crystal field as octahedral O_h . The 3d states are then separated into two irreducible representations e_g and t_{2g} , of which the t_{2g} representation possesses the lower energy (compare Fig. 2.3). Assuming a high-spin ground state (first HUND's rule still applicable), we end up with a filled t_{2g} subshell and two spin-up electrons in the e_g orbitals ($d_{x^2-y^2}^\uparrow d_{z^2}^\uparrow$), which add up to $S = 1$.

Taking HUND's second rule for granted, we still have $L = 3$ and the possible irreducible representations are then $A_2 + T_1 + T_2$. Multiplet ligand field theory finally yields that 3A_2 has the lowest energy [151]. Since NiO is an insulator, all itinerant or direct interactions to convey a magnetic order are weak, leaving as only effective mechanism the so-called superexchange, i.e. the hopping of electrons between two cations via a ligand bond [5]. In the case of NiO, the $3d e_g$ orbitals have a good overlap with the oxygen $2p t_{1u}$ orbitals. Since the latter are occupied by two electrons with antiparallel spins according to the PAULI principle, the formation of a covalent bond with a cation on either side of the

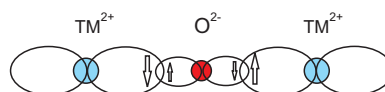


Figure 3.1.: 180° superexchange interaction.

oxygen atom leads to antiparallel spin alignment of the neighbouring cations (see Fig. 3.1).

3.2. Antiferromagnetic structure and magnetoelastic domains in NiO

Below the NÉEL temperature, the crystal will exhibit antiferromagnetic ordering due to the 180° superexchange interaction discussed in the previous section. The rocksalt structure then leads to ferromagnetic (111) planes which are stacked antiferromagnetically along the corresponding [111]-direction (AF II-structure, [139]). The easy axis within those planes have been determined to be the $\langle 11\bar{2} \rangle$ -type directions [74, 103], i.e. the spins are confined to the (111)-planes. Since there are four $\langle 111 \rangle$ -type directions and three easy directions for each (111) plane, in total 12 *antiferromagnetic domains* are possible within the crystal: Four so-called (T)win-domains classified by the corresponding AF stacking vector and within each T-domain three (S)pin-domains for the three easy axes. In principle,

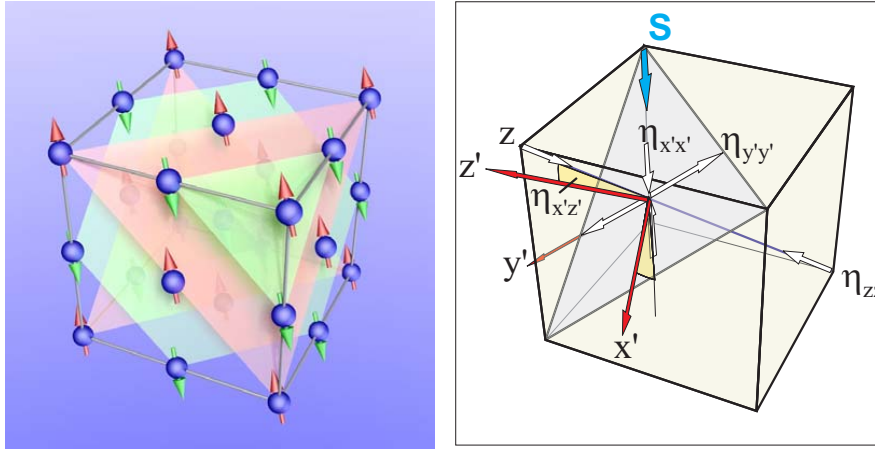


Figure 3.2.: Left: Antiferromagnetic structure of NiO with ferromagnetic (111) sheets (oxygen atoms not shown). Right: magnetoelastic distortions.

without further interactions, any crystal can be in an arbitrary multidomain state. However, NiO exhibits pronounced exchange- and magnetostriction, which puts further limits to the possible domain configurations. Upon antiferromagnetic ordering, a single domain crystal, let's say, with stacking along [111] will exhibit several distortions: The largest one is rhombohedral with a relative size of $\eta_{zz} = -1.5 \cdot 10^{-3}$ as shown in Fig. 3.2 [140], which is caused by *exchange-striction*, i.e.

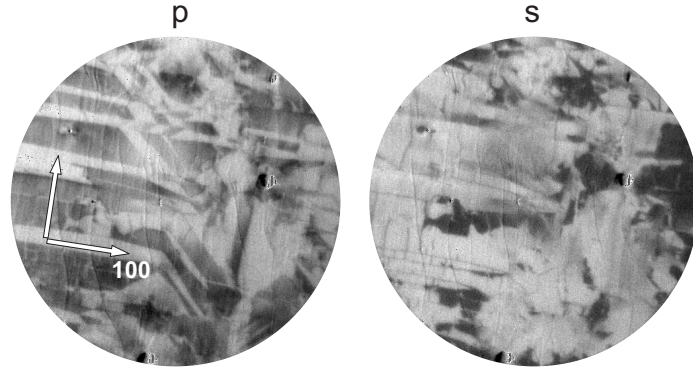


Figure 3.3.: PEEM images of antiferromagnetic domains at the (001) surface of a freshly cleaved NiO single crystal (measured at the SLS, Switzerland). In p-contrast, the domains bounded by walls running along $\langle 100 \rangle$ and $\langle 110 \rangle$ -type directions are clearly visible. In s-contrast, the walls along $[100]$ ($[010]$) become visible as dark (bright) lines.

the dependence of the superexchange constant on internuclear distance $\frac{\partial J}{\partial r} \approx -4 \mu\text{eV}\text{\AA}^{-1}$ [171].

For the remaining distortions, it is convenient to introduce a coordinate system adapted to the new symmetry of the crystal, which would be defined as $\mathbf{z}' \parallel [111]$, $\mathbf{x}' \parallel [11\bar{2}]$ || \mathbf{S} the spin axis and $\mathbf{y}' \parallel [1\bar{1}0]$ perpendicular to the spin axis. The dipolar anisotropy and magnetostriction within the ferromagnetic sheets will then lead to a contraction along the spin axis of $\eta_{x'x'} = -2.7 \cdot 10^{-4}$ and an expansion of $\eta_{y'y'} = +2.7 \cdot 10^{-4}$ perpendicular to it. Last but not least there will be a canting of the $[111]$ axis towards the spin axis of $\eta_{x'z'} = 0.91 \cdot 10^{-4}$, making the overall symmetry monoclinic. In real crystals, the magnetoelastic distortions together with the sample shape and defects will generally lead to a metastable multidomain state.

3.2.1. Antiferromagnetic Domain walls

The possible walls separating two domains have to comply to stress compatibility, i.e. the condition

$$\hat{\boldsymbol{\eta}} = -\mathbf{n} \times (\hat{\mathbf{e}}_1 - \hat{\mathbf{e}}_2) \times \mathbf{n} \stackrel{!}{=} 0 \quad (3.1)$$

must be fulfilled, where $\hat{\mathbf{e}}_{1,2}$ are the spontaneous strain tensors on both sides of the wall and $\mathbf{n} = [x, y, z]$ is the unit wall normal [167]. In this case there will be no contribution to the elastic energy $\hat{\boldsymbol{\eta}} \hat{\mathbf{c}} \hat{\boldsymbol{\eta}}$. As an example, we will consider here a

wall between a T_1 ($[111]$) and T_2 ($[\underline{1}11]$) domain. Then we get

$$\hat{\boldsymbol{\eta}} \propto \begin{bmatrix} 0 & -2z^2 + 2yz & 2yz - 2y^2 \\ -z(2z - 2y) & -4zx & 2zx + 2xy \\ y(2z - 2y) & 2zx + 2xy & -4xy \end{bmatrix}, \quad (3.2)$$

and $\hat{\boldsymbol{\eta}} = 0$ for \mathbf{n} along $[100]$ or $[011]$, which define *mirror planes* of the two domains. In a similar fashion, (001)- and (110)-type mirror planes are obtained for the other T-domains. YAMADA showed, that for the walls separating two different S-domains within the same T-domain two orientations are possible. For example, the boundary between $[11\bar{2}]$ and $[\bar{1}21]$ domains can run along the (110) or the $(2\bar{1}1)$ plane. The latter has not been observed experimentally, possibly because it is not fully compatible to the crystal symmetry due to the monoclinic deformation $\eta_{x'z'}$. Of course, the transition zones between different antiferromagnetic domains

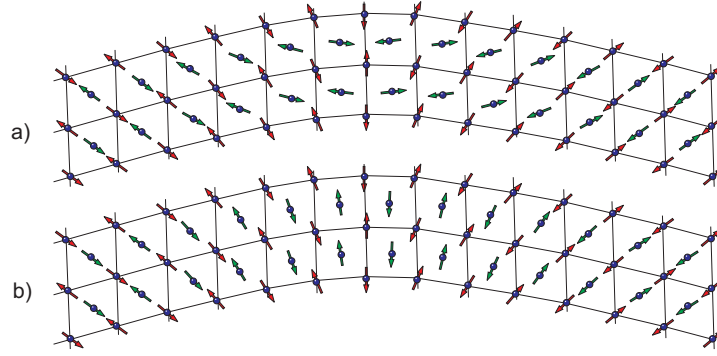


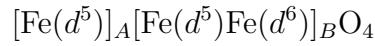
Figure 3.4.: Structure of a hypothetical 90° -wall inside of NiO. (a) model after YAMADA [171] with anticyclic rotation, (b) coherent rotation of both sublattices. The magnetoelastic distortion has been exaggerated. In (a), the wall core exhibits a strongly noncollinear magnetic structure, which would lead to a higher pseudodipolar energy than the configuration shown in (b), where an essentially collinear spin-alignment is retained throughout the wall. Our results in Chap. 8 indicate that type (b) is realized in the constrained AF domain walls of an epitaxial NiO layer exchange coupled to magnetite.

are not infinitely narrow, but the change in magnetic (and crystalline) structure will take place over a finite distance in the solid. The physics of the naturally occurring magnetoelastic domain walls in NiO was the subject of several theoretical studies by YAMADA [171, 173, 172, 174]. It should be pointed out that the anticyclic rotation of both sublattices inside the wall – as postulated by YAMADA – has never been confirmed experimentally, and furthermore contradicts intuition, since the resulting noncollinear spin-alignment inside the wall-core would lead to a high pseudodipolar energy. A more likely scenario is the rotation of both

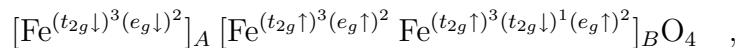
sublattices as a "rigid" spin-axis. This model has been successfully applied to describe the wall profiles at the NiO (001) surface [167]. Experimentally, an upper limit of 160 nm was found for the width of T-walls, in contrast to the postulation of only 8 nm made by YAMADA. For the S-walls, a larger value of 200 nm was found, which is consistent with the lower in-plane anisotropy for rotations of the spins within the ferromagnetic (111)-planes. It should be noted that in contrast to the magnetoelastic walls described here, chapter 8 deals with another type of antiferromagnetic domain wall, which is induced in a thin AF layer by the interfacial exchange coupling to a ferrimagnet (Fe_3O_4), which thereby imprints its domain pattern into the antiferromagnet. Since the thin AF layer must obey the strain boundary conditions dictated by the substrate, the walls are not dominated by magnetoelastic effects anymore but rather by exchange interaction and magnetocrystalline anisotropy, just as ferromagnetic domain walls. One important difference is, however, that stray fields don't play a role in the minimization of the wall energy.

3.3. Fe_3O_4 : Electronic and magnetic structure

Magnetite crystallizes in the inverse spinel structure. In a simple ionic picture, it has the formula $[\text{Fe}^{3+}]_A[\text{Fe}^{3+}\text{Fe}^{2+}]_B\text{O}_4^{2-}$, or



i.e. the Fe^{3+} ions occupy the tetrahedral (A) sites and half of the octahedral (B) sites. The lattice constant is 8.396 Å [53] and thus almost twice as large as the one of NiO. Below 120 K (VERWEY temperature T_V) it exhibits a transition from the high-temperature conducting to the low-temperature insulating phase (for a review see [165, 49] and references therein). This metal-insulator transition, which coincides with a monoclinic distortion, is thought to be accompanied by charge ordering mainly on the octahedral sites, thereby preventing the hopping mechanism between Fe^{2+} and Fe^{3+} cations that leads to the finite conductivity. All cations are in a high-spin state, and the A and B sites interact with each other by 124.5°-superexchange via an oxygen atom, which orients their net moments antiparallel. The B-site cations interact by ferromagnetic 90° *double-exchange* via oxygen [6]. The 3d electronic configuration is thus



resulting in a net spin moment of $4\mu_B$. Experimentally, a spin-moment close to $4\mu_B$ has indeed been found [169, 50].

This means that the electrical conductivity by electron hopping on B sites has almost purely minority spin character, i. e. Fe_3O_4 is a ferrimagnetic *half-metal* with ideal properties for spin-electronics. The CURIE temperature is ≈ 850 K and the magnetic anisotropy constant $K_1^- = -1.1 \cdot 10^4 \text{ Jm}^{-3}$, thus the bulk easy-directions are along $\langle 111 \rangle$ [87].

In the iron-oxide system, there are other phases with different physical properties, which we will discuss here for the sake of completeness. It is important to know their properties and the conditions for their formation, in order to be able to prepare samples with the right stoichiometry and interpret the effects of surface reconstruction.

When going towards lower oxygen content, there is Fe_{1-x}O (Wüstite), which is a rocksalt-type antiferromagnetic insulator ($T_N \approx 198$ K) with a lattice constant of $a = 4.305 \text{ \AA}$. In its single-domain state it orders – similar to NiO – with ferromagnetic sheets stacked along $\langle 111 \rangle$, but the spins also pointing along the stacking axis [88]. Wüstite is nonstoichiometric with defect clusters in the cation lattice, which locally resemble the structure of Fe_3O_4 [164].

For higher oxygen content, two phases are possible, namely $\gamma\text{-Fe}_2\text{O}_3$ (Maghemite) and $\alpha\text{-Fe}_2\text{O}_3$ (Hematite). Maghemite ($\gamma\text{-Fe}_2\text{O}_3$) has the same inverse spinel structure as magnetite, however with only one type of cation on the B sites, namely Fe^{3+} . For the sake of charge neutrality, vacancies are introduced, which also reside mainly on the B lattice, so one can write $\text{Fe}_A^{3+}[\text{Fe}_{5/3}^{3+}]_B\text{O}_4$ or $\text{Fe}_{2.67}\text{O}_4$. Varying the number of vacancies per formula unit, a gradual phase change from magnetite to maghemite takes place.

Hematite ($\alpha\text{-Fe}_2\text{O}_3$) is a mineral, which was known (up to several years ago) as the worst enemy of car owners. In contrast to maghemite it crystallizes in the corundum-structure. Hematite is antiferromagnetic with a quite high $T_N = 950$ K. An interesting feature is the so-called MORIN-transition at 260 K, where the spin-axis reorients from the low-temperature c-direction by 90° into the (001)-plane. Due to the DZHALOSHINSKY-MORIYA-interaction, the moments become canted in the high-temperature-phase, producing weak ferromagnetism [37, 101].

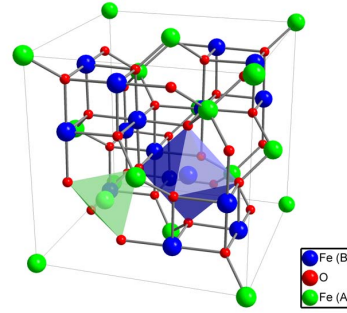


Figure 3.5.: Crystal structure of magnetite.

4. Experimental Methods

4.1. Generation of polarized x-rays – synchrotron radiation

Today, materials science relies to a large extent on the use of x-rays of variable energy and polarization, because of to their versatility in determining chemical and structural order. Without high brilliance x-ray sources such as synchrotrons, the recent advances in this field would not have been possible. In the following, a brief introduction into the generation and use of synchrotron radiation will be given, based on the monographs and reviews in Refs. [10, 151, 29].

In the early days of x-ray physics, scientists had a very hard task in waiting days and weeks for their experiments to be finished. Be it x-ray diffraction, absorption or fluorescence, the sources – conventional x-ray tubes based on the principle detected by WILHELM CONRAD RÖNTGEN – simply did not possess enough flux to allow for convenient measurement times. Admittedly, detectors were not as efficient as today, but still the major drawbacks were intensity – and tunability. For some applications – like spectroscopy – monochromatized x-rays were needed. This was usually achieved by a grating- or crystal monochromator or a filter, cutting the flux further. The way out was offered by a phenomenon, which first occurred as a parasitary effect in big particle storage rings like, for example, DORIS [34]. There, charged particles are accelerated until they almost reach the speed of light, and then fed into a storage ring, conserving their energy by microwave feedback. Keeping them on their orbit requires transversal acceleration by bending magnets and beam-shaping devices (sextupole-, octupole-magnets), intermitted by straight sections where so-called *insertion devices* can be installed (this will be discussed later). As electrodynamics predicts, every charged particle experiencing acceleration emits electromagnetic radiation [46]. Since the emitted power depends on the particle energy as

$$P = \frac{2e^2c}{3R^2} \left(\frac{E}{m_0c^2} \right)^4, \quad (4.1)$$

the effect becomes very pronounced at relativistic energies [10, 29]. Another feature that comes with relativistic motion is, that the "classical" HERTZian dipole

radiation, having a "doughnut"-like characteristics with axis along the propagation direction, is distorted into a narrow cone *along* the propagation direction, with an angle $\theta = 1/2\gamma$, $\gamma = 1/\sqrt{1 - v^2/c^2}$. This means, that synchrotron sources have a very high brilliance. With $\gamma = 1.96 \cdot 10^3 \cdot E_e[\text{GeV}]$, which takes values around $\gamma \approx 3000$ for common synchrotron sources, the full emission angle is as small as 0.1 mrad.

Looking at a charged particle moving on a circular trajectory, it is directly apparent that according to the laws of momentum conservation, the photons emitted must possess a defined angular momentum, since the electron does so, too. In this sense, the synchrotron is like a giant atom. This picture, though a bit unprecise, provides an easy rule of thumb to predict the polarization type depending on the emission direction relative to the orbital plane [151]. Since during emission, the amount $\hbar \text{sgn}(\hat{\mathbf{l}} \cdot \hat{\mathbf{k}})$ of the electron angular momentum is transferred to the photon, one can directly conclude on its helicity. This means that for the common case of electrons circulating clockwise in a synchrotron, photons emitted above the orbit plane are left circularly polarized ($\sigma = -1$) and below right circularly polarized ($\sigma = +1$). Emission exactly within the ring plane consequently leads to horizontal linear polarization. Such polarization characteristics is usually emitted by bending magnets, and as one already can see, the linear vertical polarization component is not accessible.

Applications that need a higher flux and variable polarization require a special type of insertion device, the so-called *undulator*. One of the most versatile designs is the APPLE-II type undulator, which contains four independent magnet arrays [128]. By adjusting the phase relations between the four arrays properly, it is possible to force the electrons passing in between into arbitrary helical or linear sinusoidal trajectories, thus allowing for variable polarization [176]. One of the features important for vectorial magnetometry using XMLD is the free rotation of the linear polarization around the beam axis (see Sec. 7.3.2), which becomes possible with this type of undulator.

4.2. Photoemission microscopy using soft x-rays

In the following, the primary measurement technique and instrumentation used in this thesis, Photoemission Electron Microscopy (PEEM) will be outlined, with regard to the special circumstances when using polarized x-rays for the generation of photoelectrons as compared to excitation by UV radiation or low energy electrons reflected from the sample surface (LEEM). The details given here are based on the review articles in Refs. [12, 130, 131] about electron and photoelectron microscopy.

An early electron microscope based on photoelectrons emitted from the sample itself has been proposed by BRÜCHE in 1934 [19], and worked essentially like an electrostatic loupe with only one (magnetic) lens for focussing and a phosphor screen to transform the electron distribution into visible light. The new concept was that the sample was now itself part of the optical system, emitting the particles to be imaged. Modern versions of the PEEM have a more complex design, partly analogous to an optical microscope:

Photoelectrons are emitted from the sample by a light source of sufficient energy to overcome the sample's work function. They are subsequently accelerated by a so-called electrostatic immersion lens – an analogy to the optical immersion objective, where high numerical apertures are achieved by special tricks, i. e. inserting a material with high refractive index.

The trick with PEEM is to strongly accelerate the electrons by fields of +10 kV/mm on a very short distance (1-2 mm) in order to achieve a high acceptance angle. A second consequence of the high acceleration voltage is to reduce the relative energy spread $\Delta E/E_0$ (polychromaticity) of the electrons, thereby reducing chromatic aberration and increasing the final resolution. In addition, also the angular spread will be narrowed down, leading to a reduction of spherical aberration. The resolution can be further improved by additional optical elements like electron mirrors, energy analyzers or apertures. While mirrors belong to the class of compensation elements, involving no loss of intensity, analyzers and apertures work as filters, reducing the total flux. For simplicity we will only discuss the effect of an aperture here. Placed into a crossover of the electron trajectories, an aperture can be used to diminish the angular distribution of the photoelectrons, caused by their energy spread, and therefore select electrons with a smaller energy bandwidth. This leads to improved resolution at the cost of intensity. Apertures are usually placed in the back focal plane or a suitable image of it, working as an energetic low-pass filter. The typical energy distribution of the photoelectrons is shown in Fig. 4.1 (A). It has a smooth background peaking at low kinetic energies of only a few eV, then decreasing strongly towards higher energies. This background is caused by secondary electrons generated during the photoemission process. The function of the aperture is to cut out all the high-energy electrons, limiting the kinetic energy to a narrow range at low values (B). A typical PEEM optical setup is shown in Fig. 4.2. Besides the immersion lens (extractor),

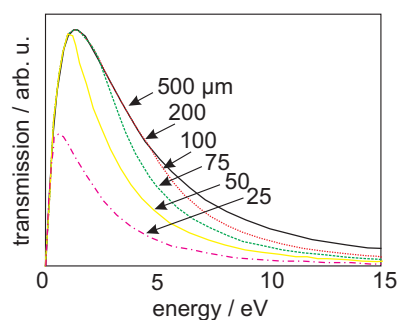


Figure 4.1.: PEEM transmission of secondary electrons excited by synchrotron radiation, measured for various aperture diameters (after [4]).

there are at least two more projector lenses which produce a magnified version of the intermediate image directly on a phosphor screen, or – as in most modern versions – on an image intensifying system, for instance, a multi-channel plate stack with subsequent scintillator. Focal stigmators are included to improve focus quality, removing astigmatism due to any spurious field distributions, which are non-centrosymmetric with respect to the optical axis. Finally, optional deflector units allow for a convenient alignment of all optical elements to a single optical axis. A well aligned microscope can typically reach a resolution down to 20 nm using threshold photoemission by a Hg lamp. In LEEM mode, where strongly reflected low-energy electrons with a small energy spread are used for imaging, an even better resolution down to 10 nm can be obtained. Excitation by x-rays does not directly allow such high resolutions, since the energy-spread of the photoelectrons is considerably larger. Typical values here are (for our experiments) below 70 nm.

Contrast using UV light and x-rays can arise from several effects. (i) Topographic features on the sample surface cause a deflection of the photoelectrons at field inhomogeneities (such as steps), which produce variations in the local photoelectron yield; (ii) material-dependent work functions can lead to laterally varying electron yield in chemically inhomogeneous samples; (iii) using x-rays, chemical sensitivity can be achieved by tuning the photon energy to specific absorption edges. The selected element will then produce a high amount of photoelectrons via primary and secondary photoionization processes.

(iv) Additionally, in a sample with magnetic order, various contrast mechanisms are possible. LORENZ contrast, for example, is caused by a deflection of the photoelectrons in inhomogeneous surface stray field patterns of a ferromagnetic domain structure. This contrast requires no special illumination technique, unpolarized UV light is sufficient. Using polarized or even unpolarized UV light, magnetic contrast can also be achieved by the MLDAD effect. One of several possible contrast mechanisms is, for example, that the electron yield is influenced by the magnetization component transversal to the plane defined by the light incidence direction and the PEEM optical axis. Field reversal along this direction changes the angular distribution of the photoelectrons excited by p-polarized photons, which is then transformed into an intensity variation by the acceptance angle cutoff in the PEEM (see,

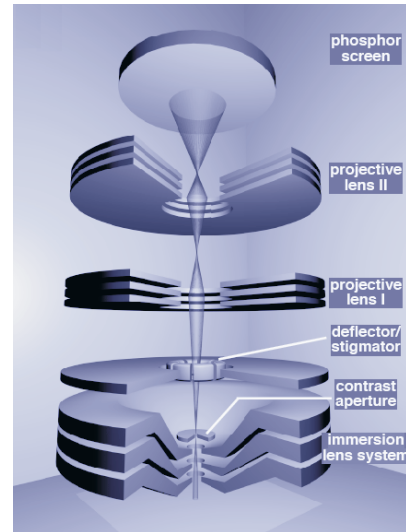


Figure 4.2.: PEEM optics (after Ref. [131]).

for example, Ref. [94]). Finally, we come to the most important and versatile type of contrast, which is produced by Circular and Linear Dichroism (XMCD, XMLD). Tuning the x-ray energy while recording image sequences, microspectroscopy can be performed in so-called Total Electron Yield (TEY), or better: Partial Yield (PY), since the electrons are low-pass filtered. Magnetic dichroism will then manifest in a local variation of the electron yield depending on the local magnetic order. In this way, ferromagnetic as well as antiferromagnetic domain states can be imaged by XMCD resp. XMLD. The usual procedure to enhance magnetic contrast and remove inhomogeneous image backgrounds is to compute ratio-images (I_1/I_2) or asymmetry-images $(I_1 - I_2)/(I_1 + I_2)$ of measurements at two different helicities (XMCD) or x-ray energies/polarizations (XMLD). In this way, any effects caused by inhomogeneous illumination of the sample or the detector sensitivity pattern are eliminated, provided that the illumination is stable between two images.

5. Magnetic Proximity Effect and Related Phenomena

When two different magnetic materials are brought into contact, their magnetic structure may be altered near the interface. This effect is generally referred to as "magnetic proximity effect" [72]. There are various reasons for this alteration:

1. *exchange interaction across the interface*
2. broken translational symmetry normal to the interface, which has several consequences: (i) Additional electronic *interface states/bands*, which do not exist in the bulk, in analogy to surface states (see, for example, Refs. [86, 70]). (ii) Altered *bonding anisotropies* and *anisotropic exchange interaction* at the interface, which modify the orientation and sizes of spin- and orbital momenta (for example [170]). (iii) additional magnetic interactions like the DZHALOSHINSKY-MORIYA interaction, which is related to broken translational symmetry or the absence of a crystalline inversion center [37, 101].
3. interfacial reconstruction, i. e. a *per se* different geometric and hence also electronic and magnetic structure *within* each constituent material near the interface (for example [70]).
4. hybridization effects between different species across the interface, which do not occur inside the bulk (i.e. in [119, 155]).
5. Magnetoelastic interaction between the two materials arising from both epitaxial lattice strain and magnetostrictive effects (this aspect will be discussed in more detail in Chap. 7).

5.1. Interfacial exchange coupling and exchange bias

Almost exactly 50 years ago, MEIKLEJOHN and BEAN made a discovery, which should prove 30 years later as invaluable for spintronics and magnetic storage technology. In a very simple system, namely cobalt nanoparticles with a surface shell oxidized to CoO in air, they found a peculiar and "new anisotropy" (such was the title of their work). By hysteresis and torque measurements they found that the magnetization loop of field-cooled particles, i.e. samples which had been cooled through the Néel temperature of CoO in an external magnetic field, exhibited a characteristic shift on the field axis as compared to the high temperature state. The second peculiarity was the torque curve,

$$T = -\frac{\partial E}{\partial \theta} = -K_u \sin(\theta) \quad , \quad (5.1)$$

where E is the energy and θ is the angle between the cooling field direction and the magnetization. This torque did not resemble the shape for a free ferromagnetic particle

$$T = -\frac{\partial E}{\partial \theta} = -K_1 \sin(2\theta) \quad , \quad (5.2)$$

and integrating the torque curves, it directly became apparent that a unidirectional anisotropy $-K_u \cos(\theta)$ emerged, besides the uniaxial anisotropy $K_1 \sin^2(\theta)$ of the Co particles in the field-cooled case. This anisotropy tended to pin the particle magnetization along the cooling field direction, leading to a shift (*bias*) of the hysteresis loop towards the *negative* field axis. MEIKLEJOHN and BEAN concluded that the most probable origin was a spin-effect between the Cobalt and its oxide and termed the phenomenon *exchange anisotropy* and the loop shift *exchange bias*. Without this "magnetic glue" it would have been incomparably more difficult to construct GMR sensors with sufficient stability of the magnetic reference layer.

5.1.1. Models and their limits

Coherent rotation model by Meiklejohn and Bean

To explain their results, MEIKLEJOHN and BEAN invoked a model, where a uniaxial ferromagnet was coupled to an ideal layered and uniaxial antiferromagnet (see Fig. 5.1 (B)). The interface was assumed completely *uncompensated*, i.e. all AF interface spins belong to the same antiferromagnetic sheet. Furthermore, the AF was assumed completely "rigid", i.e. its anisotropy was set to infinity,

confining the moments within the sample plane along the easy axis. The strictly simplifying assumptions were appropriate to explain the basic features of the phenomenon, i.e. the loop shift and torque behaviour, but failed in estimating the size of the exchange field. Naively assuming a difference between high- and low energy state

$$\sigma_{\text{int.}} = E_{\uparrow\downarrow} - E_{\uparrow\uparrow} = \frac{2J_{\text{int.}}S^2}{a^2}$$

or in terms of the bias field

$$H_{eb} = \sigma_{\text{int.}}/(M_{\text{F}}t_{\text{F}}) = \frac{2J_{\text{int.}}S^2}{a^2M_{\text{F}}t_{\text{F}}}$$

yields values about three orders of magnitude too high (for instance $\approx 17 \text{ Jm}^{-2}$ for a Co surface [152]) as compared to the experimental findings ($\approx 10^{-2} \text{ Jm}^{-2}$ [107]).

Approaching reality...

Subsequently, several approaches have been pursued to better meet the experimental reality. The main improvements to name here were (i) a more physical picture of both the AF and the FM with variable anisotropies and planar domain walls, (ii) the account for interface roughness, (iii) the inclusion of higher-order magnetic interaction such as biquadratic exchange. Further improvements were the account for systems with variable defect densities (diluted ferromagnets and antiferromagnets, DAFF) and a more realistic domain-state in both the FM and the AF.

Planar domain walls

One of the first "remedies" found to get rid of unrealistically high exchange anisotropies was the assumption of a less rigid antiferromagnet. MAURI *et al.* developed a model,[96] which contains a coupling parameter, defined as the ratio between the interfacial coupling energy density $\sigma_{\text{int.}}$ and the domain wall energy of a NÉEL-type partial domain wall in the antiferromagnet

$$\lambda = \frac{A_{\text{int.}}/\xi}{2\sqrt{A_{\text{AF}}K_{\text{AF}}}} \quad , \quad (5.3)$$

where $A_{\text{int.}}$ is the interfacial exchange stiffness $J_{\text{int.}}/a$, and ξ is the spacing between FM and AF, i.e. at least one atomic distance a . In the limit of weak coupling ($\lambda \ll 1$), the results of MEIKLEJOHN and BEAN are restored, and the AF spins keep their direction, the bias field becoming $H_{eb} = -A_{\text{int.}}/(\xi M_{\text{F}}t_{\text{F}}) = -J_{\text{int.}}/(a^2 M_{\text{F}}t_{\text{F}})$.

For strong coupling $\lambda \gg 1$, a partial domain wall (*exchange-spring*) forms in the antiferromagnet, with typical energy $2\sqrt{A_{\text{AF}}K_{\text{AF}}}$. In this case, the exchange field becomes

$$H_{eb} = 2 \frac{\sqrt{A_{\text{AF}}K_{\text{AF}}}}{M_{\text{F}}t_{\text{F}}} . \quad (5.4)$$

Such exchange-springs really exist in the non-ground state of the system, i.e. with the FM not pointing along its easy direction, as has been shown experimentally, for example, in Refs. [175, 132, 125]. The width of the planar domain wall forming in the strong coupling case can be large, in the order of more than 100 nm, as has been shown experimentally in Ref. [175], where a spin-spiral has been identified by AF thickness variation of NiFe/FeMn/Co trilayers. The ground state proximity zone will – in general – be much narrower, as will be discussed in the following sections and the experimental part of this thesis. An important improvement of the partial-domain-wall model is that the disappearance of the exchange bias for AF thicknesses lower than the critical domain wall width $\pi\sqrt{A_{\text{AF}}K_{\text{AF}}}$ is predicted correctly.

Random fields

Thirty years later the discovery of exchange bias, MALOZEMOFF introduced a model accounting for surface roughness, which lead to realistic values for H_{eb} [92]. He assumed a randomly rough boundary between the ferromagnet and the antiferromagnet, which introduces statistical variations in the magnetic order at the interface. For an uncompensated interface like in Fig. 5.1 (B), it is directly apparent that any roughness will decrease the magnitude of the exchange anisotropy, since spins of the unfavourable AF sublattice meet the interface, leading to an increased amount of spin frustration. For a compensated interface, defects can lead to a locally enhanced or reduced exchange energy, i.e. the interface becomes *locally uncompensated*, with a *random field* pointing along the local excess-spin direction. This random field will then introduce a domain state in the antiferromagnet in such a way as to minimize the interfacial spin frustration by introducing antiphase domains (see Fig. 5.1(G-H)). The typical length scale was assumed to be similar to ferromagnetic domain-wall widths, i.e. $L \approx \pi\sqrt{A_{\text{AF}}K_{\text{AF}}}$, where $A_{\text{AF}} = J_{\text{AF}}/a_{\text{latt}}$ is the *exchange stiffness* and K_{AF} is the antiferromagnetic volume anisotropy. If in an area of L^2 around the defect a reorientation of the antiferromagnet occurs, one can expect that the amount of spin frustration and thus the energy is reduced by a factor of $\frac{1}{\sqrt{N}}$, where $N = L^2/a^2$ is the number of lattice sites in the area.

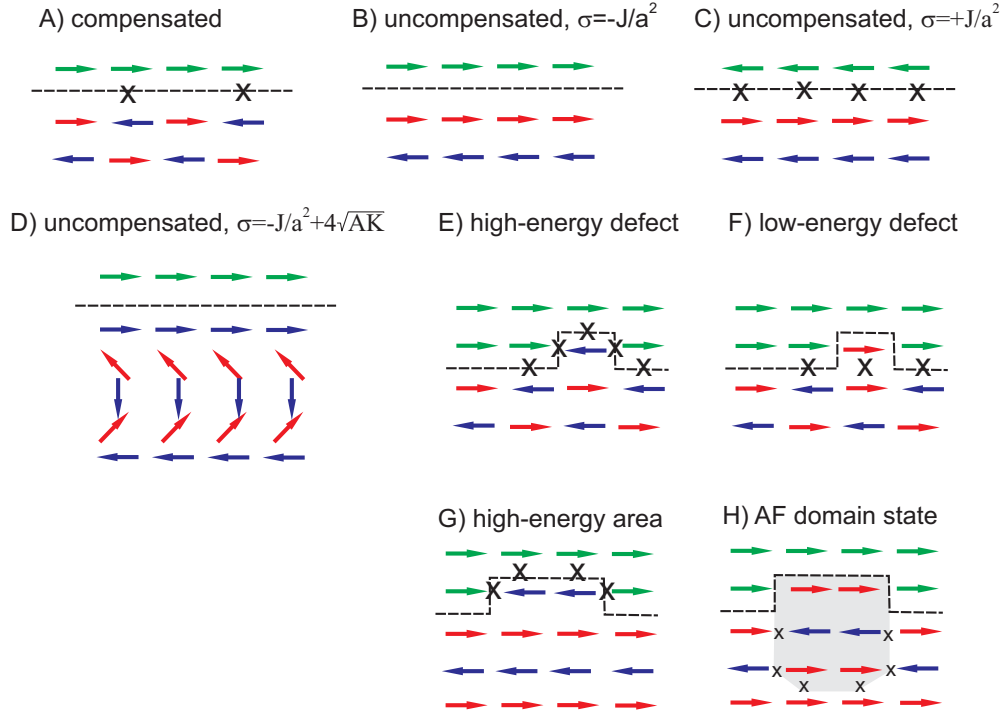


Figure 5.1.: Various scenarios at the FM/AF interface: (A) at a fully compensated interface, collinear alignment leads to 50% spin frustration; (B) energetically favoured configuration at an uncompensated interface; (C) if the FM is reversed, the energy increases by $2J/a^2$; (D) The AF can respond by formation of a planar domain wall, lowering the energy again by $2J/a^2$, but at the cost of domain wall energy $4\sqrt{AK}$; (E) some AF defect spins have a high energy configuration and can reverse parallel to the FM (F) producing an uncompensated magnetization in the AF. (G) local fields acting on the AF can lead to confined regions of high interface-exchange energy; (H) Those can be removed by formation of antiphase domains inside the AF, especially in case of strong interface coupling and low AF anisotropy.

Spin-flop coupling: Necessary preconditions and relation to exchange bias

In analogy to investigations of HINCHEY and MILLS [63] for superlattices, KOON developed a theory for the interesting case of a perfectly compensated interface. The motivation for his work was the finding of a perpendicular alignment of the FM and AF easy axes in NiFe/FeMn [69] and a large exchange bias for a compensated interface of 0.11 Jm^{-2} in FeF_2/Fe [108]. At the same time, perpendicular coupling was also detected for the FeF_2/Fe system, both for the compensated (110) and the *uncompensated* (001) interfaces [100]. In this work it was already pointed out that spin-flop coupling at an uncompensated interface is unusual and interactions other than exchange might be at work. The conclusion at hand was that magnetoelasticity might play a role in the systems tendency for collinear respective perpendicular alignment.

Irrespective of the mysteries in this effect, KOON modeled a (110) oriented bcc system very similar to FeF_2/Fe , assuming a *constrained in-plane* anisotropy and a perfectly compensated interface with strong exchange coupling. The mean-field numerical calculations indeed revealed a 90° orientation of the FM with respect to the AF, with both the FM and the AF-spins canted by a small angle out of their purely perpendicular alignment. The canting angle was found to diminish as a function of distance from the interface, and was reduced to zero within only 5-6 monolayers. This means, that the proximity zone turned out to be ultrathin in this model, a direct consequence of the restriction to only nearest neighbour exchange interactions. For fluorides and oxides, in which exchange and conduction usually is mediated via short-ranged hopping mechanisms, this is indeed a good approximation. We will discuss this aspect later in more detail when presenting the experimental details. Interestingly, the reduction of the overall interfacial exchange energy by spin-flopping as compared to a fully uncompensated interface with collinear coupling was only 6%, and thus much smaller than expected.

To test the system for exchange bias, the FM was simplified as a macrospin, i. e. a layer with homogeneous spin orientation under neglect of canting. Then, the energy minimum was calculated for different *in-plane* angles θ with respect to the easy direction. The consequence was a formation of a partial domain wall in the antiferromagnet (so-called exchange-spring), and the typical characteristics of the energy curves contained an "unwinding" instability for angles greater than a certain threshold, where the antiferromagnet flipped back to a lower energy branch. The instability angle increased rapidly with increasing AF thickness, approaching 180° for $t_{\text{AF}} > 50 \text{ ML}$. This means that for thicker AF layers the energy curves are completely reversible for simple switching of the FM, i.e. *exchange bias* occurs.

The artificial in-plane constraint of the model was later discovered to overestimate the tendency for exchange bias with spin-flop coupling. It was found, for example, by SCHULTHESS and BUTLER,[134] that a so-called transversal instability in the AF can always occur (which is different from the "unwinding" instability in KOON's model). If the FM direction is reversed by an external field, the canted AF spins can always change into the low energy mirror-symmetric configuration making a movement similar to the paddles of a rowing boat (see Fig. 5.2). By this effect, exchange bias should be impossible in single-domain spin-flop systems. Consequently, Schulthess and Butler had to introduce uncompensated defect spins to re-establish a finite exchange bias. Interestingly, FINAZZI found in calculations on the Fe(001)/NiO system that defects are not only related to the occurrence of exchange bias, but can also decide whether a spin-flop or a collinear state develops in the system [42].

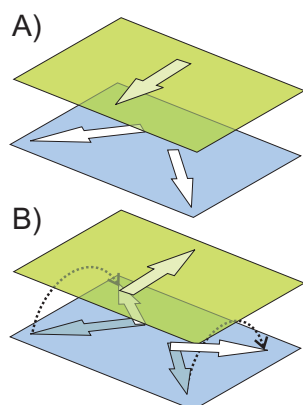


Figure 5.2.: Transversal instability during field reversal of a spin-flop coupled system.

USOV *et al.* resolved the issue of missing exchange bias in calculations of spin-flop systems by allowing a domain state in the antiferromagnet, where several AF easy axes in different domains coexist. In this way, exchange bias, which was nonexistent in the single domain state, could be re-established for sufficiently strong interface coupling [157]. Experimentally, FITZSIMMONS *et al.* investigated the relation between the occurrence of exchange bias and spin-flop coupling for different crystalline structures of the antiferromagnet in poly-Fe/MnF₂ and poly-Fe/FeF₂ systems [45]. For untwinned single crystalline AF substrates, they found considerable exchange bias by field cooling parallel to the AF easy axis, while field cooling perpendicular to the AF easy axis produced a pure spin-flop state and no exchange bias. In twinned and textured AF layers, however, always a unidirectional anisotropy was found. They concluded that (i) spin-flop coupling is neither a required nor a necessary condition for exchange bias, however, (ii) frustrated spin-flop coupling in a twinned or multidomain AF can lead to considerable bias. In this sense, their findings comply to the theory of USOV *et al.*.

Noncollinear exchange bias and training effects

In all the model mentioned above (except the one by USOV) it was assumed that both the FM and the AF anisotropies are uniaxial, with the easy axes being

collinear. This situation is generally not realistic. A generalized MEIKLEJOHN-BEAN approach by BINEK *et al.* [14], for example, accounts for a possible angle between the two easy axes, and calculations by HOFFMANN [64] consider multiple easy axes inside the AF, identifying metastable non-collinear magnetism at the F/AF interface as the origin of training effects. The non-collinearities are then successively removed by repeated field cycling, thereby altering the magnetic structure at the interface. Consequently, exchange bias, coercivity and the shape of the hysteresis curve change in subsequent field cycles until stability is achieved. The hypothesis that a multi-axis antiferromagnet may be responsible for training effects is – according to Ref. [64] – supported by the fact that training effects were not observed for uniaxial F/AF systems, like untwinned $\text{FeF}_2/\text{poly-Fe}$ and $\text{MnF}_2/\text{poly-Fe}$ [45].

Microscopic details of the proximity zone

Up to now we have assumed that the materials in contact possess their bulk magnetic and crystalline structure at the interface, which means that, for instance, the antiferromagnet can have a multidomain state, but all the domains exhibit the bulk antiferromagnetic order right up to the interface. Any uncompensated magnetization is either caused by defects, a random-field driven redistribution of bulk AF domains with net spin-polarization at the interface or spin-canting of a spin-flop state. Due to the proximity effects mentioned at the beginning of this chapter, however, it is also likely that the interfacial region possesses completely new properties different from the bulk, for example, a different *intrinsic* AF order. This could mean that totally different stacking vectors and types of AF structure may exist, and a transition to the bulk structure must somehow be achieved in the vicinity of the interface. Calculations of JENSEN *et al.* [68] and FINAZZI [42] indicate that due to the boundary conditions at the interface, a secondary magnetic order is superimposed onto the bulk order of the antiferromagnet near the interface. An interesting feature of this superposition is that the uncompensated magnetization *per layer* can change its sign with respect to the direction of the FM magnetization. The behaviour resembles a strongly damped oscillation of the uncompensated moment as a function of distance from the interface. This oscillation is mediated via the 180° superexchange interaction, which favours antiparallel spin alignment between nearest neighbours. De facto, one could speak of a second type of AF order which coexists with the bulk AF order near the interface. This interesting aspect was part of the motivation for the measurements of the interfacial magnetic structure in $\text{Fe}_3\text{O}_4(110)/\text{NiO}$ presented in Chap. 6.

Magnetoelastic coupling

A detail generally neglected in exchange bias theory is the magnetoelastic coupling between the two magnetic layers in contact. Two major effects of magnetoelasticity have to be distinguished in this context: (a) the epitaxial lattice strain, which is introduced in both materials in case of a lattice misfit. This strain can lead to a zone of altered magnetization via magnetoelastic interactions, until finally strain relaxation occurs via dislocation defects, or it can affect the whole layer in case of unrelaxed growth. (b) Magnetostriction and exchange-striction lead to crystal distortions dependent on the spin orientation in the two materials. At the interface, the strictions of both materials can be compatible (low-energy state) or incompatible (high-energy state). Depending on what spin-directions are preferred for compatible strain in both materials, magnetoelasticity can support or counteract the spin-configuration favoured by interfacial exchange interaction. As mentioned earlier, a first speculation towards this direction has been made in Ref. [100], but up to now more detailed investigations are rare¹.

In contrast, there exist several studies about the influence of epitaxial strain on the magnetic structure of antiferromagnets, for example Refs. [60, 31]. The usual stray field arguments valid for ferromagnets do not apply to compensated antiferromagnets, when trying to find out if the anisotropy is *in-plane* or *out-of-plane*. There is, however, some kind of shape-anisotropy inside these layers, which can have two different origins. One origin is a pseudodipolar anisotropy analogous to ferromagnets, as for example postulated by FINAZZI. An alternative explanation by GOMONAY and LOKTEV assumes a shape anisotropy by magnetoelastic surface strains [52].

An important fact that should be mentioned here is that in the absence of complete relaxation the magnetoelastic interactions and strains are generally long-ranged, over dimensions of hundreds of lattice constants, while the exchange effects are generally very short-ranged. This may have interesting consequences on the thickness-dependence of the proximity effect respective exchange bias.

The question whether there is an interplay between exchange coupling and magnetoelasticity will be addressed in Chap. 7, where different interface orientations are compared with respect to the magnetic structure that develops at the interface.

¹In fact, the author did not find a single one

Part II.

Experimental results

6. Proximity effect in Fe_3O_4 (110)/NiO

6.1. Introduction

In this chapter, the alteration of the interfacial magnetic structure in the oxidic heterosystem $\text{Fe}_3\text{O}_4/\text{NiO}$ will be discussed in detail. As an example, the (110) orientation is considered, since the proximity effect manifests here more drastically than in other crystalline interface orientations. We will employ all available contrast mechanisms to provide an almost complete picture of the material-specific magnetism. Circular dichroism provides information about the substrate net magnetization (Fe-edges) and the uncompensated magnetization in the NiO layer (Ni-edges). The influence of natural linear dichroism will be discussed in terms of epitaxial lattice strain, and temperature-dependent measurements will be presented to identify the magnetic contributions to the contrast and to reveal finite size effects in the sample. Magnetic linear dichroism at the Ni L_2 edge provides information on the spin-axis orientation in NiO. Finally, by thickness dependent measurements on a NiO wedge, the development of the interfacial magnetic structure will be monitored, permitting depth-dependent analysis.

6.2. Sample preparation

A synthetic single crystal of magnetite (Fe_3O_4), oriented and polished to yield a (110)-surface served as substrate. To obtain a stoichiometric and well-ordered magnetite template, substrates were prepared as described by JANSEN *et al.* [67]. Surface conditioning consisted of several cycles of sputtering with 1 keV Ar-ions and subsequent annealing in 10^{-6} mbar O_2 pressure at 1100 K. It is interesting to note, that JANSEN *et al.* report a one-dimensional reconstruction of the sample surface, with lines of 1-2 ML height and a spacing of 3-4 times the lattice constant (8.396 Å) running along $[\underline{1}10]$. According to this study, the lines are B-terminated (only octahedral cation sites) and the grooves are A-terminated, i.e. both octahedral (B) and tetrahedral (A) sites are present.

To check the surface phase in our sample, it was transferred *in-situ* to the microscope chamber in order to record local XAS and XMCD spectra. Information about sample stoichiometry can be gained by fitting the sum of the site- and valency-dependent contributions to the XMCD as obtained by atomic multiplet calculations. The method is described, for example, in ref. [129]. For stoichiometric magnetite the ratio of $Fe_{tet}^{3+}:Fe_{oct}^{3+}:Fe_{oct}^{2+}$ should be 1:1:1. Since no atomic multiplet calculations were at hand, data were taken from Ref. [129] by digitizing the graphs. The analysis was restricted to the L_3 region, since the accordance of theory and experimental spectra is usually best in this region. As can be seen in Fig. 6.1, there are considerable differences between the calculations and the experimental data outside that region. It has to be pointed out that the accuracy of this method depends on the quality of the theoretical calculations as well as on the structural model assumed for the non-stoichiometric magnetite. The contribution of those aspects to the overall uncertainty can only be estimated, and the results gained by this analysis should therefore be interpreted with care. The relative error in the determination of stoichiometry might thus be as high as $\pm 20\%$. Nevertheless, the method provided the only accessible way to perform a comparative analysis of the sample surface composition, since no additional *in-situ* techniques like AUGER- or photoemission spectroscopy were available.

The sample was only slightly non-stoichiometric according to this analysis, corresponding to $Fe_{3-\delta}O_4$, $\delta = 0.032$ (see Fig. 6.1). After this analysis, NiO was deposited onto the sample by MBE at room temperature in an oxygen background pressure of 10^{-6} mbar. The molecular beam was directed onto the sample under normal incidence, in order to avoid deposition-induced contributions to the magnetic anisotropy. As described later, the experiment was repeated several times, each time with a removal of the NiO layer by Ar-sputtering and re-preparation of the substrate surface. Complete removal of the NiO was also checked by XAS. To "freeze" a domain state into the antiferromagnet, the sample was heated for several minutes to 573 K – high enough to exceed the bulk NiO NÉEL temperature of 523 K [95] and low enough to prevent thermal intermixing at the interface [121]. Cooling down slowly without application of an external field resulted in large homogeneous domains in both materials. As will be shown in Sec. 6.3.4, the interface resulting from the overall preparation procedure is indeed atomically sharp.

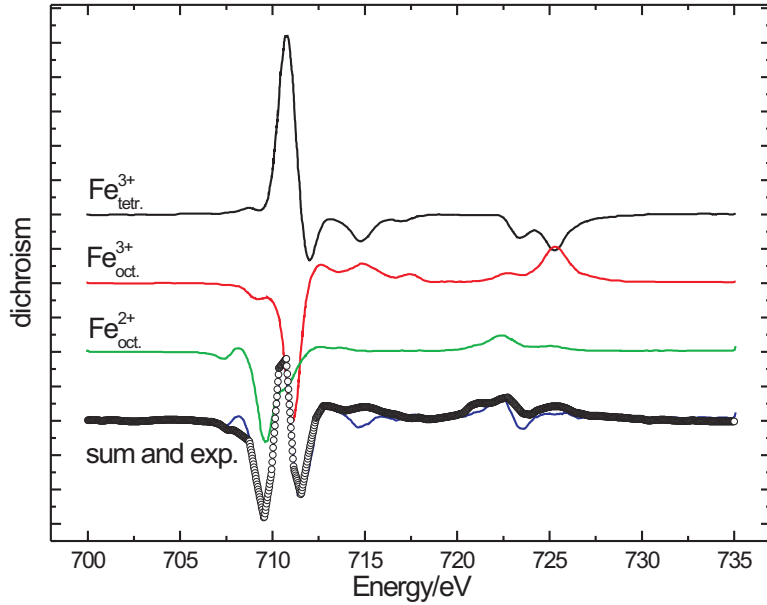


Figure 6.1.: Comparison of the experimental Fe₃O₄-XMCD to atomic multiplet calculations (taken from ref. [129]). Ideal Fe₃O₄ has the structure Fe_{T_d}³⁺Fe_{O_h}³⁺Fe_{O_h}²⁺O₄. Non-stoichiometric magnetite corresponds to Fe_{T_d(1-γ)}³⁺Fe_{O_h(1+2δ+γ)}³⁺Fe_{O_h(1-3δ)}²⁺O₄, where δ is the amount of octahedral vacancies and γ is the transfer of Fe³⁺ ions from tetrahedral to octahedral sites. The sum of three site-valency spectra fitted to the experimental data (circles) is shown at the bottom. According to the fit, the sample is slightly non-stoichiometric with δ = 0.032.

6.3. Vectorial magnetometry using PEEM microspectroscopy

In the following section the local magnetic structure of the sample constituents will be extracted from the spatially resolved soft x-ray microspectra measured with PEEM. To discriminate between interfacial and bulk magnetic structure of the antiferromagnetic layer, different film thicknesses/coverages have been prepared, namely, a fractional NiO coverage corresponding 0.5 ML thickness, a thick 35 ML film (51 Å) and a stepped wedge with step heights of 2.5 Å. A 0.5 ML partial coverage of NiO will exhibit no antiferromagnetic order, but rather consist of islands coupled parallel to the substrate net magnetization. It can thus provide information on the magnitude and signature of the Ni-XMCD upon complete alignment of the Ni-spins. The thicker 35 ML film shows antiferromagnetic order and serves as a reference to extract the total amount of spin-polarization induced

by the exchange coupling. At last, the wedge sample provides detailed information about the development of the interfacial magnetic structure depending on the layer thickness. From the growth process, conclusions about the depth-dependent magnetic structure can be made.

6.3.1. Determination of the substrate magnetization map

To extract information about the magnetic coupling between FIM and AF, first the local magnetization directions in the substrate must be known. This can be achieved by using the $\cos \angle(\mathbf{k}, \mathbf{M})$ -dependence of the XMCD magnitude, where \mathbf{k} is the photon wavevector and \mathbf{M} the local magnetization direction. In principle, measurements along three linearly-independent directions are necessary to extract the vector orientation. This was, however, not possible due to the fixed measurement geometry. In order to be able to perform a reliable analysis in spite of the fixed experimental geometry, additional information has to be provided and the conditions for the applicability of the angular relation mentioned above have to be checked.

Eq. 1.16 is not generally applicable because of the magnetic dipole operator \mathbf{T} arising from a quadrupole moment in the spin density distribution [150]. Though \mathbf{T} vanishes in the bulk of our samples due to cubic symmetry, at surfaces/interfaces, a nonzero contribution may occur. In the case of the $\text{Fe}_3\text{O}_4/\text{NiO}$ interface, the effect of \mathbf{T} on magnetization mapping by XMCD-PEEM is small for two reasons: (i) The oxygen sublattice is continuous across the interface, providing a bulk-like environment for the B-site cations. Since – as we will see later, Ni^{2+} favours octahedral sites, no magnetic dipole contribution will arise for the Ni-XMCD. (ii) In case of a bulk-like interface termination of Fe_3O_4 , the tetrahedral A-sites within the interface unit cell will add up to cubic symmetry, too. Thus, the interfacial magnetic dipole contribution to the XMCD should be negligible. At the magnetite (110)-*surface*, in principle the situation should be more complicated due to incomplete oxygen coordination of the cations and reconstruction. However, as we will see later, the XMCD analysis without consideration of the magnetic dipole term results in a magnetization map consistent with the expected easy directions.

Having ruled out spurious effects by the magnetic dipole term, we can proceed our XMCD analysis. Fortunately, the drawback of fixed measurement geometry can be overcome by providing additional information about the magnetization orientation: Due to the demagnetizing field at the surface (shape anisotropy), the magnetization is in-plane, and besides this, two easy directions of $\langle 111 \rangle$ -type lie in the Fe_3O_4 (110) surface. Hence, an *in-plane* magnetization is a reasonable assumption, making a measurement of the normal component obsolete. Another helpful

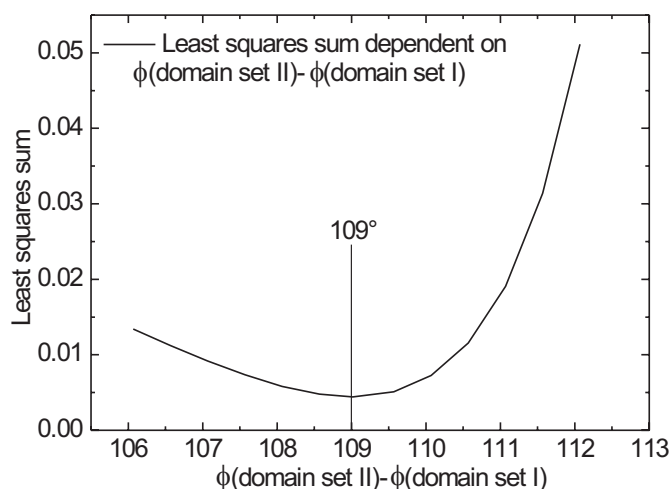


Figure 6.2.: Least-squares sum versus angle-difference between magnetizations in the two domain-sets *I* and *II*. The fit minimum is close to twice the "magic" angle 54.7° , which means that in both sets the magnetization points along $\langle 111 \rangle$ -type directions.

feature are the traces of the closure-domain walls, which run along crystalline high-symmetry directions $\langle \underline{111} \rangle, \langle \underline{110} \rangle$ and $\langle 001 \rangle$. Two sets of domains exist: *Set I* with directions $[\underline{111}]$ and $[\underline{111}]$ and *set II* with directions $[111]$ and $[\underline{111}]$. This corresponds well to the four gray levels seen in the PEEM image of Fig. 6.3.1. The brightest and darkest value corresponds to *set I*, while the intermediate gray levels correspond to *set II*, where the magnetization is almost perpendicular to the light incidence direction. Furthermore, a comparison of the domain wall traces to crystallographic directions obtained from a LAUE-orientation of the crystal yielded very good agreement with the directions assigned above.

The correct magnetization directions can be verified by comparing the magnitude of the XMCD-contrast in different domains. For this purpose, a $\langle \underline{111} \rangle$ -type orientation was simply assumed for $\mathbf{M}(\textit{set I})$, while the XMCD spectrum of *set II* was scaled and fitted to the contrast of the first one, using the magnetization direction $\mathbf{M}(\textit{set II})$ as a free parameter. For the fitting process, only the L_3 -structure of the spectra was taken into account, since this region is well above the noise level in both domain sets. As can be seen in Fig. 6.2, the fit converged for $\mathbf{M}(\textit{set II})$ also pointing along a $\langle \underline{111} \rangle$ -type direction (error approximately $\pm 1^\circ$). The resulting angle agrees well with the theoretical expected angle of 109.47° (twice the "magic" angle). Furthermore, this good accordance allows the important conclu-

sion, that the magnetic dipole contribution to the XMCD is negligible, and the use of Eq. 1.16 for vectorial magnetometry is justified. We speculate, that in contrast to the (110) orientation, for other interfaces like (111) and (001), the accuracy is even better due to the higher *in-plane* symmetry.

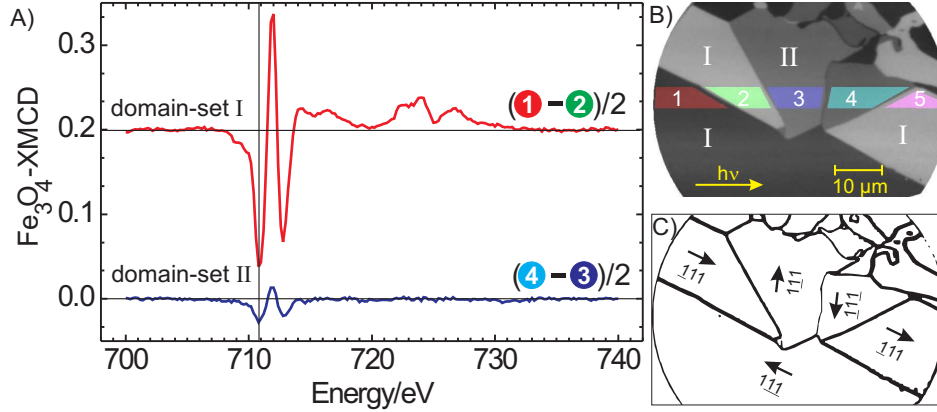


Figure 6.3.: (A) Fe_3O_4 -XMCD microspectra derived from the regions of interest (ROIs) shown in the PEEM image. The y-scale shows the magnitude of the XMCD signal normalized to the peak height of the isotropic L_3 white line. To enhance the signal-to-noise ratio of the XMCD, not a single ROI was used for generation of the XMCD spectrum, but the difference of XMCD spectra from two antiparallel domains was calculated by the rule $\text{XMCD}_{\text{enh.}} = (\text{XMCD}_{\text{ROI1}} - \text{XMCD}_{\text{ROI2}})/2$. The vertical line in the plot indicates the energy chosen for calculation of the XMCD ratio image. (B) Fe_3O_4 : XMCD ratio image σ^+/σ^- . The numbers represent regions of interest (ROIs) for the spectra.

6.3.2. Coupling of the interfacial Ni-moments to Fe_3O_4

While bulk NiO is antiferromagnetic and produces no circular dichroism due to the vanishing net moment, this is not necessarily true for the $\text{Fe}_3\text{O}_4/\text{NiO}$ interface. There, a net Ni magnetization can exist, due to the influence of the interfacial exchange interaction, or if there is a gradual phase transition from ferrimagnetic Fe_3O_4 via NiFe_2O_4 to fully compensated NiO at the interface. Fig. 6.4 (B) shows a PEEM image of the Ni-XMCD contrast calculated as the ratio of two images with different helicity. It is directly apparent, that the pattern in Ni-XMCD

contrast is a perfect replica of the domain structure seen in magnetite substrate. The corresponding nickel dichroism spectra are shown in Fig. 6.4 (A) for both the 0.5 ML coverage and the 35 ML film. The fractional coverage layer exhibits a maximum dichroic signal amounting to 54 % of the isotropic L_3 white-line peak height. The spectral signature closely resembles the data of VAN DER LAAN *et al.* for NiFe_2O_4 [160] with a maximum signal of 53 %, as indicated by the solid line in Fig. 6.4 (A).

The good accordance of the experimental data with the atomic multiplet calculations shows that the Ni^{2+} cations strongly prefer sites with octahedral oxygen coordination, and that no metallic Ni is present at the interface. Note, that the spectral XMCD signatures of metallic and oxidic Ni differ considerably [27]. At the L_3 edge, the XMCD signal of octahedrally coordinated Ni exhibits a pronounced positive spin-flip peak located 2 eV above the energy for the main negative XMCD peak [160]. This peak arises from the large spin-orbit coupling of the core-hole and strong correlation effects due to oxidation, causing a large core-valence exchange-splitting of $\Delta_{pd} = 2$ eV. For metals, Δ_{pd} is much smaller, hence the spin-flip peak is not observable in the XMCD spectrum of metallic Ni. Consequently, the existence of this peak and its good accordance with the data of NiFe_2O_4 show, that the amount of metallic Ni is negligible.

From the sign of the XMCD at the Ni edges, one can further conclude that the induced magnetization is *parallel* to the net moment in Fe_3O_4 , since the main L_3 peak for Ni is negative, just as the two peaks ascribed to octahedral Fe cations in the magnetite XMCD (remind that the octahedral Fe sites determine the net magnetization direction and compare Figs. 6.1 and 6.3.1). If the interface layer reconstructs to NiFe_2O_4 , then the interfacial monolayer contains an ordered arrangement of octahedral Ni cation sites and octahedral vacancies as shown in Fig. 6.7. Since Ni cations favour octahedral sites, they are always connected to tetrahedral ("A") sites via antiferromagnetic 124° superexchange bonds, while the connection to the octahedral ("B") sites is mediated by 90° double-exchange, which is ferromagnetic. Thus, the overall coupling to the net moment in Fe_3O_4 , which is determined by the B site spins, is *parallel*. Looking at the dichroism of the 35 ML film in Fig. 6.4 (A), a reduction of the maximum dichroic contrast to 2.7 % is observed. From the comparison of the dichroism magnitude in both films we can roughly estimate the fraction of the thick NiO layer exhibiting an uncompensated magnetization. First, the magnitude of the unnormalized XMCD in a completely ferromagnetic film scales linearly with thickness d :

$$A_{\text{XMCD}} = N \cdot \mu_{\text{tot.}} \cdot d \quad . \quad (6.1)$$

Second, the isotropic white line intensity for a general film scales linearly with d :

$$I_0 = C \cdot d \quad (6.2)$$

What is known from experiment are the two film thicknesses d_{thin} and d_{thick} and the XMCD spectra normalized to the isotropic white line intensity:

$$a_{\text{thin}} = \frac{N \cdot \mu_{\text{tot.}} \cdot d_{\text{thin}}}{C \cdot d_{\text{thin}}} \quad (6.3)$$

$$a_{\text{thick}} = \frac{N \cdot \mu_{\text{tot.}} \cdot d_{\text{prox.}}}{C \cdot d_{\text{thick}}} \quad (6.4)$$

From this, we can estimate the thickness of the proximity zone $d_{\text{prox.}}$, assuming an abrupt transition to the compensated AF structure for simplicity:

$$d_{\text{prox.}} = d_{\text{thick}} \frac{a_{\text{thick}}}{a_{\text{thin}}} . \quad (6.5)$$

This calculation results in a thickness of about 1.7 ML (2.6 \AA) – a very small value that indicates not only an ultrathin proximity zone, but also a very sharp interface.

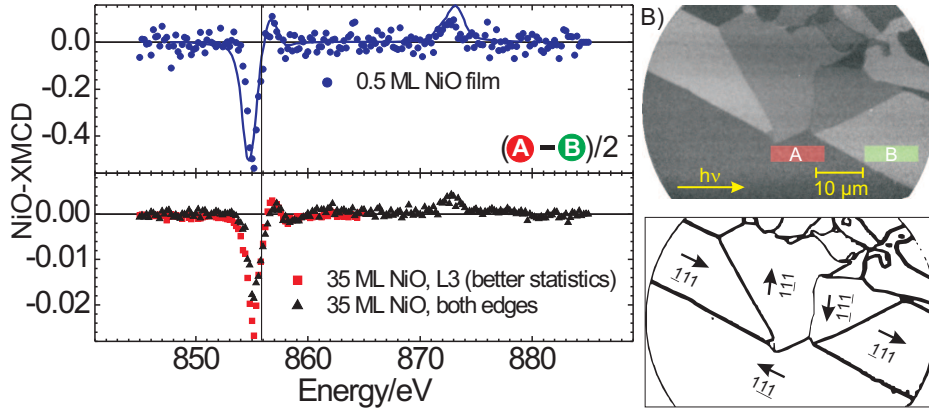


Figure 6.4.: (A) NiO: XMCD microspectra from the ROIs A and B. **0.5 ML coverage:** blue circles (experiment) and line (theory for Ni d^8 in O_h symmetry from Ref. [160]). **35 ML NiO film:** red squares and black triangles. Vertical line: Energy position for ratio image. (B) Ni-XMCD ratio image and (C) magnetization map derived from the spectra. Ni moments in the 0.5 ML layer are fully parallel to Fe_3O_4 .

6.3.3. Orientation of the spin-axis in NiO – determination of the coupling type

In the last section we found that the domains seen in Ni-XMCD are the same as in the Fe_3O_4 substrate, and the interfacial Ni spins are coupled parallel to the net magnetization in Fe_3O_4 . The question is now, how the antiferromagnet will respond to the domain formation in the substrate. It is tempting to conclude that from this situation a collinear coupling of the remaining antiferromagnet will result. Such a conclusion, however, would be premature, since it would derive the coupling type solely from the direction of the "uncompensated" magnetization of one interfacial monolayer. One should be aware, that besides the direction of the interface exchange anisotropy there are other important factors which influence the coupling, such as magnetoelasticity. Since in the experiment, collinear coupling of the antiferromagnet was indeed found, a detailed explanation for its origin must be given in terms of the interface structure and additional magnetoelastic effects. Anticipating that the $\text{Fe}_3\text{O}_4/\text{NiO}$ interface possesses a particular magnetic structure with a 1:1 matching of magnetic periodicities, there is no need for invoking random magnetic defects at the interface, in order to explain collinear coupling via the random-field effect.

In the antiferromagnet, the magnetic order cannot be accessed by circular dichroism due to the vanishing net moment. In case of collinear magnetism, however, the X-ray magnetic *linear* dichroism can provide information about the orientation of the spin-axis. Nevertheless, care has to be taken in single-crystalline systems, because the XMLD is generally "anisotropic" and depends on the spin-axis orientation with respect to the crystal lattice, as has been pointed out by ARENHOLZ *et al.* [8]. For a more detailed explanation of the "anisotropic" XMLD, please refer to Sec. 2.3.3.

In a pioneering work, ALDERS *et al.* used the XMLD contrast at the NiO L_2 edge to determine the spin-axis orientation in epitaxial NiO/MgO(001) [2]. They found a special statistical distribution with only $[\pm 1 \pm 1 \pm 2]$ type spin-axes, which is possibly caused by the epitaxial strain via magnetoelastic effects [60]. The XAS signal averaged over all these domains yields an angular dependence of the XMLD, which is axially symmetric to the film normal (z -direction). The problem can thus be modelled in O_h symmetry, with the spin pointing along the C_4 axis, and the dichroism magnitude is reduced as compared to the case $\mathbf{S} \parallel \mathbf{z}$ by the factor $\sin(54.73^\circ) = 0.82$. In this case, the XMLD contrast obtained from the ratio of the L_2 -double peak can be described by the simple relationship

$$I_{\text{XMLD}} = A + B \{ 3 \cos^2 \angle(\mathbf{E}, \mathbf{S}) - 1 \}, \quad (6.6)$$

where A represents the isotropic part and B the angular part of the spectrum. At this point it should be emphasized that this formula is applicable if and only if the overall symmetry of the Hamiltonian is *axial*, i.e. the crystal symmetry is either averaged out by integration over a large number of statistically oriented grains, or the sum over all magnetic domains yields rotational symmetry with respect to a C_4 or C_3 axis *or* if \mathbf{S} points along an axis of at least C_3 symmetry. In the general case, a complicated dependence of the spectral shape on the orientation of \mathbf{S} and \mathbf{E} with respect to the reference frame (in the easiest case: the crystal lattice) will result. In the case of NiO, we have to deal with O_h symmetry, since the material is crystalline cubic with uniform epitaxial orientation.

Cubic NiO has a particular electronic configuration which allows a relatively simple theoretical construction of arbitrary polarized XAS spectra from only two *fundamental spectra*. Since the ground-state is high spin d^8 , the t_{2g} subshell is completely filled, while the e_g representation is half filled with only spin-up electrons. First, this means that each representation possesses cubic symmetry, and there is no need to consider additional orbital degrees of freedom (compare Fig. 2.8 and Sec. 2.3.3). Because of the cubic symmetry, the orbital moment itself will be strongly quenched and the orbital moment anisotropy will not contribute substantially to the XMLD. The dominant mechanism will thus be XMLD by exchange and correlation effects (see Sec. 2.3.1). This is why atomic multiplet calculations neglecting the $3d$ spin-orbit coupling in the initial state describe the effect fairly well¹. The calculations together with the spin orientation-dependent dielectric tensor given in Eq. 2.38 make it possible to extract the spin-axis orientation from given NiO XAS spectra taken with different linear polarization orientations.

At this point, it should be emphasized that in the case of Fe_3O_4 , the situation is in principle more complicated due to the presence of different cation site symmetries (tetrahedral and octahedral) and valencies. However, summing over all sites in the unit cell must yield a cubic symmetry, and again the formalism used for NiO describes the experimental results fairly well. Consequently, the Fe_3O_4 -XMLD can be used for vectorial magnetometry as well. What remains to be shown is, that the observed contrast in NiO is indeed of magnetic origin.

Ruling out the Crystal field dichroism...

If the symmetry of the material under investigation is exactly cubic, no crystal-field dichroism will occur, and thus any observed contrast is due to the magnetic

¹Again it should be noted, that because the effect is described well without considering the $3d$ spin-orbit interaction, the "anisotropic" XMLD has no direct relation to the magnetocrystalline anisotropy in the sample.

order in the material. However, the growth of an epitaxial NiO layer on top of a substrate with a lattice mismatch will introduce a distortion, which induces an energy splitting of the two degenerate e_g -orbitals and the three degenerate t_{2g} -orbitals. Since Ni^{2+} is high-spin d^8 , the t_{2g} orbitals are completely filled and XAS transitions from the 2p core levels involve only the two z^2 and $x^2 - y^2$ orbitals of the e_g irreducible representation. Ergo, allowed transitions (with their relative intensities) are $|\langle d_{z^2} | C_0^{(1)} | p_z \rangle|^2 = \frac{4}{15}$, $|\langle d_{z^2} | \frac{1}{\sqrt{2}}(C_{+1}^{(1)} + C_{-1}^{(1)}) | p_{x,y} \rangle|^2 = \frac{1}{15}$ and $|\langle d_{x^2-y^2} | \frac{1}{\sqrt{2}}(C_{+1}^{(1)} - C_{-1}^{(1)}) | p_{x,y} \rangle|^2 = \frac{3}{15}$, as already discussed in Sec. 2.2.2. As one can directly see from the numbers, z -polarization exclusively probes the d_{z^2} -orbital, while xy -polarization mainly probes $d_{x^2-y^2}$. If there's an energy splitting between the two, for example, by crystal-field effects, switching between the two polarizations will result in an energy shift of the maximum transition intensity, which can be observed best at the sharp L_3 peak [60].

While the bulk structure of NiO deviates very little from cubic symmetry, thin films grown onto a substrate can experience significant distortions due to lattice strain, if they are not relaxed. In case of a (001)-oriented interface, there will be a tetragonal distortion, which can be very sensitively determined by the method described above, since the film will, for example, expand along the z -direction, while it contracts in the xy -plane, strongly affecting the e_g -orbitals, which have lobes along the cubic axes. For the (110) oriented sample, the strain in that plane will, however, result in a symmetry lower than tetragonal (monoclinic). This case cannot be described easily by theory, which might be the reason, why to date no calculations exist that quantify the splitting. If the monoclinic distortion is small, the d orbitals for cubic symmetry will still be a good basis, but the energetic splitting of the states within the different irreducible representations is substantially different from tetragonal symmetry. As can be seen in Ref. [119], in any case the d_{z^2} and $d_{x^2-y^2}$ orbitals will split, so a shift should be observable in the L_3 peak energy. Since the strain does not work in the direction of specific d orbitals, but rather linear combinations between them, the energy-shift in the spectra might, however, not be as pronounced as in the case of a tetragonal distortion. In Fig. 6.5, two spectra with s- and p- polarized light are compared for the Fe_3O_4 (110)/NiO[35ML] sample. Obviously, within the experimental resolution (0.2eV), there is no shift in the L_3 peak position, which is an indication that the crystal field effects are indeed very small.

For the application of vectorial magnetometry, it is important to determine whether the observed contrast vanishes above the ordering temperature of the material. In that case, one can conclude that the contrast is related to the magnetic order. Such a measurement is shown in Fig. 6.11, where the difference in the L_2 ratio for two different AF domains is plotted versus temperature. One can directly see that the contrast vanishes around 480 K, which is lower than the bulk

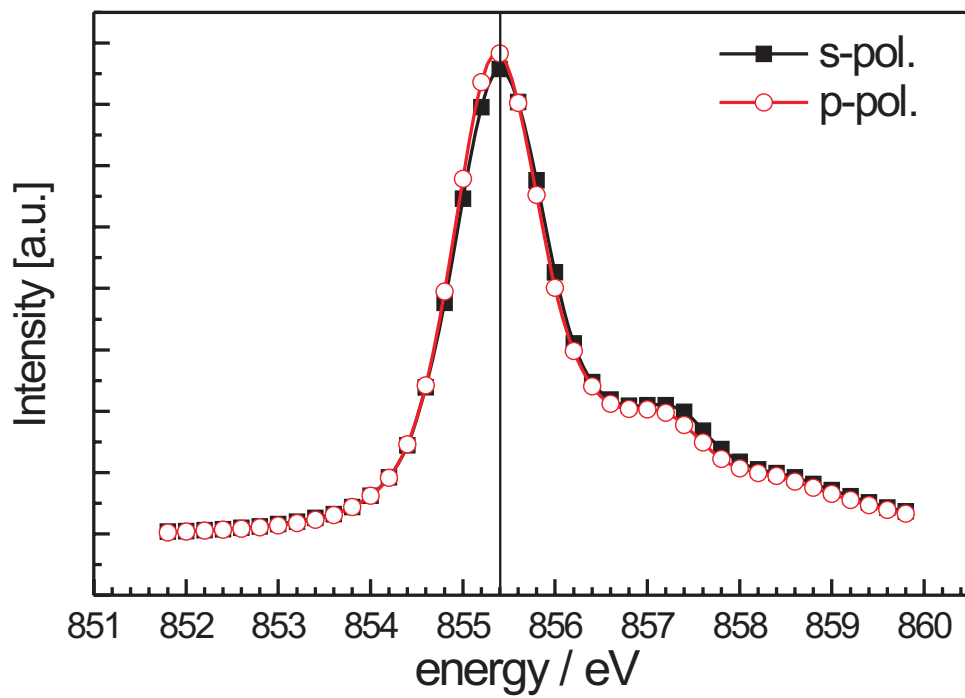


Figure 6.5.: Vanishing crystal field dichroism. Spectra with p- and s-polarized light show no shift in the maximum of the L_3 -peak. Thus the crystal field dichroism resulting from the small in-plane lattice mismatch of 0.5% is negligible.

NÉEL temperature of 523 K due to the finite size and blocking effects in the thin AF film. Thus, the contrast is indeed related to magnetism, but is it also *magnetic*? In principle, one might argue, that the origin may just as well be XMLD related to magnetoelastic domains caused by *exchange-striction*. Different distortions in adjacent domains would then locally break the cubic crystal symmetry, producing domain contrast by natural linear dichroism. However, one should keep in mind, that exchange-striction is generally small in NiO (for example only about 10^{-3} relative contraction along [111])[172, 174] and that – if present – such effects only provide a small contribution to the overall contrast. Hence, one can tacitly assume that the observed contrast is – to the largest extent – XMLD, which is directly related to the presence of long-range antiferromagnetic *spin* order in NiO. The main mechanism is the probing of the exchange-split density of states in the 3d shell by the polarized XAS-process, amplified by the exchange and correlation effects in the 2p core hole.

Experimental results: Collinear vs. perpendicular coupling

Having discussed the necessary prerequisites for a straightforward interpretation of the magnetic contrast, we will now turn to further experimental results. In Fig. 6.6 (G) and (H), the microspectra of the NiO L₂-peak are shown for the domain sets *I* and *II*, taken from the same image regions 1-5 as used previously for the Fe₃O₄-XMCD. In (E) and (F), the corresponding parameter images of the L₂-ratio $R = I(L_{2a})/I(L_{2b})$ are shown. In the s-polarized case, the reduced number of gray-levels catches the eye. Now, each domain-set is represented by a single gray value, since the linear dichroism contrast is only sensitive to an axis, not a direction, as would be the case for circular dichroism.

In Fig. 6.6, the experimental XMLD contrast is compared to plots of the theoretical L₂ asymmetry. Panels (A) and (B) show the XMLD manifold for the full solid angle of spin orientations, in p- and s-polarized geometry, respectively², while in panels (C) and (D), only the *in-plane* anisotropy is plotted. It is immediately clear that the simple $\cos(\mathbf{E}, \mathbf{S})^2$ -dependence Eq. 6.6 is not valid in the general case, since the symmetry of the XMLD manifold is not axial around the polarization direction (shown as green arrows in (A) and (B)). Only if either \mathbf{E} or \mathbf{S} is parallel to an axis of C₃ or higher symmetry, the latter is recovered, however, with different pre-factors for a C₃ axis $\langle 111 \rangle$ or a C₄ axis $\langle 001 \rangle$. By comparing the observed XMLD contrast for p- and s-polarization to the theoretical spectra, it is possible to discriminate between collinear and perpendicular coupling.

² $\theta'_s = 106^\circ$ and $\phi'_s = 62^\circ$ in surface coordinates $\mathbf{x}_s \parallel [\bar{1}10]$, $\mathbf{y}_s \parallel [001]$ and $\mathbf{z}_s \parallel [110]$

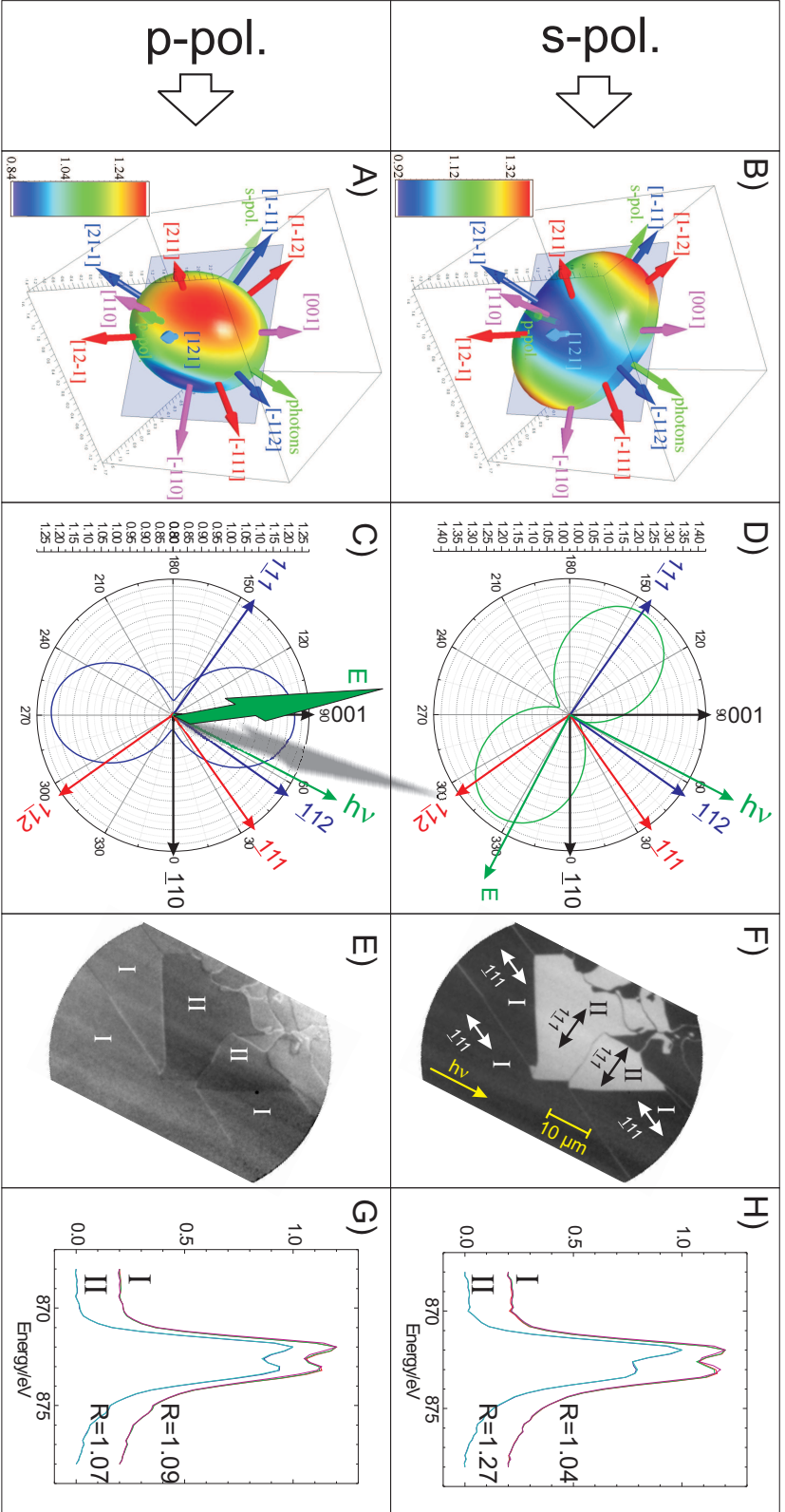


Figure 6.6: Anisotropic NiO-XMLD in Fe_3O_4 (110)/NiO: Upper row: s-polarization. Lower row: p-polarization. In (A) and (B), the XMLD manifold $\mathfrak{M}_{\mathbf{E}}(\mathbf{S})$ is plotted for the full solid angle of spin directions. The red vector quartet shows the magnetite $[111]$ easy-direction (*domain-set I*) and the three easy axes in NiO, which are perpendicular to it and thus allow spin-flop coupling. The blue vector quartet shows the $[1\bar{1}\bar{1}]$ easy direction *domain-set II* and the three NiO easy axes perpendicular to it. (C) and (D) show the in-plane anisotropy only. (E) and (F) are PEFM images of the NiO L_2 ratio. The full L_2 -spectra and experimental L_2 ratios R are shown in (G) and (H).

Although atomic multiplet calculations performed by MAURITS HAVERKORT were available, the XMLD values theoretically calculated by Eq. 2.38 were calibrated to earlier experimental data, employing the fundamental L_2 ratio values derived by ALDERS *et al.* in MgO(001)/NiO layers. These data have the advantage, that they were measured for room temperature (the same as in our measurements), whereas atomic multiplet calculations at present are only available for 0 K. To briefly repeat the matter: In the work of ALDERS *et al.*, a domain distribution with only $[\pm 1 \pm 1 \pm 2]$ -type domains led to an effectively uniaxial sample compatible with the case $\mathbf{S} \parallel \mathbf{z}$, the C_4 sample normal. This is why the XMLD could be described by the simple relationship given in Eq. 6.6, and the values of the L_2 -ratio extrapolated for the incidence angle with respect to the surface normal $\theta = 0^\circ$ ($\mathbf{E} \perp \mathbf{S}$) and $\theta = 90^\circ$ ($\mathbf{E} \parallel \mathbf{S}$) represent the fundamental quantities $\epsilon_{\perp} = 1.25$ and $\epsilon_{\parallel} = 0.82$, respectively. Using those values, it is again possible to calculate the expected contrast for the most probable spin orientations, which are given in Table. 6.1. Note, that because we calculate the contrast from reference data derived in a different experiment on a different material system (MgO(001)/NiO), the values for the L_2 ratio may not be *exactly* comparable for the same experimental geometry. Discrepancies can arise from (i) additional strain in the MgO/NiO layers, i.e. a crystal field contribution, (ii) a different experimental resolution or (iii) a slightly deviating evaluation technique. The *anisotropy* of the contrast, i.e. the relative contrast between different domains should, however, solely depend on the general relation of Eq. 2.38 as well as the temperature, which is the same in our experiment (room temperature).

Let's start with s-contrast and *domain-set II*, for example, where the substrate magnetization is parallel to $[\underline{111}]$. In the PEEM image for s-contrast in Fig. 6.6 (F), *domain-set II* showing a high L_2 ratio of 1.27 is considerably brighter than *domain-set I*, as can be seen in microspectra from that region in (H). Comparing to (B) and Table. 6.1, such high contrast values are only expected for $\mathbf{S} \parallel [\underline{111}]$ (*in-plane* collinear) and $\mathbf{S} \parallel [\underline{112}]$ (*in-plane* quasi-collinear), but not for $\mathbf{S} \parallel [\underline{112}]$ (*in-plane* spin-flop), and not for $\mathbf{S} \parallel [\underline{211}]$, $[\underline{121}]$ (*out-of-plane* spin-flop). For *domain-set I*, one finds experimentally a considerably lower contrast of 1.04 from (F) and (H). Since the substrate magnetization is parallel to $[\underline{111}]$, we are left with the possible coupling directions shown as red arrows in (B) and tabulated Table 6.1 (quasi-collinear: $[\underline{112}]$, *in-plane* spin-flop: $[\underline{112}]$ and *out-of-plane* spin-flop: $[\underline{211}]$, $[\underline{121}]$). *In-plane* spin-flop would produce a high contrast, which is not observed, and would lead to a contrast inversion between *set I* and *set II* as compared to experiment, while *out-of-plane* spin-flop coupling would lead to a difference value much lower than the one found experimentally. As a result, *in-plane* as well as *out-of-plane* spin-flop coupling can be directly ruled out.

For p-contrast, the outcome of the analysis is quite similar. *In-plane* collinear

and quasi-collinear coupling produce realistic contrast differences between *set I* and *set II*, while spin-flop coupling would lead to either inverted contrast or unrealistically large values. Hence, it can finally be concluded that the NiO spin-axis tends to align in the sample plane, *collinear* to the substrate magnetization.

When describing the results of the Ni-XMCD measurements, it was concluded that only a very thin zone near the interface produces XMCD, i. e. the uncompensated moments reside near the interface and are coupled parallel to the substrate magnetization. The question is now, how far the influence of the substrate extends into the NiO layer. One could, for example, speculate that the AF has an uncompensated magnetization at the interface, but the rest of the layer has a magnetic order that is completely unrelated to the substrate domain pattern. In this (extreme) case, also the XMLD contrast would only stem from the interface region, and nothing (or little) could be said about the bulk of the NiO layer. Such a situation can be identified by looking at the magnitude of the XMLD contrast. Any inhomogeneity leads to a deviation of the contrast characteristics from that of a bulk crystal or a homogeneous thin layer of NiO. Looking at Table 6.1, one can indeed see a very good accordance of the contrast difference between the two domain-sets to values characteristic for a homogeneous film. This means, that essentially the *complete* NiO layer exhibits the AF domain pattern, and not just a part of it.

After we gained information about the possible interface reconstruction phase and the coupling type, we are left with the intriguing question, which mechanisms lead to the favouring of collinear coupling over a spin-flop state. It is well-known, that in case of a fully compensated interface, spin-flop coupling should result, as first postulated by KOON [75] and found experimentally, e. g., for PtMn(001)/Fe [48]. At first glance, the [110] interface is fully compensated, as far as NiO is concerned. However, an interface always has two sides and thus that conclusion would be too rash.

Since Fe_3O_4 has twice the lattice constant of NiO, it is possible that the two magnetic sublattices \mathbf{S}_1 and \mathbf{S}_2 of the antiferromagnet couple differently to the ferrimagnet. To make this clear, a sketch of a possible crystalline structure of the interface is given in Fig. 6.7, where a reconstruction of the interfacial monolayer to $NiFe_2O_4$ is simply assumed. As will be discussed in a later section (Sec. 6.3.4), there are good reasons for this assumption: First, in this way the inverse spinel structure of the substrate is retained also at the interface. Second, this structure provides a way to place the Ni cations on strongly preferred octahedral sites. This has been verified experimentally by the Ni-XMCD signature, which is consistent with calculations of a NiO_6 cluster. In order to retain charge neutrality, charge ordering at the octahedral cation sites might occur, with the iron cations

s-pol.	set I dir./L₂-ratio	set II dir./L₂-ratio	diff.
exp	1.04	1.27	-0.23
theo			
in-plane coll.	[$\underline{111}$]/1.05	[$\underline{111}$]/1.39	-0.34
in-plane quasi-coll.	[$\underline{112}$]/1.02	[$\underline{112}$]/1.35	-0.33
in-plane SF	[$\underline{112}$]/1.35	[$\underline{112}$]/1.02	0.33
out-of-plane SF	[211]/ 1.02 ; [$\underline{121}$]/1.02	[$\underline{211}$]/0.94 ; [121]/ 0.94	0.08
p-pol.	set I dir./L₂-ratio	set II dir./L₂-ratio	diff.
exp	1.09	1.07	0.02
theo			
in-plane coll.	[$\underline{111}$]/0.99	[$\underline{111}$]/0.96	0.03
in-plane quasi-coll.	[$\underline{112}$]/1.11	[$\underline{112}$]/1.09	0.02
in-plane SF	[$\underline{112}$]/1.09	[$\underline{112}$]/1.11	-0.02
out-of-plane SF	[211]/1.30 ; [$\underline{121}$]/1.11	[$\underline{211}$]/1.17 ; [$\underline{121}$]/1.26	0.13 ; -0.15
	[$\underline{121}$]/1.11 ; [211]/1.30	" ; "	-0.06 ; 0.04

Table 6.1.: Experimentally determined and theoretically predicted values for the NiO L₂ ratio for the cases of *in-plane* collinear coupling, *in-plane* and *out-of-plane* spin-flop coupling in the (110) interface orientation.

favouring the Fe³⁺ valency, which would lead to an enhancement of the octahedral Fe magnetic moment by 125% from 4 to 5 μ_B . This effect could account for the enhancement of the observed Fe-XMCD (later in this chapter). In Fig. 6.7, two possible terminations A and B are shown, which both have in common that there is an ordered array of octahedral vacancies and Ni²⁺ sites. Comparing to the structure of a NiO like surface, it is directly obvious that NiO can assume a magnetic order in which the two antiferromagnetic sublattices experience different coupling environments. In a simple model, one can show that for a simple coupling of a two sublattice antiferromagnet to a ferromagnet with coupling constants $J_F^{(1)}$ and $J_F^{(2)}$, collinear coupling wins over spin-flop coupling, if the difference between $J_F^{(1)}$ and $J_F^{(2)}$ exceeds a certain threshold.

This can be made clear in a simple picture of one AF monolayer coupling to a ferromagnetic substrate [51]. If we assume that there are two sublattices \mathbf{S}_1 and \mathbf{S}_2 in the antiferromagnet, we can introduce the exchange coupling constants

$$J_F^{(1)} = \bar{J}_F + \frac{\Delta J}{2} \quad , \quad J_F^{(2)} = \bar{J}_F - \frac{\Delta J}{2}. \quad (6.7)$$

Assuming that the rotation of the spins is confined to the film plane by some kind of dipolar anisotropy, a simple energy functional can be written down as

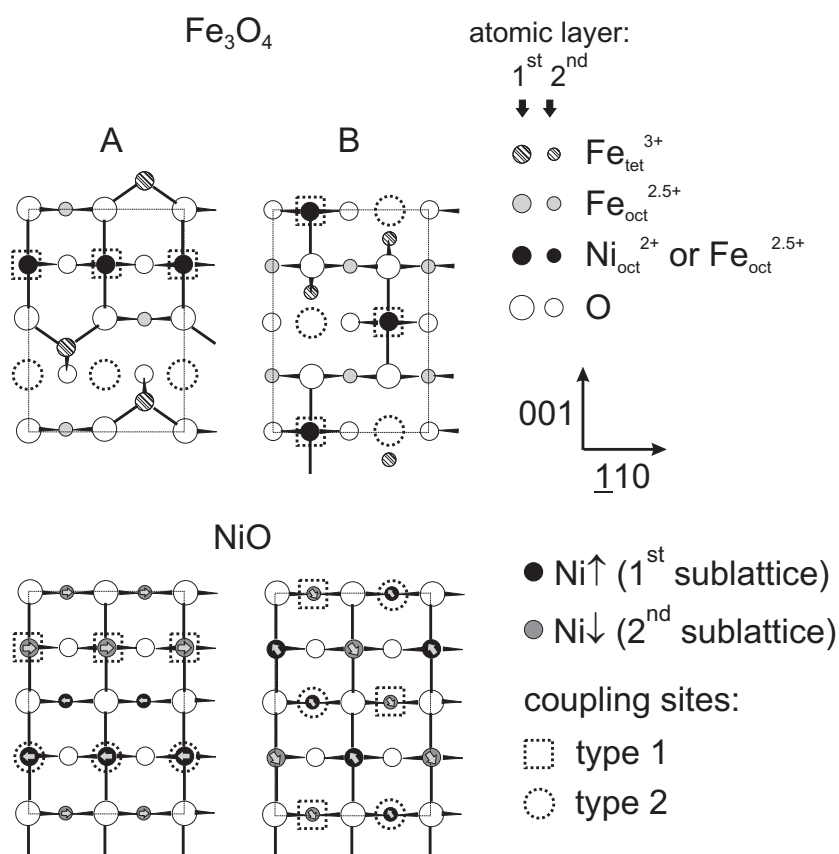


Figure 6.7.: Sketch of the bulk-terminated (110)-surfaces of Fe_3O_4 and NiO. In Fe_3O_4 , there are two possible terminations (A and B). For each of the two, there is a matching T-domain in NiO, which leads to inequivalent coupling of the two (spin-up and spin-down) sublattices. If the interfacial layer reconstructs to $NiFe_2O_4$, octahedrally coordinated iron cations are replaced by Ni.

follows:

$$F = -J_F^{(1)} \mathbf{S}_1 \cdot \mathbf{M} - J_F^{(2)} \mathbf{S}_2 \cdot \mathbf{M} + J_{AF} \mathbf{S}_1 \cdot \mathbf{S}_2 \quad (6.8)$$

Assuming further that each sublattice site bears the same magnetic moment $|\mathbf{S}_1| = |\mathbf{S}_2| = S$, then Eq. 6.8 can be rewritten in terms of the in-plane rotation angles as

$$F = -J_F^{(1)} \cos \phi_1 - J_F^{(2)} \cos \phi_2 + J_{AF} \cos(\phi_1 - \phi_2), \quad (6.9)$$

where $\phi_{1,2}$ are the respective angles of the sublattice spins with respect to the substrate magnetization \mathbf{M} . A critical point in the free energy exists, if the gradient vanishes:

$$J_F^{(1)} \sin \phi_1 - J_{AF}(\sin \phi_1 - \phi_2) = 0 \quad , \quad J_F^{(2)} \sin \phi_2 + J_{AF}(\sin \phi_1 - \phi_2) = 0 \quad (6.10)$$

Minimum and stability conditions are given for the case of positive diagonal elements and a positive determinant of the HESSEian matrix, respectively

$$J_F^{(1)} \cos \phi_1 - J_{AF} \cos(\phi_1 - \phi_2) > 0 \quad , \quad J_F^{(2)} \cos \phi_2 - J_{AF} \cos(\phi_1 - \phi_2) > 0 \quad . \quad (6.11)$$

$$\left(J_F^{(1)} \cos \phi_1 - J_{AF} \cos(\phi_1 - \phi_2) \right) \left(J_F^{(2)} \cos \phi_2 - J_{AF} \cos(\phi_1 - \phi_2) > 0 \right) - J_{AF}^2 \cos^2(\phi_1 - \phi_2) > 0 \quad . \quad (6.12)$$

The gradient vanishes for collinear coupling, i.e. $\phi_1 = 0$ and $\phi_2 = -\pi$. In this case, Eq. 6.10 and Eq. 6.12 yield

$$J_F^{(1)} + J_{AF} > 0 \quad , \quad J_{AF} - J_F^{(2)} > 0 \quad , \quad J_{AF}(J_F^{(1)} - J_F^{(2)}) - J_F^{(1)} J_F^{(2)} > 0 \quad . \quad (6.13)$$

It is directly clear that if $J_F^{(1)} = J_F^{(2)}$, collinear coupling is unstable. In this case, a possible solution is $\phi_1 = \frac{\pi}{2} + \gamma$ and $\phi_2 = \frac{\pi}{2} - \gamma$ (spin-flop coupling), where γ is the canting angle of the sublattices towards the net magnetization. Of course, this model accounts only for the coverage of one monolayer, but a similar approach is possible for thicker films, requiring numerical computations.

6.3.4. Ultrathin proximity zone at the interface

To have a closer look at the magnetic structure directly at the interface, a wedge experiment has been performed, from which quasi depth-dependent information can be gained. For this purpose, a NiO stepped wedge was prepared onto the bare Fe₃O₄ (110) substrate, with a step height of 2.5 Å and 50 μm wide steps³.

³The steps were created by retraction of a shutter directly in front of the sample.

The preparation resulted in 20 μm wide step slopes, which allow a convenient thickness-resolved measurement in PEEM. It turned out that the crucial changes in magnetic structure happened already at the first step slope, i.e. within the first few monolayers at the interface. This verifies the earlier finding that the proximity zone is only a few lattice constants wide.

PEEM images and line profiles of that area are shown in Fig. 6.8. Clearly, the Ni-XMCD increases up to a coverage around one ML, then drops down again and remains constant for thicknesses greater than 1.5 ML. Fig. 6.9 shows closeup images and lineprofiles of the slope region around 1 ML. The extremal contrast can be observed in all contrasts, the Ni-XM(C/L)D and Fe-XMCD. While the Ni-XMCD is enhanced up to 20% as compared to thicknesses greater than 1.5 ML, the Fe-XMCD is only enhanced by about 3%. The Ni-XMLD shows a sharp dip at the extremal location. In Fig. 6.8 (G), the sharp dip cannot be observed maybe due to its small size, and the contrast gets darker with thickness, which corresponds to increased XMLD. The behaviour is generally linear with thickness, besides a small nonlinearity at coverages smaller than 0.25 \AA .

The PEEM images alone do not allow for a separation of spin and orbital moment, since the contrast derived by computing the asymmetry at one particular energy is always proportional to a weighted sum of m_{orb} and m_{spin} . Therefore, microspectra from PEEM image stacks have to be used for a sum rule analysis. This has been done for the Ni-XMCD as shown in Fig. 6.10. Note that in the inset, the total moment shows a similar behaviour as the Ni-XMCD line profile, an increase up to one ML and then a slight decrease with approximately constant values above 1.5 ML. Looking at the separated moments, it appears that the extremum at one ML is caused by the orbital moment, while the spin-moment increases up to one ML and varies little for greater thicknesses. This means that the uncompensated spin moments reside directly at the interfacial monolayer, and all further material deposited on top is almost fully antiferromagnetic. The orbital moment enhancement in the Ni cations – and possibly also the enhanced Fe (orbital) moment can have three possible origins:

First, the low dimensionality at one ML coverage creates a strong bonding anisotropy lower than cubic, which might lead to an enhancement of the orbital moment, which is strongly suppressed in cubic symmetry. Similar effects have been observed earlier in ultrathin film wedges [149]. Looking at the L/S ratio, the maximum value is, however, around 0.21, which is close to the experimental and theoretical values (0.27) for $NiFe_2O_4$ or $Ni^{2+} O_h$ [160]. This might imply that the orbital moment has its full value only at the interface or at one ML coverage and drops down considerably (almost to zero) inside the following layers. This could be a consequence of the re-established cubic symmetry, but contradicts theory and earlier experiments on NFO, where a strong orbital moment was observed

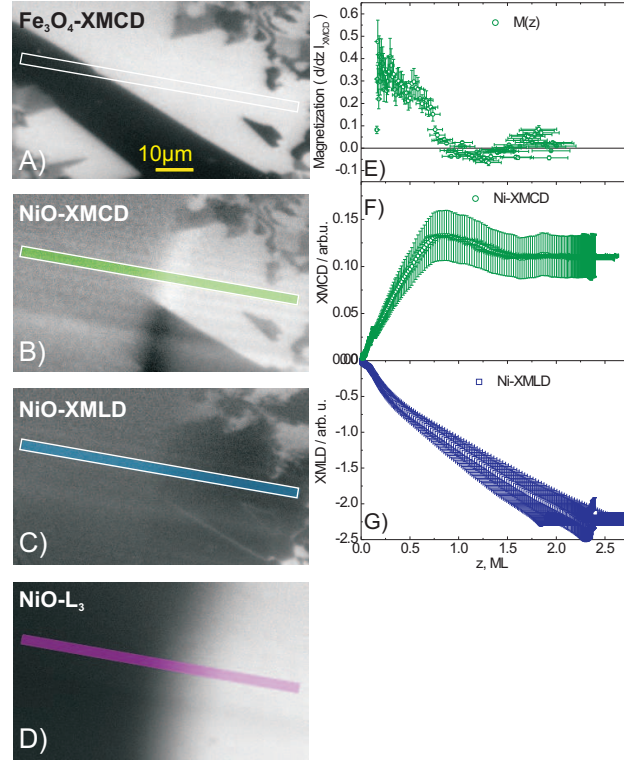


Figure 6.8.: Thickness dependent dichroism of a NiO wedge on top of Fe₃O₄ (110). A) Fe₃O₄-XMCD contrast (profile not shown). B) NiO-XMCD C) NiO-XMLD (s-pol.) D) NiO-L₃ white line intensity (used for normalization and determination of coverage). E) Depth dependent NiO magnetization $\frac{d}{dz} I_{\text{XMCD}} \propto M(z)$. F) Total NiO-XMCD $I_{\text{XMCD}} = \int_0^d m(z) dz$ at film thickness d. G) Total NiO-XMLD. While the XMCD shows a clear maximum around 1 ML, the XMLD increases almost linearly with thickness. Note that there is a sharp and small dip at one ML which can only be seen in Fig. 6.9. The derivation of the XMCD signal yields a quasi-depth-dependent magnetization (E), which seems to be confined to the first interfacial monolayer.

in spite of cubic symmetry, obviously reinstated by the 3d spin-orbit interaction (see Ref. [160] and references therein).

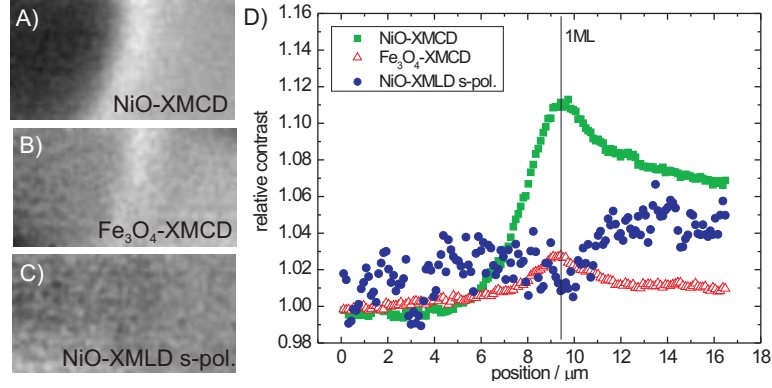


Figure 6.9.: Closeup of the slope region around one ML. Clearly, all dichroism signals exhibit an extremum near one ML. Sum rule analysis suggests that the effect is caused by the orbital moment (see Fig. 6.10).

A second explanation for the decrease of the orbital moment towards the second monolayer could be that the latter possesses no spin, but an orbital polarization, which is antiparallel to the first layer, thus compensating the orbital moment. In this context, it is interesting to note that in Fig. 6.10 there is a minimum in the Ni orbital moment at 2.2 ML, where m_{orb} is almost zero. For higher thicknesses, it increases again to finite (positive) values. Since only a single data point is affected, one might consider this an artifact. However, the spectra do not give evidence for any anomaly, so we believe this to be a real effect. Therefore, one can speculate that there is an oscillation in the orbital moment for successive monolayers near the interface. That could actually explain the compensation of the orbital moment at two monolayer thickness. In this context it is interesting to note that theoretically, an alternation in the AF uncompensated magnetization direction near the interface has been postulated in at least two studies [42, 68]. There, however, the spin-moment oscillates, since orbital effects have not been taken into account by the models. Third, the interface layer can reconstruct to a Nickel-ferrite phase NiFe_2O_4 , which is isostructural to Fe_3O_4 and contains Ni cations only on octahedral sites. As a consequence, there is an electronic interaction between Fe and Ni cations. This might have significant influence on the magnetic structure. For example, redistribution of charge between Fe and Ni cations could lead to a significant change in the magnitude of their net spin moments. Nevertheless, charge ordering will also influence the size of the respective orbital moments.

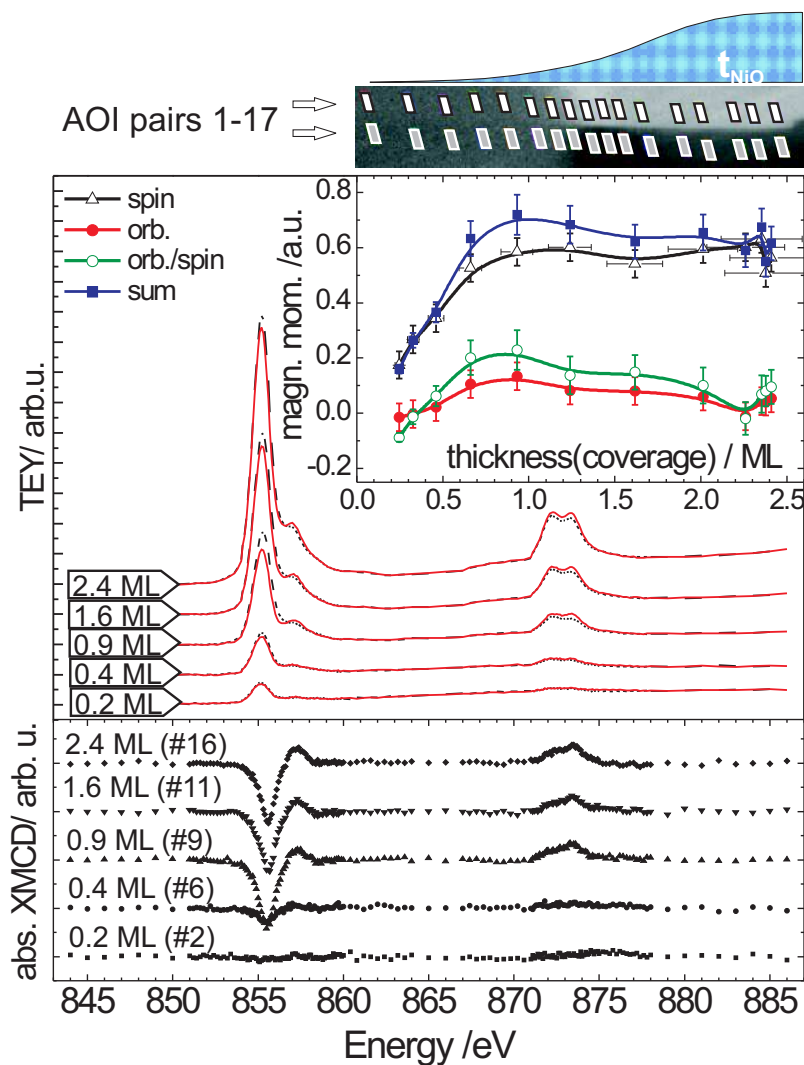


Figure 6.10.: Local microspectra of the thickness dependent NiO-XMCD. The inset shows the thickness dependent magnetic moments derived from sum rule analysis. Note that the moments are not in units of μ_B , since this would require normalization to the isotropic intensity and does not make sense in a vertically inhomogeneous film. Instead, the moments represent a measure of the total number of uncompensated moments at a certain thickness.

6.4. Temperature-dependence of the magnetic contrast

6.4.1. Introduction

A free (uncoupled) layer of NiO should have a temperature dependence of its order parameter similar to the bulk material, but it also exhibits finite size effects from the limited thickness, if it is very thin (see Ref. [2] for details). In a layer which is magnetically coupled to a substrate, however, two contributions to the temperature dependence should be observable: One contribution stems from the volume material in the layer, which does not experience the short range interface exchange interaction. A second contribution may arise from the interfacial region, showing a different characteristics due to its reduced dimension (quasi 2D) and the different interface exchange coupling. The so-called *blocking temperature* is usually seen as the critical point at which the AFM anisotropy barrier is overcome, the correlation length of the internal fluctuations becomes greater than the AF domain dimensions and any local exchange bias vanishes. In the PEEM images this corresponds to the disappearance of any domain contrast in the AF layer. Note that above T_B , the antiferromagnet still possesses long range order, which vanishes at $T_N \geq T_B$, but is effectively single domain.

6.4.2. Experimental procedure

To obtain the temperature dependence of the magnetic contrast for the ferri- and antiferromagnet, PEEM images were computed as described earlier – now at different sample temperatures after an appropriate settling time. The substrate contrast was generated by the Fe-XMCD signal, and the NiO contrast by the NiO L_2 ratio. After careful subtraction of an eventual nonlinear background in the images, arising, for example, from x-ray mirror interference patterns, and inhomogeneous illumination, the difference between the magnetic contrast in different domains was computed. In the antiferromagnet, different T-domains were chosen, whereas in the ferromagnet, two 180° -domains yielded maximum contrast. The sample temperature was allowed to stabilize, sometimes for hours to minimize thermometry errors and to avoid thermal sample drifts.

The results of the measurements are shown in Fig. 6.11. Half the data points were gained on the upward ramp until no domain contrast was visible anymore in the images⁴, the remaining intermediate values were collected during cooling

⁴It turned out later that after background subtraction and contrast enhancement, a (very) small contrast became apparent.

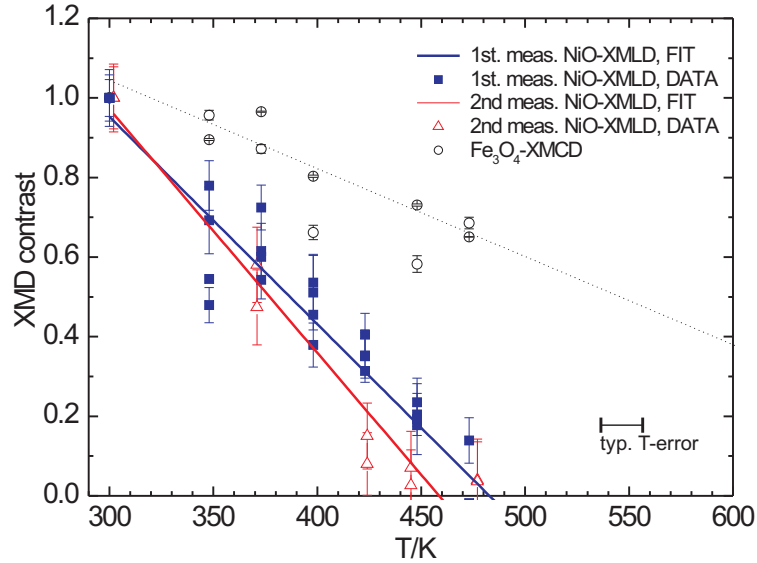


Figure 6.11.: Temperature dependence of the AF domain contrast. The values represent the difference between the NiO L_2 ratio for ROIs in different T-domains. The contrast decreases as the temperature approaches the blocking regime. A second heating/cooling cycle results in a reduction of T_B . Fits with a simple linear relationship show that T_B is around 483 K and 459 K for the first and second measurement, respectively. This value is well below the bulk Néel temperature of NiO (523 K), but close to the reduced T_N found in NiO films of comparable thickness on MgO(001)[2]. For comparison, the substrate domain contrast is also shown. The black open circles represent the contrast difference of two ROIs located in a pair of 180° -domains. Astonishingly, the magnetite contrast reduces considerably, as the temperature is increased. A linear extrapolation (dotted line), which should overestimate T_c , yields a Curie temperature *lower* than the bulk. Note: The vertical error bars represent the sum of the gray-level standard-deviations in the two ROIs.

down. Besides slight variation of the domain topology with temperature, up- and down-ramp values seem to lie on the same curve, implying that during the heating process nothing changed irreversibly in the magnetic characteristics of the sample. Two heating measurements were performed with an interval of about two weeks in between, the sample being kept in UHV. Interestingly, the second measurement yielded a lower blocking temperature than the first, with each of the data sets showing a single characteristics for heating and cooling. The reduction in T_B between successive measurements implies that the sample is not left unaffected by the heating process, but is magnetically annealed. Since during each single measurement run, no change in the blocking temperature has been observed, the alteration seems to be due to some kind of thermally activated magnetic aftereffect, similar to a thermal training effect reported in Ref. [168]. The reduction in T_B can be caused by a decrease of pinning centers for the AF domain walls, thereby facilitating the removal of the domain state by domain wall creeping. Another possible origin could be a reduced interface coupling strength or a different interfacial anisotropy. In Chap. 8 it will be shown that the interfacial anisotropy – and driven by it also the AF anisotropy – is indeed changed by the annealing.

In Fig. 6.12, mean-field calculations of the temperature-dependent behaviour of three important quantities are plotted: (i) The expectation value of the magnetic moment $\langle \boldsymbol{\mu} \rangle$, which determines the magnitude of the XMCD contrast. (ii) The squared expectation value $\langle \boldsymbol{\mu}^2 \rangle$, which is measured for example in neutron-scattering experiments. This quantity also describes the nearest-neighbour spin-spin correlation function, which can contribute to the XMLD as shown in Ref. [3]. (iii) The expectation value of $\langle \boldsymbol{\mu}^2 \rangle - 1/3J(J + 1)$, which provides the major contribution to the XMLD contrast [154]. As can be clearly seen, the XMLD contrast follows an almost linear relation when the temperature is greater than $0.6T_N$.

In order to quantify the NÉEL and blocking temperatures, the NiO XMLD data were fitted to the a linear function like $\propto (T_B - T)$ (Fig. 6.11) as well as adapted to the universal curve of $\langle \boldsymbol{\mu}^2 \rangle - 2/3$, which accounts for the NiO-XMLD (Fig. 6.12). The NiO XMLD data are in good accordance with the 3D mean field picture, where the expectation value of the magnetization near T_B scales like $\langle \boldsymbol{\mu} \rangle \propto (T_B - T)^\beta$, $\beta = 0.5$. Since XMLD measures $\langle \boldsymbol{\mu}^2 \rangle$, the contrast scales like $(T_B - T)^{2\beta}$.

Although the 3D mean-field model yields a good agreement to the data, it is mandatory to briefly discuss other models for the critical behaviour. A 2D mean field characteristics with $\beta = 1$ – as found for the surface of a NiO(001) crystal [99, 105] – can definitely be excluded, since fitting the contrast with a parabola yields a $T_B > T_{N,\text{bulk}}$, which is unlikely due to the finite size effects in the AF,

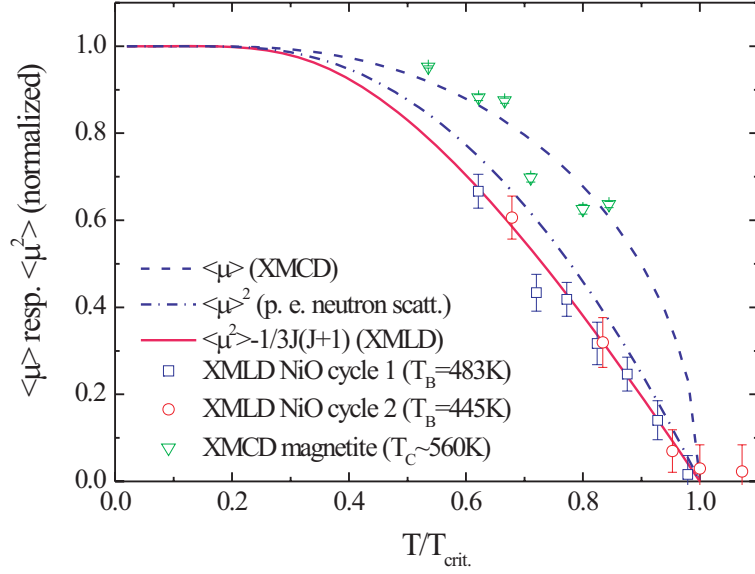


Figure 6.12.: Mean-field calculations for the thermal expectation value of the atomic magnetic moment $\langle \mu \rangle$ (XMCD), the squared expectation value $\langle \mu \rangle^2$ (for example neutron scattering) and the expectation value of the squared moment $\langle \mu^2 \rangle$. The XMLD contrast is proportional to $\langle \mu^2 \rangle$ minus the isotropic value $1/3J(J+1)$. Temperatures are normalized to the critical temperature, expectation values to 1 at 0 K. The experimental XMLD contrast values from the first and second heating cycles have been fitted to the universal relationship of $\langle \mu^2 \rangle - 1/3J(J+1)$, $J = 1$. Clearly, the accordance is very good, and the blocking-temperatures obtained from this procedure are $483 \pm 20(445 \pm 20)$ K for the first (second) heating cycle. The Fe_3O_4 XMCD contrast has been adapted to $\langle \mu \rangle$, which yielded an approximate CURIE temperature much lower than in the bulk ($T_C \approx 560$ K). Due to the low probing-depth of the XMCD ($\approx 10 \text{ \AA}$ [50]), the reduced critical temperature probably exists only near the $\text{Fe}_3\text{O}_4/\text{NiO}$ -interface and is caused by the magnetic proximity effect.

which *lower* T_N [2]. A 2D ISING behaviour can be ruled out, since the exponent $\beta = 1/8$ would yield a much steeper descent at T_B . 3D HEISENBERG with $\beta \approx 1/3$ cannot definitely be excluded, but it would yield a slightly lower T_B and a nonlinear temperature-dependence near the critical temperature ($\langle \mu^2 \rangle \propto (T_B - T)^{2/3}$). As a result, the data suggest that the critical exponent lies somewhere between $1/3$ and $1/2$, probably closer to $1/2$, which strongly hints a 3D mean-field behaviour at the blocking temperature.

The fits yielded $T_B = 483 \pm 10 \text{ K}$ ($445 \pm 10 \text{ K}$) for the first (second) measurement, respectively. These values are considerably lower than the bulk NÉEL temperature of NiO (523 K), but comparable to T_N -values of thin films of similar thickness on MgO(001) [2]. A determination of the NiO L_2 ratio, which is a measure for the long range order in NiO, yields a value around 1.12 at T_B , which is close to the isotropic value of 1.06. This means that the film is still antiferromagnetic, but only slightly below its NÉEL temperature. Consequently, T_B and T_N are very close, possibly even identical.

Although the system under consideration represents the reverse case of exchange bias, namely an antiferromagnet dominated by the coupling to a ferrimagnet, it is interesting to note that a linear behaviour of the exchange bias field near T_B has been found in many systems [22, 163, 57, 90]. In most of them this characteristics was observed over a very large temperature range of more than $0.6 - 1 T_B$. This may be explicable by the interface exchange energy responsible for exchange bias. It is defined as $\sigma_{\text{int.}} \propto H_{\text{eb}} M_F \propto \langle \mu_{\text{AF}} \rangle \cdot \langle \mu_{\text{F}} \rangle \propto \langle \mu_{\text{eff.}} \rangle^2$, where $\mu_{\text{eff.}}$ is an effective magnetic moment. Therefore, one can expect an approximately linear behaviour of $\sigma_{\text{int.}}$ at least in the range $0.75 - 1 T_B$ according to Fig. 6.12. The interfacial exchange-energy has the character of a nearest-neighbour spin-spin correlation function $\langle \mathbf{S}_i \cdot \mathbf{S}_k \rangle$, or – in other words – a short-range order-parameter. This quantity has been investigated by ALDERS *et al.* [3] for the bulk of NiO layers. Their data were fitted to a mean-field $\langle \mu \rangle^2$ in the range of $0.4 - 1 T_N$, showing a slightly more linear behaviour than the model suggests. From this, we conclude, that our temperature-dependent XMLD-contrast might contain an additional contribution linear in temperature, stemming from the interfacial nearest-neighbour spin-spin correlation function. However, because of the similarity to the mean-field behaviour of the XMLD, we cannot separate this contribution.

Last but not least one observes in Fig. 6.11 and Fig. 6.12, that also the Fe_3O_4 XMCD contrast strongly decreases with increasing temperature. Due to the negative curvature of the mean-field $\langle \mu \rangle$, extrapolation of the data with a linear fit in Fig. 6.11 should strongly overestimate T_C . Astonishingly, this analysis yields values around 770 K, considerably lower than the bulk $T_c \approx 850 \text{ K}$ [87]. A more accurate value is gained from the adaptation of the XMCD contrast to the universal mean-field behaviour of $\langle \mu \rangle$ as shown in Fig. 6.12. As expected, an even

lower T_C of only about 560 K results. This implies that either the T_C is lower than for the bulk at the Fe_3O_4 (110) surface (interface), or that the enhanced Fe interface moment discussed in Sec. 6.3.4 shows a temperature dependence, which is more related to the AF layer than to magnetite – and thus has a T_C closer to the AF's T_N . The temperature dependence of the interfacial moment may then be related to the interfacial nearest-neighbour spin-spin correlation function discussed in the previous paragraph. In Chap. 8 we will provide more evidence that the Fe_3O_4 -XMCD is indeed very sensitive to the topmost monolayers of the Fe_3O_4 , which have a different magnetic anisotropy than the bulk – and probably also a different temperature dependence.

6.5. Summary

In this chapter, PEEM measurements of the Fe_3O_4 (110)/NiO system have been presented. The thin AF adlayer couples collinearly to the substrate, with the interfacial Ni spins parallel to the Fe_3O_4 net moment. At a NiO wedge, thickness-dependent measurements have been performed in order to extract quasi-depth-dependent information about the interfacial magnetic structure. At the interface, a maximum in the magnetization was found for Ni as well as for Fe at a thickness of exactly one monolayer. Explicit sum rule analysis of the thickness dependent Ni-XMCD spectra indicates that the enhancement is caused by the orbital moment, which peaks at one ML and drops down by 20% towards higher thicknesses. The fact that the L/S ratio of O_h Ni d^8 is of the same size implies that the orbital moment is nearly quenched in the bulk, in contrast to theoretical predictions[160]. The interfacial Fe moment is enhanced by a factor of 120-200% depending on the assumed probing depth. Transferring the results for Ni, also here the orbital moment could be the cause. It is well known that reduced dimensionality can enhance the orbital moment via bonding anisotropy effects. The results indicate that a monolayer of NiFe_2O_4 is formed at the interface. Temperature dependent measurements of the XMLD and XMCD contrast prove that the antiferromagnetic contrast is indeed of magnetic origin. The blocking temperature in the 35 ML NiO film is lower than the bulk NÉEL temperature due to finite size effects in the ultrathin layer. The XMLD contrast exhibits a linear temperature dependence in a wide range of $0.6 - 1 T_B$, which can be explained by a mean-field behaviour and possibly also by the temperature-dependence of the interfacial short-range order-parameter. The Fe_3O_4 -XMCD contrast suggests a T_C of about 560 K – much lower than the bulk value. The effect is very likely restricted to the vicinity of the interface, since XAS measurements at the Fe edge have a low probing depth of only 10 Å [50]. The lowered T_C might be related to the temperature-dependence

of the interface coupling and a crossover of the critical temperatures in Fe_3O_4 and NiO.

7. Influence of interface orientation on the coupling type

7.1. Introduction

A central aspect of the magnetic proximity effect is the interfacial crystallographic structure, which influences the coupling in two ways:

1. First, electronic effects will arise due to the breaking of translational symmetry, like, for example, anisotropic exchange, altered crystal-field symmetry and hybridization between the neighbouring materials. Those will be in general short-ranged, in particular for the oxidic materials used in our study. Thus, the purely electronic proximity effects are generally restricted to a very narrow region of a few atomic layers near the interface (see, for example, ref. [72] and references therein).
2. Second, in case of epitaxial lattice mismatch, magnetoelastic effects will depend on the orientation of the planar epitaxial strain with respect to the crystal lattice. In contrast to the short-ranged electronic interactions at the interface, the strain-induced effects will extend farther. In the two systems Ag(001)/NiO [60] and MgO(001)/NiO [2], the strain changes the ratio of the *out-of-plane* and *in-plane* lattice parameters c and a , respectively. This results in a preferred spin-arrangement *in-plane* for $c/a > 1$ and *out-of-plane* for $c/a < 1$. This effect has also been predicted theoretically by calculations of the dipolar anisotropy energy of NiO [43]. Moreover, magnetostriction in one of the constituents leads to magnetization dependent strain, which in turn influences the magnetic structure in the other via magnetoelastic coupling.

The importance of the crystallographic interface orientation has already been pointed out by NOGUÉS *et al.*, who experimentally found a dependence of the exchange bias field H_{eb} on the crystallographic orientation in single crystalline FeF₂-Fe systems [106]. In their study, magnetoelastic effects were first considered to contribute to the overall magnetic behaviour, but not discussed in great detail. QIAN *et al.* predicted theoretically, that the orientation-dependent crystal

field splitting has an important influence on the electronic and magnetic properties of the interface region [119]. Despite numerous other theoretical calculations of the proximity effect at interfaces (see, for example, Ref. [72] and references therein), still experimental studies are scarce, partly because only few techniques are able to investigate buried interfaces with high selectivity and/or depth resolution.

This chapter will provide some insights into how the crystallographic orientation influences the FM/AF magnetic proximity effect via exchange coupling and magnetoelastic effects. Experimentally, some discrepancies to the simple model proposed by KOON [75], were found, which predicts that for perfectly compensated interfaces, spin-flop coupling should result, while for (sufficiently) uncompensated interfaces, a collinear FM/AF alignment would be stabilized. It will be shown that those discrepancies do not mean that KOON's model is wrong, but rather that additional effects, such as magnetoelasticity, have to be considered in order to make the right predictions. In the author's opinion, magnetoelasticity has been underestimated so far in relation to exchange coupling, and more work has to be done for a quantification of both contributions.

Reliable conclusions in this context, however, will only be possible in highly-ordered systems. Thus, the choice of a well-ordered epitaxial system of low lattice mismatch is mandatory, as already explained earlier, and a good candidate for investigation is the $\text{Fe}_3\text{O}_4/\text{NiO}$ system used throughout this thesis.

The chapter is structured as follows: In Sec. 7.2, the method of sample preparation will be described. In sections 7.3.1-7.3.3, the experimental data of the three interfaces are presented and evaluated. In section 7.3.4, a quantitative comparison of the uncompensated magnetization arising at the three interfaces due to the interfacial exchange interaction and possible phase reconstructions will be performed. Finally, the results will be discussed in terms of exchange and magnetoelastic effects in Sec. 7.4, followed by a final summary.

7.2. Sample preparation

In this section, the preparation methods will be summarized and deviations in the recipes for different crystallographic surface orientations will be discussed.

7.2.1. Substrate and interface conditioning

All samples were prepared *in situ* and measured directly after preparation to study the as-grown magnetic structure and to avoid the necessity of capping. We used synthetic magnetite single crystals as substrates, which were polished to the respective crystallographic orientation to typically better than 0.5° . In UHV, they were treated by Ar-sputter- and annealing cycles at 850-1100 K in typically 10^{-6} mbar O_2 background pressure to obtain large and homogeneous domains and the right interface phase. Note that according to the phase diagram compiled in Ref. [84], stoichiometry should result in 10^{-6} mbar O_2 pressure in the whole range from 850-1200 K, which is not in accordance with our findings. Annealing times were usually several hours, followed by careful cooling in oxygen pressure (same as during annealing). The magnetic domain topology and surface stoichiometry was verified by PEEM images and fitting of local XMCD spectra to atomic multiplet calculations (for a description of the method, see Ref. [129] and Sec. 6.2 on page 59).

For the (110) interface, we adopted the recipe reported by JANSEN *et al.*, who found stoichiometry and good crystalline order for the (110) interface under treatment by sputter-anneal cycles up to 1200 K, both with and without oxygen background [68]. Annealing our samples at 1100 K in $1.4 \cdot 10^{-6}$ mbar resulted in large homogeneous domains and a sufficiently good surface stoichiometry $Fe_{3-\delta}O_4$, with $\delta = 0.03$ as determined by fits of the Fe_3O_4 -XMCD to atomic multiplet calculations Fig. 7.3 (B). The sample for the NiO wedge was annealed at a slightly lower temperature (1065 K). Astonishingly, the fits yielded a surface with a decreased contribution of octahedral cations in favour of tetrahedral cations (negative γ in Fig. 7.3 (C)).

For the Fe_3O_4 (111) surface, preparation conditions had to be optimized in several steps to obtain the proper surface stoichiometry. Throughout the annealing runs, we applied an O_2 background pressure of $1.3 \cdot 10^{-6}$ mbar. Choosing the annealing temperature too high (1100 K) resulted in a mixed surface phase with triangular islands, (see Fig. 7.1). The surface is partly reduced and the islands have been confirmed to be of the FeO phase (see Fig. 7.2). Evaporating NiO on such a surface resulted in a noncontiguous NiO layer, which showed an island growth behaviour as well, possibly because surface irregularities disturbed the growth. PEEM images at the NiO L_2 edge confirm a NiO depletion on top of the FeO islands, as indicated by the lowered intensity in those areas (Fig. 7.1 (C-D)).

Finally, choosing a slightly lower annealing temperature 1000 K, no islands were observed anymore. The sample shows the typical "coathanger" quasidomain-pattern (see Fig. 7.1 (E)), which is typical for the low-anisotropy Fe_3O_4 (111)-

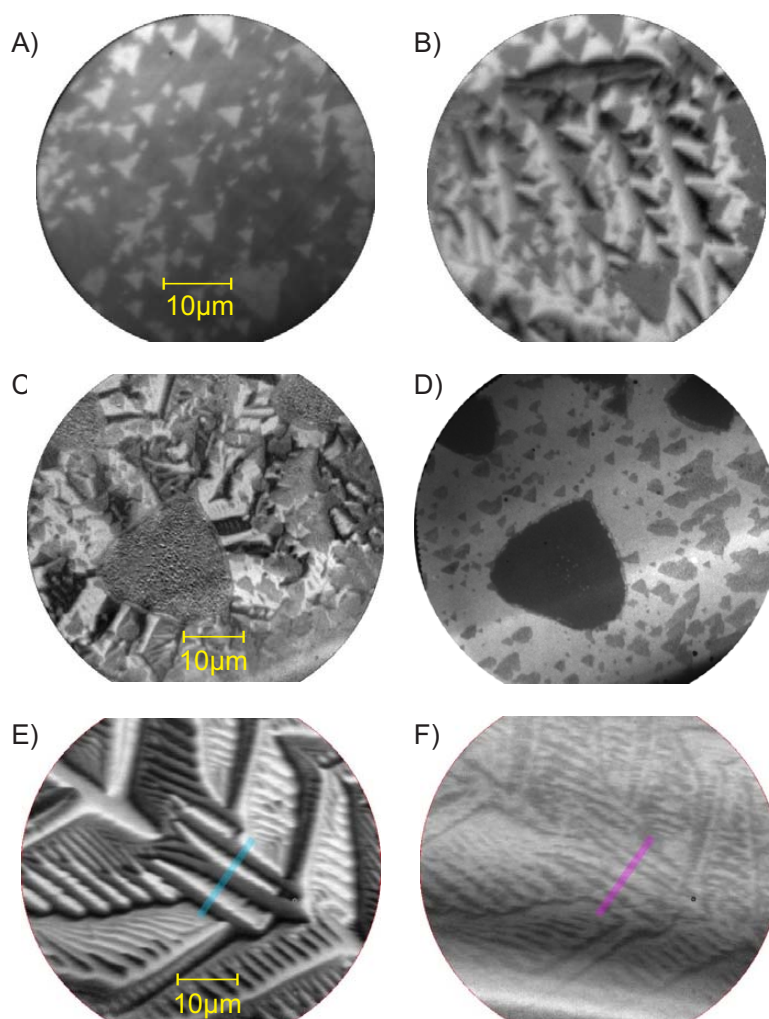


Figure 7.1.: (A) XAS contrast at the Fe edge of a freshly tempered Fe₃O₄ (111) crystal. Triangular islands can be seen, producing no XMCD contrast in image (B), which shows the Fe-XMCD contrast at 711 eV. The underlying domain pattern is partly correlated to the islands due to exchange coupling between the antiferromagnetic FeO islands and the Fe₃O₄ phase below. (C) Fe-XMCD contrast, now with a NiO layer evaporated on top. The NiO layer is noncontiguous, as can be seen in the PEEM image (D), which was taken at the NiO L₂ edge at 872 eV. The FeO islands are avoided by the NiO, as can be seen by the low intensity in these areas. (E) Annealing at only 1000 K yielded a homogeneous surface of Fe₃O₄-phase, which shows the typical quasidomain pattern of the (111) surface [177]. Evaporation of NiO yields a homogeneous film which couples well to the substrate, as can be seen in the NiO-XMLD image (F). Coloured bars show the spots for the lineprofiles discussed in section 7.3.3, page 101.

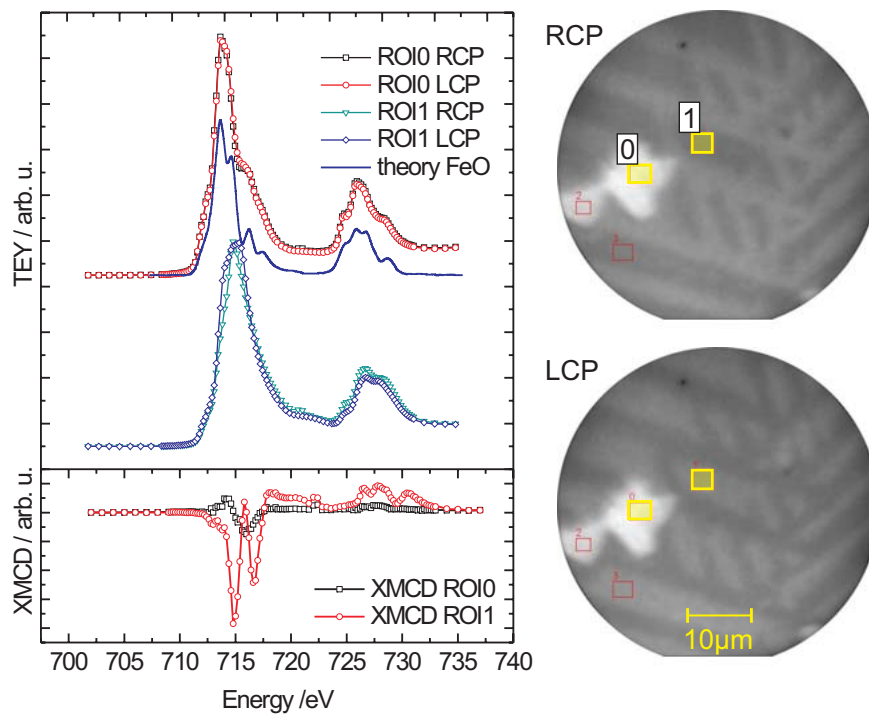


Figure 7.2.: If the annealing temperature is too high, FeO islands form on the Fe_3O_4 (111) surface. Yellow rectangles show the ROIs for the microspectra. Spectra taken inside one of the islands (ROI0) show a good accordance to theoretical calculations of $\text{Fe}_{\text{O}_h}^{2+}$ as in FeO [30]. The islands show only minimal circular dichroism, possibly due to exchange coupling to the substrate, whereas the remaining sample area (ROI1) is of Fe_3O_4 -type and showed the proper XMCD signal.

surface, as described in Ref. [177]. The final stoichiometry of the sample was nearly perfect (compare Fig. 7.3 (A)), but with an increased weight of the tetrahedral Fe^{3+} . Evaporating NiO onto this surface resulted in a contiguous layer, which shows homogeneous XMLD contrast in PEEM (Fig. 7.1 (F)).

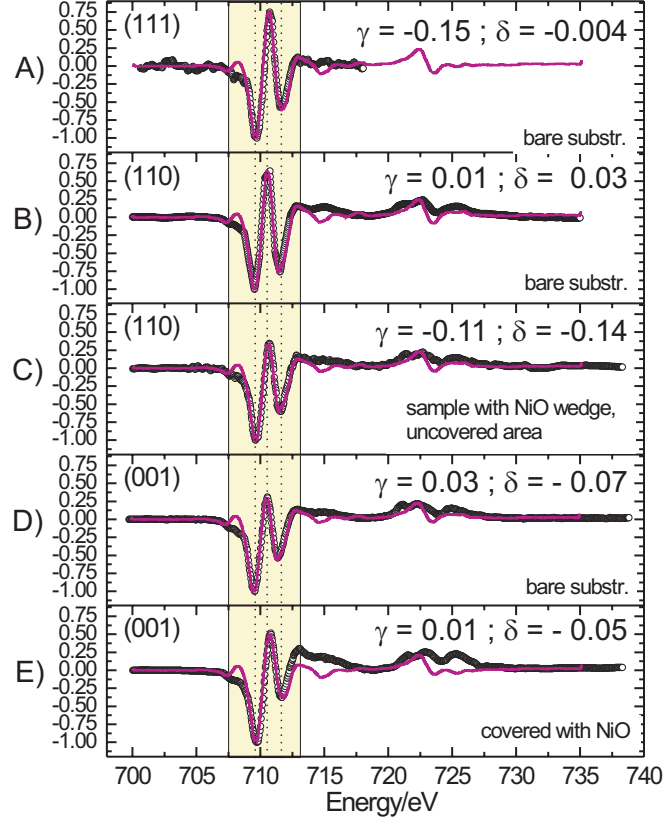


Figure 7.3.: Comparison of the stoichiometry for three different crystalline surfaces. The L_3 region of the experimental XMCD spectra (yellow background) has been fitted to the sum of the site-valency contributions calculated by atomic multiplet theory (see Sec. 6.2 on page 59 for details). The stoichiometry parameters have been derived according to the ionic model reported in Ref. [129]: $\text{Fe}_{\text{Td}(1-\gamma)}^{3+} \text{Fe}_{\text{Oh}(1+2\delta+\gamma)}^{3+} \text{Fe}_{\text{Oh}(1-3\delta)}^{2+} \text{vac.}_{\text{Oh}\delta} \text{O}_4$, where γ describes the transfer of 3+ cations from tetrahedral to octahedral sites and δ describes the amount of vacancies on octahedral sites and is a direct indicator for stoichiometry ($\delta = 0$).

For the (001) surface, a considerably lower annealing temperature was chosen, in accordance with the procedure given in Ref. [102], where a stoichiometric and well-ordered surface was obtained by annealing at 850 K. JORDAN *et al.* report the formation of a clean $\sqrt{2} \times \sqrt{2} R45^\circ$ -reconstructed (001) surface after annealing at 850 ± 20 K in $5 \cdot 10^{-6}$ mbar O_2 . The conditions chosen in the present experiment

were $T = 870$ K, and $p_{\text{O}_2} = 1.4 \cdot 10^{-6}$ mbar. Fits to atomic multiplet calculations yielded a negative $\delta = -0.07$, which indicates a surface with a slight excess of octahedral iron as compared to stoichiometric magnetite. This may be interpreted as a reduction of the sample to FeO. Since in Ref. [93], this only occurs for UHV annealing, a reduction is thought to be unlikely. Most likely, the sample is simply B-terminated, as reported under the given preparation conditions [93]. Since the probing depth is only $\approx 10 \text{ \AA}$ [50], the topmost layer contributes most to the XMCD signal, and the XMCD spectrum of a B-terminated sample will then tend to resemble FeO, due to the 1:1 stoichiometry of the surface layer.

Interestingly, the deposition of NiO did not induce substantial changes the magnetite's interface composition, as can be compared in Fig. 7.3 (D-E). Therefore, one can assume that the interface is indeed chemically inert. The (001) surface of magnetite shows a complicated quasidomain pattern, in analogy to the (111) surface, since no easy directions lie in the surface plane (see Fig. 7.4). Summarizing,

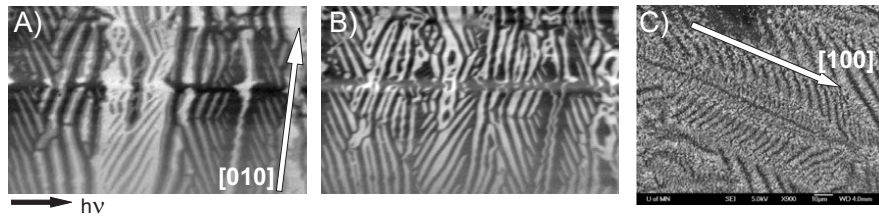


Figure 7.4.: Quasidomains at the magnetite (001) surface: A) Fe_3O_4 -XMCD contrast. B) NiO-XMLD s-pol. C) Bitter image of a magnetite (001) viewing plane taken from Ref. [25]. Since no bulk easy axes are in-plane, a complicated quasidomain pattern results, which contains "fir tree" structures as well as straight features running along $\langle 100 \rangle$ -directions, probably related to bulk domain walls.

the preparation yielded a surface stoichiometry close to magnetite in all surface orientations, but never the *perfect* phase. This is not astonishing, since even in case of a bulk truncation of the crystal – for example after cleavage – the topmost atomic layers may reconstruct and therefore assume a different phase. For the (001) surface of magnetite, a B-termination will even naturally produce a FeO surface layer. It should be emphasized that the type of termination influences the magnetic properties of the interface most drastically, whereas slight deviations from "stoichiometry" within a larger substrate volume may not have such a substantial influence. Particularly, the large deviations in the uncompensated magnetization of the NiO layer between the different orientations may be strongly related to interface termination and reconstruction (see Sec. 7.4.2).

7.2.2. NiO deposition by MBE

In general, systems like CoO/Fe₃O₄ [66, 65], NiO/Fe₃O₄ [16, 17] or Fe₃O₄/MgO [86] show good epitaxial growth due to the similar structure and low lattice mismatch, and have been successfully used to create highly-ordered magnetic multilayers. In HRTEM studies, RECNİK *et al.* verified that Fe₃O₄/NiO multilayers can be grown with atomically flat interfaces, if the temperature is kept below ≈ 573 K [121]. In addition, WANG *et al.* found by UPS/XPS that depositing NiO on top of Fe₃O₄ at moderate temperatures (< 573 K) resulted in an atomically sharp transition from the Fe₃O₄ to the NiO phase [166]. They point out that atomically sharp in this sense means that a monolayer-thick reconstruction of the interface to NiFe₂O₄ is likely due to structural similarity (inverse spinel phase), but cannot be discriminated by their technique. LAZAROV *et al.* applied HRTEM measurements and DFT calculations to demonstrate for the quite similar MgO(111)/Fe₃O₄ system, that even at a polar interface like (111), atomically sharp interfaces can be retained without substantial reconstruction or intermixing [86]. This finding is astonishing, since in a simple ionic model, one would expect that the interface reconstructs or mixes due to the strong dipolar forces acting on the ions. From the calculations it was concluded that the electrostatic mismatch due to interface polarity can be removed within the first few interface layers, obviously by strong electronic screening without the need of atom rearrangement. In particular, metallic interface states were found in the MgO gap, as well as strong Fe-O-Mg bonding across the interface, providing effective mechanisms for screening.

For our experiments, we deposited NiO layers by oxygen-assisted MBE immediately after substrate preparation and characterization onto the clean surface. As deposition parameters, we chose 10^{-6} mbar O₂-background pressure and temperatures slightly above room temperature (due to the residual heat load of the evaporator). After evaporation of the NiO layer, the system was heated briefly above the NiO NÉEL temperature (525 K) and then cooled down to room temperature within several minutes in order to "freeze" the substrate domain pattern into the AF. For the (110)-interface we monitored the growth of the adlayer by XAS on a NiO wedge and found sharp extrema for the magnetic XMCD signals at the Fe- and Ni-edges for a coverage of one monolayer [78]. From this it is concluded that the system grows with an atomically sharp interface, predominantly in a layer-by-layer fashion. Moreover, the short heating time of < 15 min for zero field cooling of the NiO obviously did not lead to interfacial intermixing. Also for the other two orientations, we conclude that we have sharp interfaces, since the uncompensated Ni magnetization is very small. If, for example, Ni cations were to diffuse into the substrate, this would result in a strong Ni-XMCD signal. In fact, the signal is only 10% the size obtained for the (110)-interface, hence we

conclude that intermixing is negligible and we have only about one reconstructed layer at the interface, which presumably has NiFe_2O_4 -structure. This result is particularly astonishing for the (111)-oriented sample, and we conclude that the screening mechanisms described by LAZAROV *et al.* may indeed lead to good growth characteristics in this case.

7.3. Experimental results

7.3.1. (110)-interface

The measurements at the (110)-interface have already been presented in the previous chapter and shall only briefly be summarized here: Evaluation of the magnetic dichroism yielded that the magnetic moments in the substrate are parallel to the in-plane easy-axes and the antiferromagnet couples collinearly to the substrate magnetization. At the interface, an enhanced total Fe- and Ni-moment was found, which is possibly in both cases is caused by the orbital part.

7.3.2. (001)-interface

The magnetic structure of Fe_3O_4 (001)/NiO was determined by angle dependent XMLD measurements at the SIM beamline SLS in Villigen. The possibility to rotate the linear polarization direction around the beam axis gives reliable results for the spin-axis orientation without the need of further assumptions. In fig. 7.5, the theoretical curves for XMLD and XMCD contrast are plotted for a hypothetical full in-plane rotation of the Fe_3O_4 net moment and the NiO spin axis in the collinear as well as 90° coupling situation. Two regions were chosen for contrast extraction, where the substrate spin-orientation approximately differs by 90° , one with the spin perpendicular to the in-plane beam projection (D1) and one parallel to it (D2) (compare fig. 7.5). Note that in XMCD contrast, this corresponds to an *intermediate* and maximum signal, respectively, as can be seen in fig. 7.6 (C). A comparison of the NiO-XMLD images in s-polarization (fig. 7.6) to the polar plots in fig. 7.5 yields a coarse estimate of the coupling angle: The scenario of perpendicular coupling is more realistic, because the NiO XMLD then produces almost maximum contrast for (D1) and minimum contrast for (D2) – in accordance with the PEEM data – whereas collinear coupling would yield the opposite.

Note that the XMLD contrast also exhibits a phase shift with respect to the XMCD, as can be seen in fig. 7.5. Whereas the XMCD is maximum along

the light propagation direction (or its in-plane projection), the maximum of the XMLD signal is shifted away by 14° from this direction. This is a consequence of the anisotropic nature of the XMLD, as will be explained in the following:

The angular dependence given in equation 2.38 yields an astonishing result: If the polarization is coplanar with a C_4 plane (i.e. the sample surface), the XMLD manifold $\mathfrak{M}_{\mathbf{E}}(\mathbf{S})$ includes a C_∞ -axis within the same plane (compare Fig. 2.10). If the polarization additionally points along a C_4 axis, the C_∞ -axis coincides with polarization direction. Rotating the polarization away from this axis by an angle ϕ within the (001)-plane results in a simple rotation of the XMLD manifold by $-\phi$, hence the in-plane XMLD anisotropy exhibits a phase shift of 2ϕ with respect to the polarization direction. Since in our case, with s-geometry, the polarization \mathbf{E} forms an angle of $+7^\circ$ with the C_4 axis [100], the maximum XMLD will occur for \mathbf{S} parallel to an axis deviating by -7° .

The anticyclic rotation of the polarization \mathbf{E} and the XMLD manifold $\mathfrak{M}_{\mathbf{E}}(\mathbf{S})$ also explains, why the XMLD has only half the period of the XMCD. Another important consequence is that the contrast levels for the two cases $\mathbf{E}||\mathbf{S}$ and $\mathbf{E} \perp \mathbf{S}$ are interchanged, when going from $\mathbf{S}||[110]$ to $\mathbf{S}||[100]$. This is why some of the findings in (001) oriented systems have to be reconsidered, if they were interpreted on the basis of the "isotropic" XMLD theory. It could easily happen that spin-flop coupling is mistaken for collinear coupling, as has already been pointed out by Arenholz *et al.* [9]. Therefore, it is absolutely necessary to apply the formalism of "anisotropic" XMLD for vectorial magnetometry in crystalline systems.

After definition of the regions of interest, angular scans of the light polarization from p - to s -geometry were performed. The corresponding contrast for Fe_3O_4 and NiO is shown in Fig. 7.6. Comparing the Fe_3O_4 and NiO XMLD, a contrary behaviour of the XMLD contrast in D1 and D2 is apparent. While D1 shows a weak angular variation for NiO, it changes strongly for Fe_3O_4 . For D2, the behaviour is opposite. From this one can already conclude on a different orientation of the two spin axes.

A more precise picture is finally gained from the explicit comparison to theory of anisotropic XMLD. For this purpose the theoretical MLD contrast produced by Eq. 2.38 was fitted to the experimental curves, taking the spin-directions of D1 and D2 gained from the XMCD as starting values and assuming either an *in-plane* spin-flop coupling or – for cross checking – a collinear arrangement. While for the collinear case the fit yielded a negative scaling parameter for the NiO MLD (which would contradict the atomic multiplet calculations) together with poor convergence, the parameter is positive for the spin-flop case and the fit converges well. The curves of the *relative* domain contrast D1/D2 show the

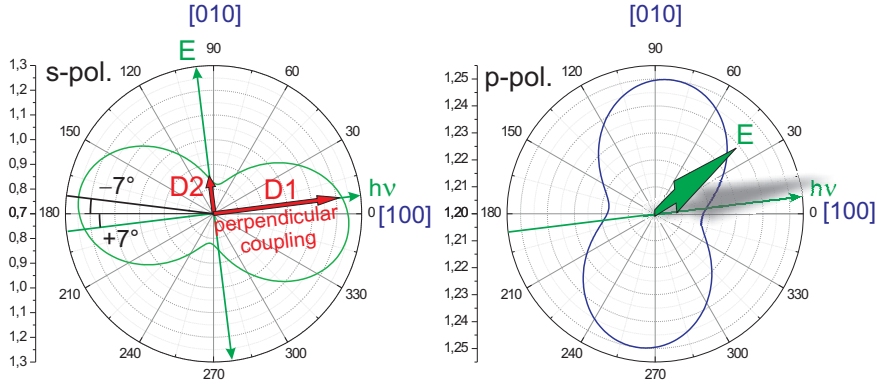


Figure 7.5.: XMLD anisotropy calculated for p- and s-geometry in our experiment. The test ROIs for the angular scans are labelled D1 and D2, respectively and are chosen as follows: In D1, the magnetization in the substrate is perpendicular to the in-plane projection of the light propagation direction, while in D2, it is parallel. If the NiO layer couples spin-flop, the spin-axis-directions then point into the directions given by the red arrows. Region D1 then produces almost maximum XMLD contrast, while region D2 shows nearly minimal signal. Note that for collinear coupling, the labels D1 and D2 would simply be reversed. Since the in-plane light projection forms an angle of 7° with the [100]-axis, the maximum of the XMLD anisotropy deviates by -7° from that direction. Hence, the maxima of the XMLD are shifted by 14° with respect to the extrema of the XMCD. Due to the anisotropic nature of the XMLD, XMCD contrast and XMLD contrast are not necessarily in phase!!

good fit quality, since all correlated noise present in the separate measurements of D1 and D2 is removed¹. Together with the coupling angles derived from the fits ($\alpha_{D1} = 58 \pm 10^\circ$ and $\alpha_{D2} = 103 \pm 10^\circ$), one can directly conclude that collinear coupling can be ruled out and a spin-flop state is realized in the FM/AF system! Furthermore, the results show that the NiO spins are *not* oriented out-of-plane, as could be expected from the deformation of the NiO-layer due to the tensile in-plane strain [43, 60], but are *in-plane*, very likely due to the interfacial exchange coupling to the substrate magnetization, which is forced to be in-plane due to shape anisotropy. Our results at the (001)-interface are in accordance with the findings for Fe_3O_4 (001)/NiO-superlattices, where spin-flop coupling has been found as well [16, 17].

¹The scatter of the data points is thus due to (nonmagnetic) intensity fluctuations possibly caused by imperfect undulator control. A normalization to the primary intensity I_0 measured at the refocussing mirror could not eliminate the scatter.

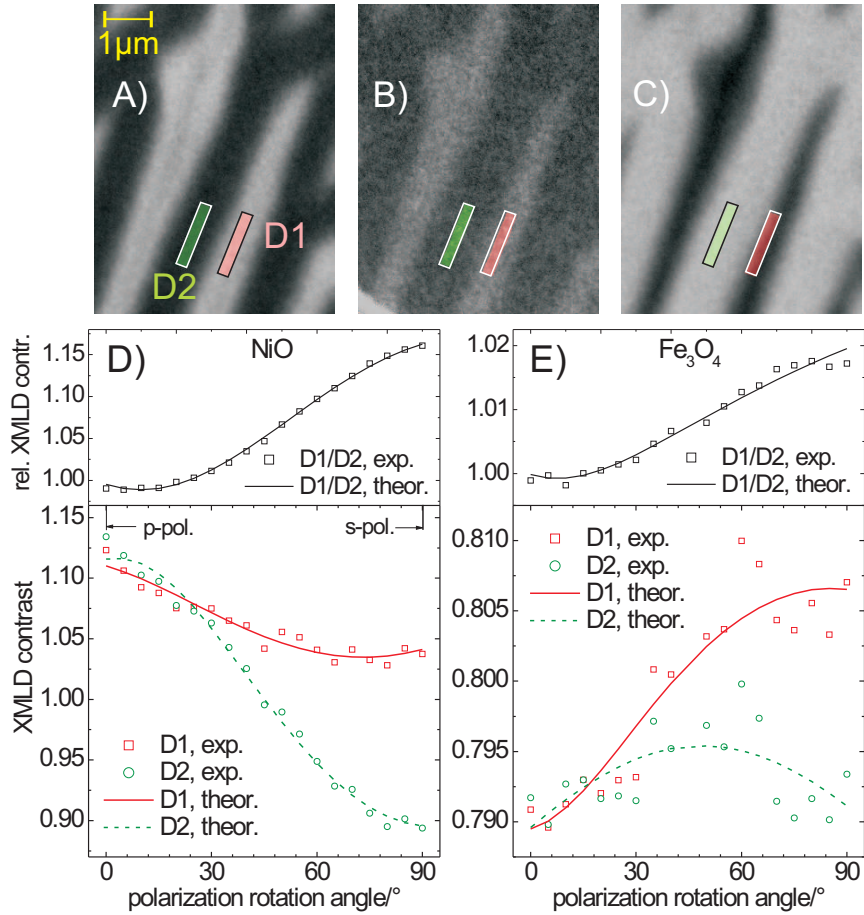


Figure 7.6.: Angular polarization scans from a 43 Å (21ML) NiO layer on Fe₃O₄ (001). In the PEEM images, two regions for contrast extraction are shown (D1, D2), which exhibit extremal contrast values in s-polarization. (A) NiO-XMLD PEEM image, (B) Fe₃O₄-XMLD PEEM image (C) Fe₃O₄-XMCD. Angular scans: (D) NiO XMLD (E) Fe₃O₄-XMLD. From the fits (solid and dashed lines), the tendency for spin-flop coupling can be derived (see text).

7.3.3. (111)-interface

Measurements for this interface have been performed at the BESSY beamline UE 56/1 SGM, where no free rotation of the polarization was possible. Fortunately, the intrinsic domain pattern of the Fe_3O_4 (111)-surface offers a convenient way to work around this limitation. The quasidomain pattern at the (111) surface consists of lamellar structures, in which a quasi-continuous rotation of the magnetization in the film plane takes place². Due to the presence of all possible in-plane magnetization directions in *one* PEEM image, the data can be treated as a *quasi*-rotation experiment, and turning the sample or polarization becomes obsolete. XMCD line profiles perpendicular to the lamellae record a full *in-plane* turn of the substrate magnetization, and the corresponding XMLD profiles show the related behaviour of the spin-axis in NiO. What remains to be done is to compare the calculated NiO-XMLD to the experimental profile. This has been performed in Fig. 7.7. On the left hand side the profiles for NiO-XMLD (p- and s-geometry) as well as Fe_3O_4 -XMCD are shown. It is directly apparent that the minima of the s-polarized XMLD coincide in most of the cases with the extrema of the XMCD, whereas the maxima tend to coincide with the zero-crossings of the XMCD. This situation corresponds to the simulation of collinear coupling shown to the right. Perpendicular coupling would just result in the opposite behaviour. Note that the p-polarized contrast has a slight phase shift with respect to the s-polarized data – as stated earlier – because \mathbf{E} points along crystalline non-symmetry directions. The tendency of p-contrast to have maxima near the minima of the s-contrast can also be observed experimentally, however, the data quality is worse than that of the measurement for s-contrast. To conclude, the (111)-interface in the $\text{Fe}_3\text{O}_4/\text{NiO}$ system leads to collinear coupling, just as the (110)- and contrary to the (001)-interface.

7.3.4. Amount of uncompensated magnetization in the three orientations

After finding out, that the interface orientation can make a difference in the coupling scheme, it is natural to presume that there should be some differences in the amount of uncompensated magnetization at the interface, too. To corroborate this hypothesis, the NiO-XMCD signal is evaluated for the three orientations by scaling it to the respective size of the Fe_3O_4 -XMCD. In this way, we get scaling factors that vary with interface orientation, which are shown in Fig. 7.8.

²Since the anisotropy in the (111)-plane is very low, there are practically no regions of homogeneous magnetization, and the sample consists only of "walls".

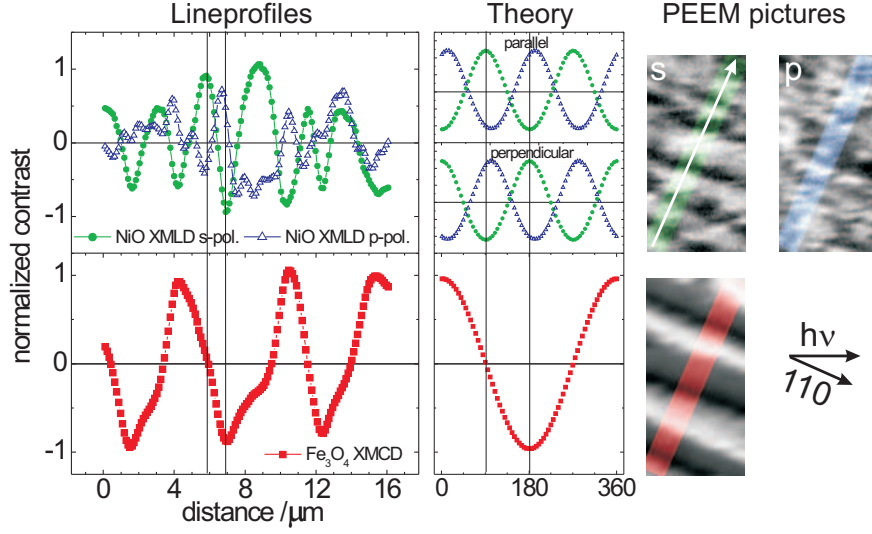


Figure 7.7.: Fe₃O₄ (111)/NiO[37 Å]: Left hand side: Experimental line profiles. Center: theoretical profiles calculated for a full in-plane rotation of \mathbf{S} for both collinear and perpendicular coupling. Right: Corresponding PEEM images. Laue measurements confirm that the stripe pattern is parallel to a $\langle 110 \rangle$ -direction.

Since the (110) interface exhibits the largest uncompensated magnetization in the AF, we use it as a reference, assuming that the Ni spins at the (110) interface are aligned fully parallel to the substrate magnetization – for simplicity. The second simplifying assumption is that only one interfacial monolayer will contribute to the NiO-XMCD. Although in reality the proximity zone may spread over 2-3 monolayers, the integrated signal will roughly be equivalent to one monolayer, since the effects decay quickly with distance from the interface. Hence, our simplification is justified. Last but not least, the signals have to be corrected for the slightly different film thicknesses by taking into account the electron escape depth λ_e , and the normal x-ray absorption length $\lambda'_x = \lambda_x \sin(\theta)$, where θ is the incidence angle to the plane (16°). The NiO XMCD signal from a buried region ranging from the depth τ to $\tau - d_l$ is proportional to

$$\begin{aligned}
 I_{\text{XMCD, NiO}} &\propto \frac{\int_0^{d_l} e^{-\mu_{\text{eff}}(\tau-z)} dz}{\int_0^{\tau-d_l} e^{-\mu_{\text{eff}}z} dz} \\
 &= \frac{e^{-\mu_{\text{eff}}\tau} (1 - e^{+\mu_{\text{eff}}d_l})}{1 - e^{-\mu_{\text{eff}}(\tau-d_l)}} , \\
 \mu_{\text{eff}} &= \frac{\lambda_e + \lambda'_x}{\lambda_e \lambda'_x} ,
 \end{aligned} \tag{7.1}$$

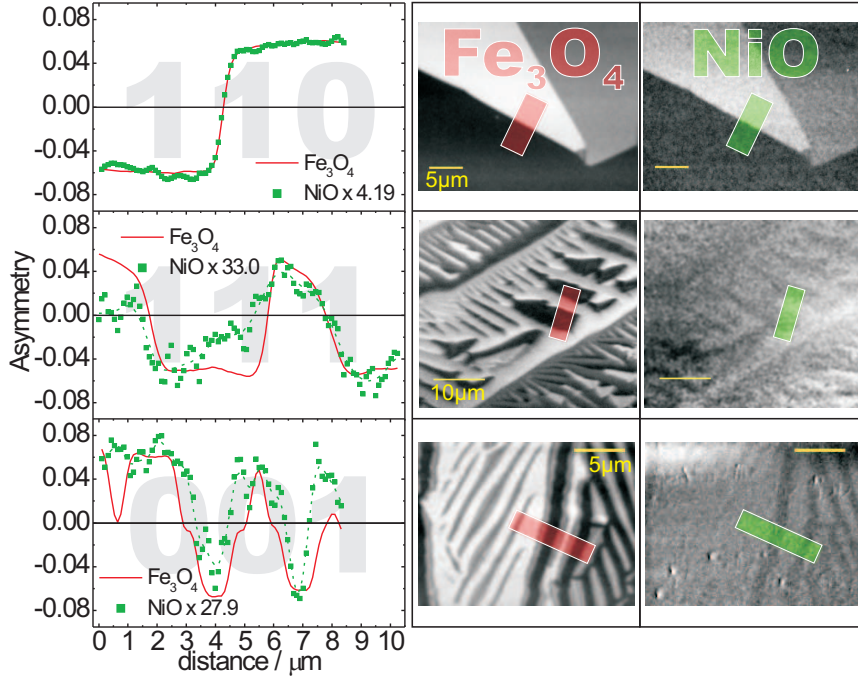


Figure 7.8.: Comparison of the amount of uncompensated magnetization at the interface for the three different orientations (001),(110),and (111). For comparison, the Ni-XMCD has always been scaled to match the size of the Fe_3O_4 -XMCD, which was assumed not to depend on the interface orientation.

while the escaping electrons from Fe_3O_4 have to travel through the NiO layer of thickness τ and are reduced in number by a factor $\exp\{-\mu_{\text{eff}}\tau\}$. Thus, relating the NiO contrast to the Fe_3O_4 contrast will result in an escape-absorption dependence like

$$\gamma = \frac{I_{\text{XMCD,Fe}_3\text{O}_4}}{I_{\text{XMCD,NiO}}} \propto -\frac{(1 - e^{+\mu_{\text{eff}}d_i})}{1 - e^{-\mu_{\text{eff}}(\tau-d_i)}} \quad (7.2)$$

Correcting with $1/\gamma$ from Eq. 7.2, the scaling values of the (001) and (111) interface can now be related to the results for (110), yielding the amount of uncompensated magnetization in %³. For the (111) interface, we obtain $13.8 \pm 7\%$, while for the (001) interface the value is $9.8 \pm 3\%$. Since spin-flop coupling occurs at the (001) interface, we can also assign a canting angle of the sublattice spins towards the substrate magnetization direction, which is only about $5.6 \pm 2^\circ$

³As electron escape depth in NiO, $\lambda_e = 30 \text{ \AA}$ was assumed [122]. The x-ray absorption length was determined to be 555 \AA at the energy of 855.8 eV .

– a typical value for spin-flop systems as found by KOON [75]. Of course, this is only an upper limit, since it is always possible, that magnetic defects play a role, and not canting alone is responsible for the uncompensated magnetization. Those defects can be located at step edges or inside antiphase boundaries in the antiferromagnet, usually have a lower anisotropy and can align more freely with the substrate magnetization.

7.4. Discussion of the results

7.4.1. Magnetoelastic influence on the coupling type

NiO has a lattice mismatch of +0.5% as compared to Fe_3O_4 , which means that a NiO layer coupled to magnetite is expanded in the interface plane and compressed along the surface normal by the epitaxial strain. Choosing different interface orientations, the directions of the strain are varied with respect to the crystal lattice, and thus different magnetoelastic effects should occur. To discuss those, we estimate the layer distortions along the possible stacking directions (T-domains [124, 172, 174]) in NiO by elastic continuum theory (see for example Ref. [127]). For the (111)-interface, the NiO-layer is compressed along the surface normal [111] by about 0.24%. Since the natural exchange-striction in NiO also leads to a compression of 0.15% along the $\langle 111 \rangle$ -type stacking vectors [140], NiO should favour T-domains with a stacking vector normal to the surface [171]. Consequently, the NiO easy-plane will be coplanar with the (111)-interface and a fairly low in-plane anisotropy should result. KUROSAWA *et al.* report an extremely low value of only 29.5 Jm^{-3} for well-annealed single crystals [126]. Our experimental situation, however, might be more compatible with a layer coupled to a single crystal, as for example reported by LAI *et al.* for NiO(111)/NiFe [85]. There, a considerably higher value of 1360 Jm^{-3} has been reported for the NiO anisotropy within the (111)-plane, which might be more realistic due to the interaction with the coupled layer. LAI *et al.* found that the tensile epitaxial strain by the Permalloy orients the Ni surface moments in-plane, which is quite similar to our situation.

It is also important to note that the anisotropy of magnetite within the (111)-plane is only about 302 Jm^{-3} and thus comparable to the value in NiO [177], or even lower. Thus, it is possible that the $\text{Fe}_3\text{O}_4/\text{NiO}$ interface is topographically compensated, partly compensating the topmost magnetite layer as well: Since locally ferromagnetic sheets of NiO couple parallel to the net moment of Fe_3O_4 , the interface is microscopically (on dimensions of the lattice parameter) uncompensated with mesoscopic antiphase boundaries due to interface terraces (with

dimensions of the order of tens to hundreds of lattice constants). As a consequence, a microscopic parallel coupling should result, but with macroscopically compensated magnetization due to the mesoscopic antiphase domains. Of course, besides those frozen spins there is another class of magnetic moments with a low anisotropy [120, 111]: Interfacial spins inside the antiphase boundaries are able to rotate more freely due to their frustrated coupling environment, and may align parallel to the net magnetization in the substrate. The same argumentation holds for defect spins. In this way, a small uncompensated magnetization in NiO is retained.

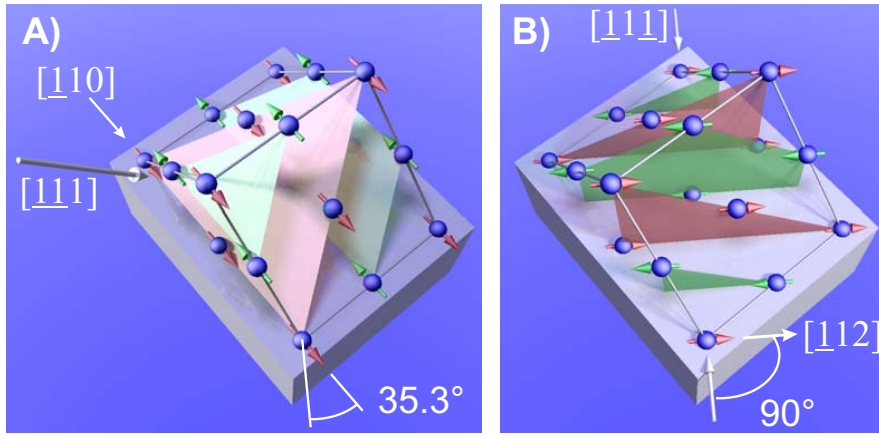


Figure 7.9.: Magnetoelastic situation at the (110)-interface. A) The tensile in-plane strain leads to an out-of-plane compression, which favours stacking along out-of-plane $\langle 111 \rangle$ -directions. The in-plane easy axis in this case is along $[110]$. B) If the stacking were to occur in-plane along the magnetite easy axis, the easy planes would be perpendicular to that axis, leading to spin-flop coupling. Since, however, the in-plane strain is tensile and moreover the magnetostriction in magnetite is positive along its easy axis, this situation is highly unlikely.

In the (110) interface, in-plane expansion of 0.5% makes the in-plane $[111]$ and $[1\bar{1}1]$ stacking directions unfavourable. Stacking along those would lead to spin-flop coupling, since the easy planes of NiO would then be perpendicular to the interface plane, leaving as only intersections the in-plane $[\pm 1 \mp 12]$ easy directions. Consequently, spin-flop coupling is unfavourable. The out-of-plane $[11 \pm 1]$ directions, however, are favoured by the out-of-plane compression (for example $1.25 \cdot 10^{-4}$ along $[111]$). Thus, the NiO stacking will take place along those directions, and the NiO easy-planes form an angle of 35.27° with the interface. The intersection axis is then $[110]$, which forms a smaller angle with the $[\pm 1 \mp 11]$ axes than with $[\pm 1 \mp 12]$. Consequently, the coupling of NiO will be basically collinear to Fe_3O_4 , but with an admixture of a uniaxial anisotropy along $[110]$. This situation is comparable to noncollinear exchange bias, where the easy axes of the F

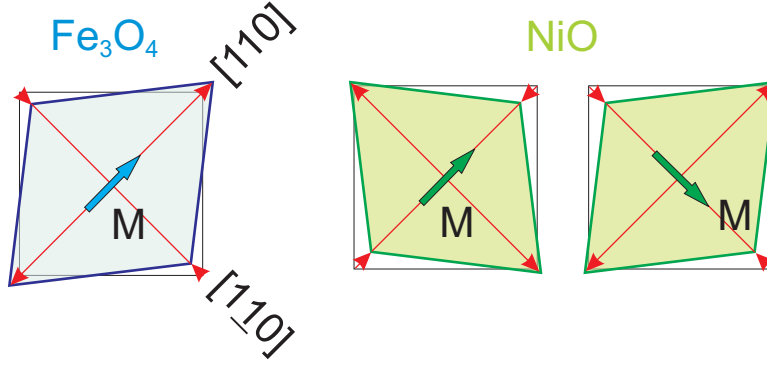


Figure 7.10.: Magnetoelastic deformations of NiO and magnetite within the (001)-interface plane (situation exaggerated by a factor $2 \cdot 10^3$). Using the magnetostriction constants of NiO [114] and Fe_3O_4 [73] one obtains that the deformations in both materials match only for spin-flop coupling.

and AF differ [115]. While in our as-grown samples, we could find no significant deviation from the $[\pm 1 \mp 11]$ easy directions in the substrate, annealing our layers induces a sizeable deviation of the easy directions towards $[\underline{1}10]$, showing that our assumption is reasonable [79].

Finally, we will discuss the situation at the (001)-interface, where all $\langle 111 \rangle$ -stacking directions are affected equally by the lattice strain (expansion by about 0.2%, as calculated from the relations given in the Appendix A.1). Thus, weaker magnetoelastic effects by origins other than lattice strain can come into play, for example, *magnetostriction*. From our data we know that spin-flop coupling is realized, in frappant contrast to the other interfaces. Considering, that the easy directions at the Fe_3O_4 (001)-surface are in-plane along $\langle 110 \rangle$ directions, we can estimate the magnetoelastic deformation at the interface from the magnetostriction constants of Fe_3O_4 [73], NiFe_2O_4 [145] and NiO [114]. Since the easy directions of bulk magnetite are $\langle 111 \rangle$, the in-plane projections in the surface domains will be along $\langle 110 \rangle$. In table 7.1 we summarize the distortions according to Eq. A.7 along the $[110]$ substrate magnetization direction and perpendicular to it ($[\underline{1}10]$) for the two cases of collinear and spin-flop coupling of NiO. As is directly apparent, the signs of the distortions in NiO along $[110]$ and $[-110]$ for spin-flop coupling match with the respective signs of magnetite, while the signs for collinear coupling are inversed. Thus, spin-flop coupling of NiO is strain-compatible with the magnetoelastic deformation of Fe_3O_4 , while collinear coupling is not.

Although the strain due to magnetostriction is small (of the order of 10^{-5}), we calculate a considerable energy gain of $\Delta E_{MS} \approx 3560 \text{ Jm}^{-3}$ of the spin-flop state as compared to the collinear state (for details, see appendix A.1.2). For this estimation we assumed that the NiO layer simply follows the magnetostrictive

strain of the substrate. We first calculated the magnetostrictive deformation of magnetite for $\mathbf{S}||[110]$ by Eq. A.7. Then we used the magnetostriction constants for NiO from Ref. [114] together with the strain tensor induced by the substrate in order to calculate the magnetoelastic energy from Eq. A.8 (see, for example Ref. [127]). Comparing the values for $\mathbf{S}||[110]$ (collinear) and $\mathbf{S}||[\underline{1}10]$ (spin-flop), the magnetoelastic energy gain by spin-flop coupling turns out to be of the same order of magnitude as other anisotropies in the sample (for comparison: see the anisotropy in the (111)-plane of NiO and magnetite as given earlier in this section). To check the possibility, that this energy overcomes exchange coupling, we estimate the total magnetoelastic energy in our film in relation to the interfacial exchange energy at the Fe_3O_4 (001)/NiO-interface. Taking the strongest Ni-Fe exchange constant in NFO, namely the 124° superexchange of $J_{AB} = -25k_B$ [71], we can estimate the interfacial exchange energy as $E_{\text{ex.}} \approx 8 \cdot 10^{-3} \text{ Jm}^{-2}$ in case of completely parallel coupling (*uncompensated* interface). This value is well within the parameter range for NiO(100) as reported in Ref. [107]. If the interface is partially compensated, however, this value is further reduced, and in the extreme case of full compensation it is smaller by approximately $\sin(\gamma)$, with γ being the canting angle. Since this angle is low ($5\text{-}10^\circ$, compare our results), the interfacial exchange energy can be as low as 10^{-4} Jm^{-2} . If we now estimate the total magnetoelastic energy in our thin film (thickness 43 \AA), we arrive at an energy of $\approx 1.6 \cdot 10^{-5} \text{ Jm}^{-2}$, which is one to two orders of magnitude lower than the estimated exchange energy. It is possible, however, that the exchange energy at the interface is further lowered, for example, if instead of superexchange, the weaker and ferromagnetic 90° -double exchange is the dominating mechanism. Another reason is that both Fe_3O_4 and NiFe_2O_4 are *ferrimagnetic*, i.e. it is possible that antiferromagnetic superexchange and ferromagnetic double-exchange partly compensate each other at the interface, depending on the termination/reconstruction. Thus, both the magnetoelastic energy and the interfacial exchange energy can indeed be of the same order. It should further be pointed out, that – since the magnetoelastic strains are long range – the total magnetoelastic energy gain increases with the *volume*, i.e. the layer thickness, while the interfacial exchange energy is *constant*. Hence, it is reasonable, that at a certain thickness the magnetoelastic energy will overcome the interfacial exchange energy. This means that there should be a thickness threshold for a spin-reorientation in the AF, if exchange and magnetoelasticity favour different coupling geometries.

Spin reorientation transitions observed in other studies [44, 76], especially for Fe(001)/NiO [44] can possibly be interpreted in this way, too. FINAZZI *et al.* observed a switching of the spin-axis orientation from spin-flop to collinear in Fe(001)/NiO($R45^\circ$) above a NiO thickness of about 20 \AA , but interpreted their results exclusively by an increase of defects with film thickness. The reorientation, however, could also be explained by strain relaxation effects: At low thicknesses,

material	$[110] \times 10^{-5}$	$[\bar{1}10] \times 10^{-5}$
Fe_3O_4 ($\mathbf{S} [110]$)	+5.5	-6.5
NiFe_2O_4 ($\mathbf{S} [110]$)	-2.8	+0.5
NiO ($\mathbf{S} [110]$, collinear)	-9.4	+0.2
NiO ($\mathbf{S} [\bar{1}10]$, spin-flop)	+0.2	-9.4

Table 7.1.: Magnetoelastic distortions in the Fe_3O_4 (001)/NiO system.

strain leads to spin-flop coupling . Note that the situation is quite similar to ours, as the magnetostriction in bcc-iron is positive along the iron $[100]$ axis [7], which is the $[110]$ -axis in NiO. Consequently, the NiO layer is expanded along the substrate magnetization direction, just as in Fe_3O_4 (001)/NiO. If now at some higher thickness strain relaxation occurs, the spin-axis orientation will switch back to collinear arrangement, for instance, in case that some uncompensated magnetization is mediated via defects (see results of Finazzi *et al.* [44]). We further mention, that the hypothesis of strain relaxation effects has also been supported by KRISHNAKUMAR *et al.* for Ag(001)/NiO/MgO systems [76]. We thus conclude that magnetoelastic effects can indeed lead to spin-flop coupling at the (001)-interface, provided that the magnetoelastic energy gain dominates over interfacial exchange coupling. Finally, we note that for NFO coupled collinearly to magnetite, the situation would be the same as for NiO, so spin-flop coupling could result even for a NFO reconstructed zone at the interface.

Other influences

In addition to magnetoelastic effects, one can speculate at least for the (110)-interface about a third influencing factor – the substrate surface and interface reconstruction. JANSEN *et al.* found a one-dimensional reconstruction of the magnetite (110) surface into rows and grooves running along $[\bar{1}10]$ [67], as mentioned earlier in Sec. 7.2. Since the (110)-oriented samples for this thesis were treated in a similar way, this opens the interesting possibility that – in case the reconstruction persists upon deposition of another oxide – the one-dimensional structure might introduce a uniaxial anisotropy along $[\bar{1}10]$. As will be shown in Chpt. 8, indeed such a uniaxial contribution is found upon annealing of a Fe_3O_4 (110)/NiO-sample (see Sec. 8.2). Thus, actually two possible sources for this effect exist: interface reconstruction and magnetoelastic coupling.

7.4.2. Amount of uncompensated magnetization

While the (111) and (001) interfaces yield almost the same low value for the uncompensated magnetization in NiO, the (110) interface shows a considerably higher value. There can be several reasons for this behaviour. First, the (110) interface is the only one, which has easy axes of the substrate lying in the plane. This means, that the in-plane anisotropy is larger than for the other orientations, stabilizing the Ni interface moments, which are exchange coupled to the substrate. Second, interfacial bonding may affect the stability of the uncompensated magnetization, too. In the (110) interface, the bonding anisotropy is the largest one among the three interfaces, since the rotation symmetry about the surface normal is only C_2 , while in (111) it is C_3 and C_4 for (001). Furthermore, while in the (110) interface, two bonds connect a Ni atom to the underlying ferrimagnet at an angle of 45° to the plane, at the (001) interface, there's only one bond oriented perpendicular to the surface. So one may expect the exchange coupling and thus the amount of uncompensated magnetization to be lower in the (001)-orientation than for the (110) case. In the (111) interface, there should be three bonds with out-of-plane components, so one might expect the induced moment to be stronger than in the other two cases. However, as discussed in section 7.4.1, the stacking is out-of-plane in NiO, leading to a topographic antiphase domain pattern in NiO, with a macroscopic compensation of the interface magnetization. The residual Ni-XMCD might be caused by frustrated spins inside the antiphase boundaries or defect spins. Additionally, the in-plane anisotropy of NiO(111) is very low.

Last but not least, the third influencing factor is a possible interface reconstruction after deposition of the antiferromagnet. While the data for the (110) interface allow conclusions about the interfacial phase and thus its structure, this is not possible for the other two interfaces due to the lack of thickness dependent measurements. It can thus not be finally excluded that the absence of an interfacial NiFe_2O_4 phase in the (001) and (111) case is responsible for the drastically reduced Ni-XMCD. It remains to note, that in analogy to the previous section one can speculate about the (110) interface having the largest uncompensated Ni-magnetization due to the one-dimensional Fe_3O_4 surface reconstruction reported in Ref. [67].

7.5. Summary and Conclusion

Summarizing, the influence of the crystalline orientation of the FIM/AF interface on the magnetic proximity effect has been investigated for the three low index

orientations (001), (110) and (111). Exploiting XMCD to map the substrate magnetization as well as "anisotropic" XMLD to extract the NiO spin-axis orientation, we found collinear coupling between the FIM and the AF for the (111) and the (110) interface, while the (001)-interface exhibits spin-flop coupling. In all three orientations, we observed an uncompensated magnetization in the AF near the interface by Ni-XMCD. Comparison of the size of that magnetization yields the largest value for the (110)-interface, while the (111) and (001)-interfaces exhibit only 10% of that value. The coupling type can be explained by a strain-induced AF stacking asymmetry in the NiO AF domain pattern. In the (111)- and (110)-orientations, *out-of-plane* stacking leads to collinear coupling, while in the (001) orientation, the epitaxial strain does not prefer any particular stacking vector. In this case, magnetostrictive deformations induced by the magnetite substrate would favour spin-flop coupling, while the exchange coupling prefers collinear coupling. A weak interfacial exchange coupling in this system may thus lead to spin-flop coupling via magnetoelastic effects.

8. Tailoring antiferromagnetic domain walls and anisotropy

8.1. Motivation

In the previous chapter we have investigated the influence of the interface orientation on the magnetic structure at the interface. In this chapter, we will revisit the (110) oriented sample. This time, however, the sample is not in its as-grown state any more. It was already mentioned in the previous chapters, that the magnetic properties of the sample have been altered during temperature-dependent measurements, namely by the extended time at elevated temperatures above the NÉEL temperature of the NiO layer (483 K) (see Sec. 6.4). We observed, that between two temperature-dependent measurements, which *de-facto* also acted as an annealing procedure, the blocking temperature of the sample had changed. In fact, this parasitary effect can never be avoided, but in this case allowed some interesting insights into the interplay of anisotropies in a coupled layer system.

The present chapter is thus dedicated to the magnetic structure of the sample that formed after the first temperature treatment. The particular focus lies on two main aspects: (i) the "peculiar" anisotropy that developed *after* the annealing and (ii) the constrained magnetic domain walls in the coupled antiferromagnetic NiO layer.

Addressing point (i), it will be shown that the new anisotropy appearing in the sample can be understood by an interplay between the bulk anisotropies of the constituents, the magnetoelastic interaction between the two and the interfacial exchange anisotropy, which to a large extent may also be influenced by the particular interface reconstruction.

Aspect (ii), namely antiferromagnetic domain walls, is a subject of great interest by itself, because it has rarely been investigated (due to a shortage of suitable techniques). Many studies deal with the AF domain state indirectly, making use of integrating techniques like neutron and x-ray diffraction [66, 65, 16, 17, 40]. However, in this way, only information about the average domain-size can

be obtained, and the detailed microstructure of the separating walls cannot be studied. Few microscopy studies exist, which are focussed on the wall-structure, among them some STM studies in iron monolayers [15] and PEEM studies of NiO crystal surfaces [167, 80]. Besides those works, antiferromagnetic domains have been studied almost exclusively in bulk crystals of NiO, where they are determined by the interplay between crystal shape, stress minimization and internal defects [171, 173, 172, 147, 62, 52]. In our case, however, the AF domain topology is dictated by the exchange coupling to the substrate, although the wall-orientations are the same as in the bulk due to the perfectly registered epitaxial growth of NiO and magnetite. Besides exchange, magnetostriction of the substrate, which is transferred to the AF layer, may have an effect on the magnetic order inside the AF layer, too. The ability to induce domain walls in our NiO layer quasi at will by means of exchange coupling to a ferromagnetic substrate opens up unprecedented possibilities for the detailed investigation of their microstructure. Since the wall-planes are identical to bulk NiO, the results may be partly transferable to the bulk-situation.

In the following, we will now discuss the measurement and evaluation procedure. All information about magnetic anisotropies and the structure of domain walls in this chapter can be gained from the fitting of domain wall profiles in XMCD and XMLD contrast to theoretical calculations using the angular relations in Eqns. 1.3, 1.14 and Eq. 2.38.

In Fig. 8.3 the PEEM images of the Fe_3O_4 -XMCD and the NiO-XMLD are shown. Clearly, the Fe_3O_4 domain pattern is imprinted into the thin NiO layer by the interfacial exchange interaction. Consequently, the domain state in the AF induces constrained antiferromagnetic domain walls, which follow the wall orientations in magnetite and exhibit a rotation of the NiO spin system from one domain to another. These walls are different from the ordinary type of walls, which would form in a bulk NiO crystal due to magnetoelastic effects [167]. Since the condition of strain compatibility plays only a minor role in the coupled thin film of NiO, the walls expected in this case are dominated by the interfacial exchange interaction and can exhibit a completely different magnetic structure. The physics of the antiferromagnetic sublattice structure inside such walls is new and has rarely been investigated up to date – in contrast to ferromagnetic domain walls, which are well understood by theory and micromagnetic simulations.

The mode of rotation as well as the spin-axis orientations inside the domains can be extracted by exploiting the anisotropic XMLD, which depends on the orientation of the polarization and the spin-axis with respect to the crystal lattice [82, 83, 32, 8, 9]. Since the site symmetry of Ni^{2+} in NiO is cubic, only two fundamental spectra of an O_h NiO_6 cluster are needed to construct the NiO XAS spectra for arbitrary polarization and spin orientation [8]. Those are gained from

atomic multiplet calculations using the XTLS 8.0 code (see for example [60]). The angular dependence of the XMLD is a direct consequence of the site symmetry at the excited atom, which in a solid is linked to the crystal symmetry. Since NiO has only one type of magnetic cation (Ni^{2+} in O_h symmetry), the two fundamental spectra $I_{\text{perp}} = -\text{Im}\{\epsilon_{\perp}\}$ and $I_{\text{par}} = -\text{Im}\{\epsilon_{\parallel}\}$ are naturally gained when the light polarization \mathbf{E} and the spin vector \mathbf{S} point along high symmetry C_4 axes, ϵ_{\parallel} for $\mathbf{E} \parallel \mathbf{S} \parallel \mathbf{z}$ and ϵ_{\perp} for $\mathbf{x} \parallel \mathbf{E} \perp \mathbf{S} \parallel \mathbf{z}$. The spectra for arbitrary orientations of \mathbf{S} and \mathbf{E} , are then obtained by Eq. 2.38. Experimentally, the intensity ratio R of the NiO L_2 double peak was used to generate the XMLD PEEM contrast, and was then fitted to the respective parameter gained from the calculations.

For Fe_3O_4 , it is not straightforward to understand why there is the same angular dependence of the XMLD. Clearly, the electronic configuration and site symmetry in Fe_3O_4 are more complex than for NiO (magnetite possesses Fe cations O_h d^6 , d^5 and T_d d^5). Although no calculations for Fe_3O_4 have been performed, fitting the angular dependence obtained from NiO with a negative sign, however, resulted in astonishingly good matching. Although the site symmetry of the T_d cations is lower than cubic, a glimpse at the magnetite's inverse spinel structure shows that in the unit cell, all T_d sites must add up to cubic symmetry as well. Thus, finally the anisotropic XMLD in a solid is linked to the crystalline symmetry. Note that similar results have also been obtained experimentally by ARENHOLZ *et al.* for NiFe_2O_4 and Fe_3O_4 [8, 9]. It should be noted, however, that for a general compound, the relation in Eq. 2.38 is not necessarily correct. In fact, for NiO and magnetite it is *correct only to a good approximation*, as stated already in Sec. 2.3.6.

For magnetite, the contrast was generated by calculation of PEEM ratio images at different energies. In Fig. 8.1, typical shapes of XMLD spectra are shown for several types of XMLD. Ratio images were computed as $I(E_1)/I(E_2)$ for the energies shown in the plot as vertical lines $E_1 = 724.2$ eV and $E_2 = 725.4$ eV.

8.2. Results of the fitting process

The fitting routine for the XMLD contrast is schematically shown in Fig. 8.2. The experimental input data are line profiles derived from PEEM images, which have been averaged over a certain width (20 pixels) perpendicular to the line to reduce noise. To achieve maximum accuracy, a *combined fit* of all three domain wall types in all possible contrast mechanisms (XMCD, XMLD p/s) has been performed, comprising a *full 360° rotation* of the magnetization *in a locally strongly confined area*. This local measurement minimizes any long-range artifacts such

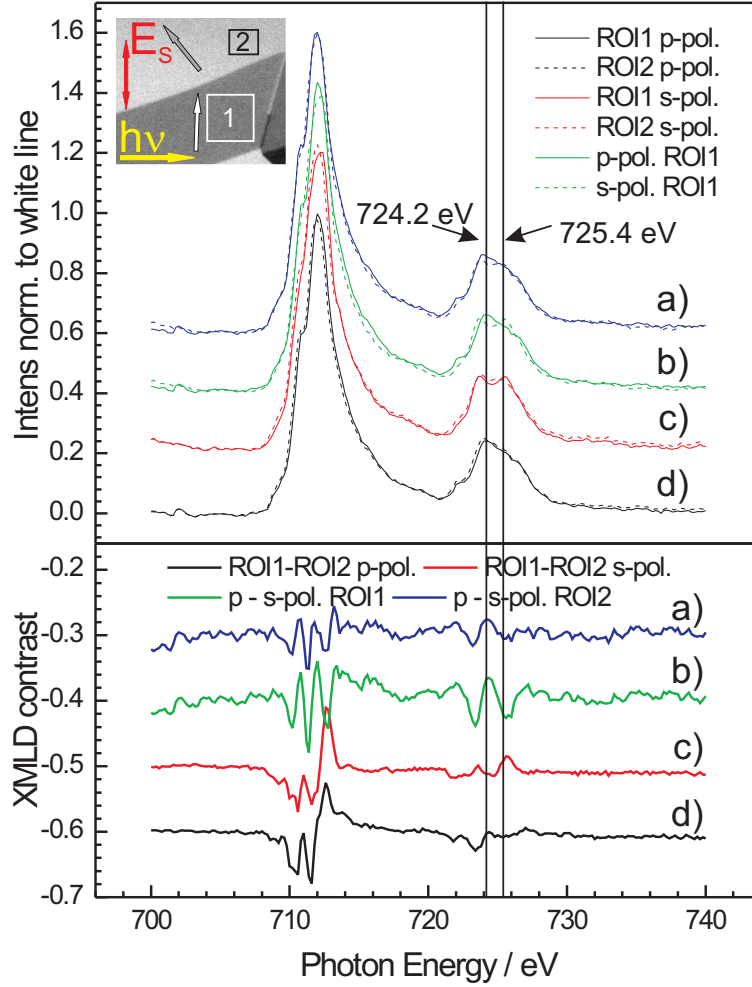


Figure 8.1.: Different XMLD spectra for magnetite: Spectrum (b) represents the "standard" method of calculating the XMLD, which is also called *XMLD contrast of the first kind* [151]: For a given direction of \mathbf{S} , the difference $I(\mathbf{E}||\mathbf{S}) - I(\mathbf{E} \perp \mathbf{S})$ is evaluated. In (b), $I_{\text{p-pol.}}^{\text{ROI1}}(\mathbf{S} \perp \mathbf{E}||[110]) - I_{\text{s-pol.}}^{\text{ROI1}}([111] \approx ||\mathbf{S} \approx ||\mathbf{E})$ was evaluated, which approximately corresponds to the standard method. The spectrum consequently looks very similar to the (inverted) XMLD spectrum of ARENHOLZ *et al.* for the magnetite (110) surface with $\phi_S = 45 - 60^\circ$, since the angle of the [111] direction with [001] is 54.73° . Spectrum (a) looks similar to (b), however with a smaller contrast. In spectra (c) and (d) one can directly see that choosing a different method of XMLD calculation directly leads to completely different XMLD spectra. Here, the so-called *XMLD of the second kind* was computed, i.e. the difference of spectra with $\mathbf{S}||\mathbf{E} - \mathbf{S} \perp \mathbf{E}$. This has been achieved by subtracting the spectra of two different domains for the same polarization). The energies for generation of the PEEM contrast shown as vertical lines had first been chosen to maximize the XMLD contrast of *first kind*. Domain contrast gained from PEEM images with a single polarization orientation, however, represent the XMLD contrast of the *second kind*. which – as is directly apparent – is considerably weaker at the chosen energies, however still sufficient for a good signal-to-noise ratio.

as inhomogeneous background intensity or energy dispersion errors ¹. In case of a full in-plane rotation of the magnetization, another advantage is that the XMCD profile comprises the entire dynamic range of the contrast, thus allowing self-calibration.

For the domain wall structure, a simple *in-plane* rotation was assumed in both materials, using a $\tanh(\alpha(x))$ -model, where α is the *in-plane* rotation angle. In terms of micromagnetic theory, this may be a crude approximation, but experimentally is justified, because the transition width is close to the PEEM resolution. Therefore, slight local deviations between model and experiment concerning the differential rotation angle $\frac{d\alpha}{dx}$ inside the wall cannot be determined. The most important implication of this model is that the AF spins of different sublattices rotate as a rigid spin-axis, retaining their collinearity throughout the wall (i.e. the situation shown in Fig. 3.2.1 (b)). Despite its simplicity, the model allows to reproduce all features of the XMD contrast. Any severe deviations of theoretical and experimental contrast can therefore help to identify a non-in-plane rotation or non-collinear magnetism.

Fe₃O₄ and NiO XMLD were measured in p- and s-geometry. The final fit was performed including all three contrast mechanisms into one χ^2 at equal weights. While for the XMLD the complex relations of anisotropic XMLD were used as described earlier, for the XMCD, a simple $\cos(\angle \boldsymbol{\sigma}, \mathbf{S})$ relation was sufficient.

The number of fit parameters has been reduced to a minimum by assuming a constant domain wall width of 200 nm and using a single scaling parameter for the angular part in the XMLD for each material. The spin-axis orientations inside the domains have been initialized to the easy directions of magnetite [$\pm 1 \mp 1 1$], but this choice lead to poor convergence of the fit and the XMCD signal was not reproduced correctly. Finally, a tilt of the magnetization towards the $[\underline{1}10]$ -axis resulted in good convergence and the characteristics of all domain wall profiles was reproduced correctly.

Note that in all the fits the theoretical magnitude of the contrast peaks in the walls is larger than the one observed experimentally, as becomes apparent in Fig. 8.3 especially for the 180°-walls in all contrast types and for the other types predominantly manifests in the peaks in XMLD p-contrast. With p-polarization, the NiO-XMLD contrast gets extremal each time the spin-axis crosses near a $[001]$ or $[\underline{1}10]$ -axis, as can be compared in Fig. 6.6 (A). The peaks in the line profiles of Fig. 8.3 thus indicate the approximate position of the *wall-core*.

¹In the dispersive direction of the image, there can be a contrast variation since the energetic condition for maximum XMD is only fulfilled for a narrow line parallel to the exit slit

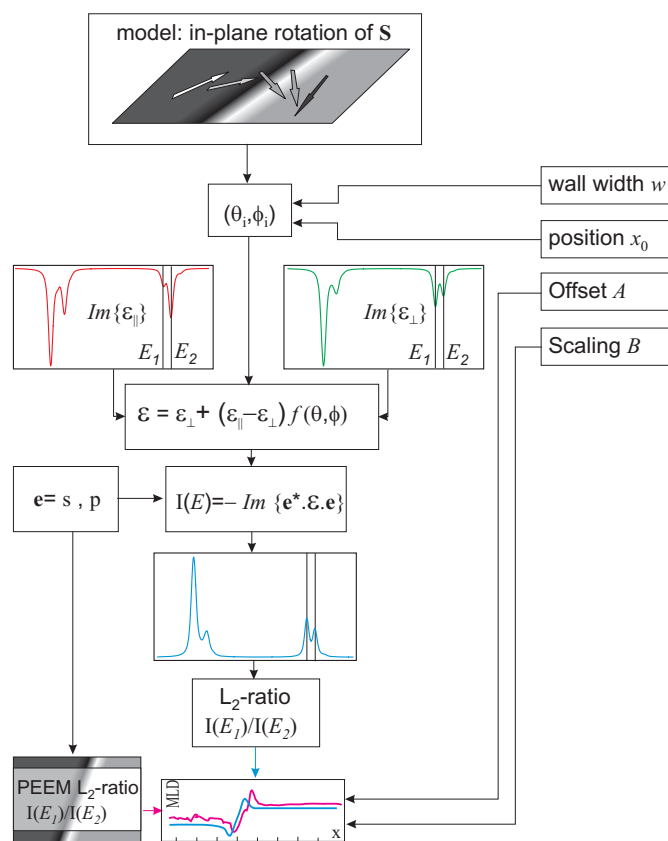


Figure 8.2.: Schematic view of the fitting process. Two fundamental spectra from the theory side and 5 experimental wall profiles serve as input.

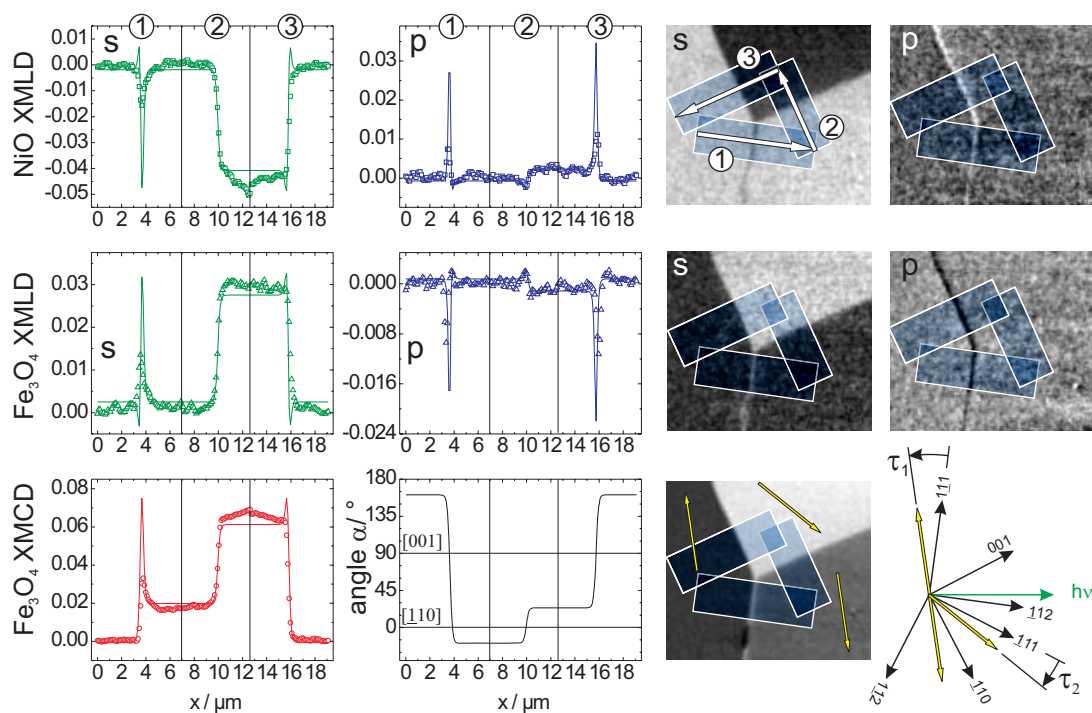


Figure 8.3.: (color) Domain wall profiles comprising all three types of walls in the Fe_3O_4 (110)/NiO system. Right hand side: PEEM images and profiles positions in the different contrast mechanisms. Lower right: Yellow arrows denote the deviation of the spin-axis (magnetization) at the interface from the crystallographic $[\pm 1 \mp 11]$ directions. Note that the deviation is always directed towards $\langle \underline{110} \rangle$, which is a sign of an additional uniaxial contribution along that axis.

A contrast reduction near the wall-core can have several reasons, which will be discussed in the following: (i) There may be a resolution problem due to limitations stemming from the PEEM apparatus function and the profile generation process, yielding an effective resolution around 100-200 nm. The true width of the domain walls must then be below that value. On the other hand, it appears that especially the 180° -domain walls are very wide (> 200 nm assumed in the fits), thus in principle the observed contrast should not be reduced as compared to theory. (ii) If the resolution is sufficient, the reduction might be caused by either a *deviation from pure in-plane rotation* or the formation of a partly *non-collinear spin-structure* near the wall-core, which should reduce both XMLD and XMCD. Both possibilities are very interesting and will be subject of further investigations. In general, however, the good matching of the theoretical profiles to the experimental data suggests that a collinear rotation equivalent to Fig. 3.2.1 (b) may be the dominant mechanism.

The best χ^2 was finally found for a tilt of $\tau_1 = 16^\circ$ and $\tau_2 = 11^\circ$ from the respective $\langle 111 \rangle$ -axis towards the $[\underline{1}10]$ direction (see Fig. 8.3). This clearly indicates that an additional uniaxial anisotropy along the $[\underline{1}10]$ -direction is present in the system. Astonishingly, the best fit also accounts for the Fe_3O_4 XMCD and XMLD data. On first glance, one may expect a more bulk-like behaviour, when the probing depth λ_e of the electrons is large. In fact, GOERING *et al.* [50] have recently found a very small λ_e of only 0.8 \AA in Fe_3O_4 single crystals, in contrast to earlier measurements of GOTA *et al.* [54], who reported 50 \AA in thin films. This suggests that the magnetite XAS is very sensitive to the topmost (interfacial) monolayers, thus probing mainly the interface anisotropy, and not the bulk. Furthermore, the magnetite and NiO XMLD show the same characteristics in the domain wall profiles, only the angular parameter has different signs, which is a consequence of the arbitrary choice of the spectral features for contrast generation. This means that the NiO spin-axis follows the interface anisotropy and collinear coupling is realized. Having a closer look at the separate bulk anisotropies of the two constituents, the interfacial anisotropy can be explained by a combination of the former with the collinear exchange coupling at the interface: While the magnetite bulk anisotropy prefers the in-plane $[\pm 1 \mp 1 1]$ - directions at the surface [177, 77], the easy planes of NiO are of (111) type. As already discussed in Sec. 7.4.1, the interfacial coupling situation forces *out-of-plane* stacking vectors along $[1 1 \pm 1]$ in NiO. So the easy planes form an angle of 35° with the interface plane, and the intersection is the $[\underline{1}10]$ axis. Thus, it is very likely, that the NiO contribution to the interface anisotropy is uniaxial and favours the $[\underline{1}10]$ -axis. Consequently, at the interface, a tilting of the spin-axis (magnetization) towards the $[\underline{1}10]$ -direction may be expected. The good fit quality for the XMLD in the thin NiO layer clearly shows that this interface anisotropy is projected into the *whole* NiO layer via the strong interface coupling (compare discussion in Sec. 6.3.3). Again, it should be

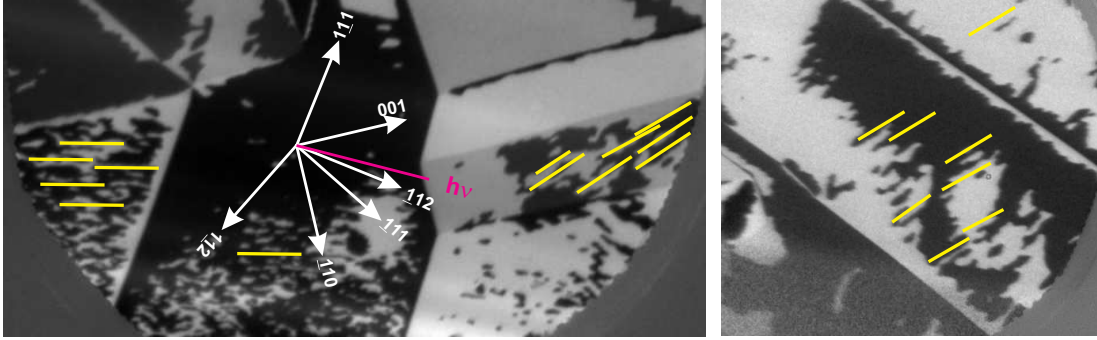


Figure 8.4.: Analysis of the long axes of the Co domains.

emphasized, that the Fe_3O_4 (110) surface itself may provide a uniaxial template along $[\underline{1}10]$, namely by reconstruction. JANSEN *et al.* report the formation of 2.8 \AA high stripes (two atomic layers), running along $[\underline{1}10]$ with a spacing of two to four times the bulk lattice constant (8.397 \AA) [67]. Since we applied a similar preparation method, such a reconstruction is likely to occur also in our samples. If the reconstruction persists upon deposition of the NiO layer – or is formed by the annealing process – the interface contains a uniaxial ”structure” along $[\underline{1}10]$, possibly also manifesting in the magnetic anisotropy.

An additional confirmation of this ”strange” anisotropy induced in the antiferromagnet by the exchange coupling is found in the data of a 15 \AA Co layer, which has finally been deposited on top of the $\text{Fe}_3\text{O}_4/\text{NiO}$ system (Fig. 8.5). The cobalt magnetization forms an angle of 90° with respect to that of magnetite, as can be seen from the respective PEEM images: 4 gray levels can be discerned both at the Fe and Co edge, which belong to the four possible easy directions. Domains showing the maximum (minimum) contrast in Fe-XMCD exhibit intermediate contrast values at the Co edge, while domains with intermediate contrast levels in magnetite XMCD show the extremal values in the Co-XMCD. This directly indicates a tendency for mutual perpendicular orientation of the Co and Fe_3O_4 magnetization. We’d like to postpone the discussion of the reasons for this behaviour to the next section in order to finish our discussion of the magnetic anisotropy in our trilayer system first. With respect to the magnetic anisotropy in our sample, the shape of the Co domains in our sample provides valuable information. The topology tends to consist of 180° -domains with an elongated shape along a particular direction. The long axis coincides with the easy axis of the coupled Co layer, because in this way charged 180° -walls are avoided. If the magnetite’s interface anisotropy were along $[\pm 1 \mp 1 1]$, this easy axis should point along $[\mp 1 \pm 1 2]$, always perpendicular to the respective direction in magnetite. However, evaluation of a sufficient number of small domains (shown in Fig. 8.4) yields a direction, which always deviates from $[\mp 1 \pm 1 2]$ towards $[001]$ by some angle. Turning sense

and magnitude of the deviation ($\approx 18^\circ$) are consistent with the findings at the $\text{Fe}_3\text{O}_4/\text{NiO}$ interface ($\approx 13.5^\circ$). Hence, we conclude that the interface anisotropy created by the coupling between NiO and Fe_3O_4 is transferred to the Co via the antiferromagnet and leads to the same deviation and turning sense from the respective crystallographic directions.

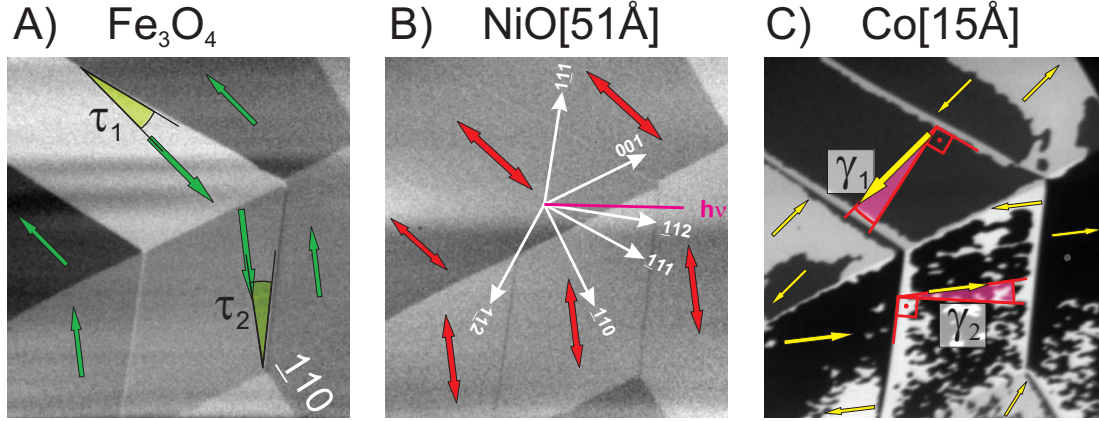


Figure 8.5.: (color) PEEM pictures of the $\text{Fe}_3\text{O}_4/\text{NiO}[51\text{ \AA}]/\text{Co}15\text{ \AA}$ system. Directly after deposition the Co-XMCD contrast shows a large number of elongated small domains. Analysis of the long axis yields directions deviating from $[\pm 1 \mp 1 2]$ towards the $\langle 001 \rangle$ -axis ($\gamma_1 \approx 22^\circ$ and $\gamma_2 \approx 14^\circ$). Thus the deviation is consistent with the one observed at the $\text{Fe}_3\text{O}_4/\text{NiO}$ interface, and the Co magnetization forms an angle of $\approx 90^\circ$ with the Fe_3O_4 magnetization.

8.3. Origin of the perpendicular FM orientation

We have, on purpose, avoided the term perpendicular *interlayer exchange coupling* in the headline of this section, since it directly provokes the association of biquadratic coupling between two FM layers via a non-insulating spacer layer. In our case, however, the spacer is an insulating NiO layer of 50 \AA thickness, which should prevent any interlayer exchange coupling *and* tunneling effects [144, 142, 143]. In the systems described in this thesis, the typical length scale of exchange interactions was found to be of the same size as the lattice parameter. Thus, intrinsic mechanisms based on RKKY-type interactions responsible for bilinear and biquadratic interlayer coupling in conductors can be ruled out.

SLONCZEWSKY proposed a second mechanism producing biquadratic interlayer coupling [141]. In his model, he assumed a trilayer system with conducting or tunneling spacer and a direct exchange mechanism between the two ferromagnets

via the spacer. Assuming imperfect interfaces with terraces, lateral fluctuations in the interlayer coupling parameter were introduced, leading to a biquadratic term via torque fluctuations acting on the two ferromagnets. It was found that the biquadratic coupling parameter J_2 *increased* with the terrace width L , up to a critical dimension, where the model breaks down. This theory has been confirmed by measurements on metallic Fe/Cu/Fe trilayers with detailed roughness analysis, where the increase of J_2 with L has indeed been observed [61].

It is worth noting that the model assumes a *direct* coupling of two ferromagnetic layers across the spacer. At first glance, one might therefore think, that it cannot account for the case of thick insulating spacer layers, where the decay length of the tunneling states is much shorter than the barrier width. If, however, the spacer is insulating but antiferromagnetic, a short-range internal exchange coupling can mediate magnetic information through the barrier, as long as its width is not too large.

Investigating this aspect, CAMERERO *et al.* experimentally found a 90° angle between the easy axes of (111) textured NiFe and Co layers separated by 40-250 Å thick polycrystalline NiO spacers [21]. They invoked a numerical 3D Heisenberg model, which tried to explain the coupling in terms of monatomic steps at the interfaces – in analogy to SLONCEWSKY’s theory, but with a correct treatment of the spacer considering only nearest neighbour exchange. The AF spacer was modelled as a layered antiferromagnet with ferromagnetic sheets parallel to the interface, somewhat idealizing the (111) textured polycrystalline NiO. Interfacial terraces at both sides of the AF then cause partial internal spin frustration, since locally the AF cannot always satisfy the coupling conditions at both interfaces simultaneously. As a consequence, the model resulted in a perpendicular alignment of both ferromagnets. In the following, we shortly outline our interpretation of this effect:

In case of spin frustration inside the AF by collinear alignment of both FM’s together with monatomic interface steps, the system has two possibilities to lower its energy. The first one is, that the AF assumes a spin-flop state with respect to the two – still collinear – ferromagnets. Thereby the internal spin frustrations are removed, and transferred to the interface, where the energy may be lowered by a spin-flop state with spin-canting. However, the canted spin-structure will extend into the AF layer, forming an artificial AF superstructure as well, which means that even the spin-flop state in the AF will appear as a layered antiferromagnet when looking at the net moment induced by canting. Thus, the unfavourable situation is not fully resolved. Only if the AF is thick enough, the superstructure will vanish inside the bulk before reaching the other interface. If this is not the case, the energy can be further lowered if the two ferromagnets align perpendicular to each other, forcing the AF to assume *spiraling spin structures*. These structures

are equivalent to a locally fluctuating *indirect* coupling between the two ferromagnets, in analogy to the fluctuating *direct* coupling assumed in SLONCZEWSKY's model. In sufficiently thin insulating AF spacers with interface roughness, the interlayer coupling can therefore still be modelled by a locally fluctuating interlayer exchange constant.

The observation of perpendicular interlayer coupling for spacer thicknesses as high as 250 Å was ascribed by CAMARERO *et al.* to the low anisotropy of the NiO layer, which is polycrystalline *and* (111)-textured. We share this opinion, and speculate that, if the AF anisotropy were larger, canted spin-structures and spirals would not extend far into the AF layer. In this case, perpendicular interlayer coupling would only be observed for low spacer thicknesses, while for higher thicknesses, the magnetization of both ferromagnets may align collinear again.

This hypothesis is indeed supported by experimental findings: VAN DER HEIJDEN *et al.* found perpendicular alignment in single-crystalline (001)-oriented Fe₃O₄/NiOFe₃O₄-trilayers for spacer thicknesses of 7-50 Å, which they ascribed to the effect of interface roughness[158]. For thicknesses greater than 50 Å, a gradual collinear realignment of the two layers was observed, in accordance with the thoughts formulated above. Similar findings are reported by BAMBRILLA *et al.*, who observed a collinear realignment for $t_{\text{NiO}} > 40$ Å in (001)-oriented Fe/NiO/Fe-trilayers [18].

We'd like now to discuss the situation in our samples on the background of the facts we have compiled above:

Since the Fe₃O₄/NiO system grows with high epitaxial order and sharp interfaces, we have every reason to assume that our interfaces are of good quality [121, 16, 166, 77], and an idealized situation as described in the model by SLONCZEWSKY can be assumed in interpreting our results. In particular, the terrace width L is definitely considerably larger than in amorphous or polycrystalline samples, leading to a large biquadratic contribution in the coupling energy according to the model. Hence, we consider it possible that a roughness-driven perpendicular coupling is realized in our system as well, although the occurrence is astonishing in view of the high insulating spacer thickness of 51 Å. Comparison to the results of VAN DER HEIJDEN *et al.* indicates – as far the different crystalline orientation allows – that we may still be in the range, where perpendicular coupling occurs.

However, we can provide a second hypothesis, in which perpendicular coupling is ascribed to the different *individual* coupling behaviour of Fe₃O₄ respectively Co to NiO: ARENHOLZ *et al.* recently found spin-flop coupling for the Co/NiO(001) interface, in contrast to earlier works, which erroneously came to the conclusion of parallel coupling in this system, since the effects of "anisotropic" XMLD

had not been considered [2]. The recent results at the (110) [77] and (001) interface suggest that spin-flop coupling in the Co/NiO system is a result of the compensated nature of those interfaces, as expected from KOON's theory [75]. The NiO(110)/Co interface would then favour spin-flop coupling in contrast to the Fe₃O₄ (110)/NiO interface, for which we have confirmed collinear coupling. The overall outcome is a perpendicular alignment of both layers. This is a possibility, which has not been considered for heterogeneous trilayers, yet. To test the validity of this theory, spacer-thickness-dependent measurements have to be performed. If a reorientation transition back to parallel is absent for higher thicknesses, the effect is caused by the individual coupling of the two layers to the NiO-spacer.

8.4. Summary

To summarize, in the Fe₃O₄ (110)/NiO [51 Å] system, fits of domain wall profiles have been performed in the AF as well as in the substrate. The good accordance of the experimental data with a simple *in-plane* rotation model suggests that the spin-axis is coupled collinearly and rotates coherently along with the substrate magnetization. Deviations in the maximum contrast arising especially with p-polarized light may point to a small amount of out-of-plane rotation or non-collinear spin-order inside the wall-core.

The easy axes found in the coupled AF as well as in the interface-near substrate layers deviate from the $\langle 111 \rangle$ directions preferred by bulk magnetite. The deviation is directed towards $\langle \underline{1}10 \rangle$, which indicates that by interface coupling, an additional uniaxial anisotropy along that axis is introduced. In a simple picture the interface anisotropy is thus a combination of several effects

- the magnetite's bulk cubic anisotropy preferring $\langle \pm 1 \mp 1 1 \rangle$ easy axes at the surface,
- the collinear interface coupling,
- the AF anisotropy with $(1 1 \pm 1)$ easy planes
- the magnetoelastic coupling due to epitaxial strain favouring *out-of-plane* stacking vectors, thus the intersection of the NiO easy planes with the interface is $[\underline{1}10]$
- possibly a surface/interface reconstruction with one-dimensional structures running along $[\underline{1}10]$

This interpretation is strongly supported by the deposition of a 15 Å Co layer on top of NiO, which then shows the same angle and turning sense of the deviation in its easy direction: The Co layer magnetization is oriented perpendicular to the magnetization in the substrate, and its crystallographic easy axes would be along $[\pm 1 \mp 1 2]$. The Co magnetization thus deviates by 10-20° towards [001], whereas the Fe₃O₄ magnetization and the NiO spin-axis deviate by the same amount towards $[\underline{1}10]$. The perpendicular interlayer coupling between Fe₃O₄ and Co via the NiO layer can be explained by a roughness-driven effect as described in Refs. [141, 158, 21]. We think, however, that an individually different coupling behaviour for magnetite and cobalt may lead to the same effect, since cobalt couples spin-flop to NiO, magnetite collinearly.

9. Conclusions and Outlook

In this thesis, the magnetic proximity effect in highly-ordered transition metal oxide (TMO) heterosystems composed of single crystals of ferrimagnetic (FIM) Fe_3O_4 and thin antiferromagnetic (AF) NiO layers has been investigated. The method applied was Photoelectron Emission Microscopy using polarized soft x-rays (X-PEEM), providing spatially-resolved and element-selective information about the crystalline and magnetic order in the sample. Important progress was made in the interpretation of "anisotropic" XMLD, allowing for vectorial magnetometry of collinear magnetic structures in singly crystalline systems. In contrast to the "isotropic" effect, "anisotropic" XMLD occurs whenever the crystalline symmetry of the sample is not spherical any more [82, 83, 32, 8, 9].

It was found, that two major contributions to the MPE exist: First, interfacial exchange interactions, which are generally short-ranged in TMO's, create an ultrathin zone of altered magnetic structure near the interface. Second, long-ranged magnetoelastic interactions lead to a change of the magnetic structure on a larger scale, sometimes affecting the whole NiO layer. The influence of directional lattice strain on the magnetic order via magnetoelastic coupling has been investigated by means of samples with different crystallographic low-index orientations of the interface. For all samples, the magnetic domain pattern of the ferrimagnetic substrate is imprinted into the thin antiferromagnetic NiO layer. Due to the surface demagnetizing field of the substrate and the interface exchange coupling, the NiO spin-axis is oriented within the film-plane for all samples. Dependent on the type of the interface, however, a difference in the *in-plane* coupling behaviour of the antiferromagnetic NiO layer to the ferrimagnetic Fe_3O_4 substrate was observed. While NiO couples collinearly to Fe_3O_4 for the (111) and (110) orientations, spin-flop coupling was observed for the (001)-interface. At first glance, this finding contradicts the theory of KOON [75], which postulates spin-flop coupling for every compensated interface, i.e. both for (110) and (001). An explanation for the deviating results is given in terms of the microscopic interface structure and additional magnetoelastic effects.

In addition to the different coupling scheme, the amount of uncompensated magnetization varies in the three orientations, with the (110)-interface showing the

largest value and the two other orientations only a small amount of 10% as compared to the value for (110). This behaviour can be explained in terms of the bonding situation and in-plane anisotropy of the different orientations. For a NiO wedge on Fe₃O₄ (110), extremal values for the Ni and Fe- orbital moments near 1 ML thickness were found. For higher thicknesses, the Ni- orbital moment reduces almost to zero, indicating a quenching or compensation as soon as cubic symmetry is established. The thickness-integrated spin-moment, however, remains constant, suggesting that the uncompensated magnetization in NiO resides directly at the interface and is induced by the exchange coupling to Fe₃O₄, whereas the bulk of the NiO layer is compensated.

Temperature-dependent measurements of the XLD contrast reveal a lowered blocking temperature of the NiO layer as well as a reduced Fe₃O₄ CURIE temperature near the interface. While the former arises from finite size effects, the latter is probably a consequence of the interfacial coupling to NiO, which has a lower critical temperature than magnetite. The scaling of the NiO XMLD contrast with temperature follows shows a linear behaviour in a wide temperature range of about $0.6 - 1 T_B$, which is consistent with mean-field calculations of the expectation value $\langle \mu^2 \rangle$ of the magnetic moment.

Finally, the AF domain state in Fe₃O₄ (110)/NiO was investigated in more detail, fitting profiles of constrained antiferromagnetic domain walls to the theoretically expected XMLD contrast. The results are consistent with a simple in-plane rotation model of the NiO spin-axis, ruling out the anticyclic sublattice rotation postulated by YAMADA. Furthermore, a peculiar magnetic anisotropy was found in the system, with easy axes turned from the $[\pm 1 \mp 1 1]$ -orientation towards $[\underline{1}10]$ by about 15°. This anisotropy can be understood as a composition of different contributions. The magnetocrystalline anisotropy of Fe₃O₄ favours $\langle 111 \rangle$ easy-directions, of which two are coplanar with the sample interface, namely $[\pm 1 \mp 1 1]$. The magnetic and magnetoelastic anisotropy of NiO prefers (111) easy planes and $\langle 111 \rangle$ AF stacking vectors. The epitaxial lattice strain in NiO favours out-of-plane stacking, leading to easy planes, which are not coplanar with the sample interface. The energetically most favourable NiO spin-axis orientation is thus the intersection of the easy plane with the sample interface, i. e. $[\underline{1}10]$. The interfacial exchange coupling tends to orient NiO and Fe₃O₄ spins collinear, thus leading to a weighted mixture of the Fe₃O₄ $[\pm 1 \mp 1 1]$ easy-axes with $[\underline{1}10]$ preferred by NiO. As a result, the overall easy-axis deviates from its orientation in Fe₃O₄ towards the $[\underline{1}10]$ -axis, as observed experimentally.

In a further step, we investigated a Fe₃O₄ (110)/NiO/Co trilayer system, which exhibits perpendicular interlayer coupling via the antiferromagnetic spacer. The easy directions of the Co layer is determined by the anisotropy of the Fe₃O₄ (110)/NiO system as well as its tendency for mutual perpendicular alignment

with Fe_3O_4 . Accordingly, the Co magnetization is tilted from the $[\pm 1 \mp 1 2]$ easy directions perpendicular to the ones in Fe_3O_4 towards the $[001]$ -axis – exhibiting the same tilt angle and turning sense as observed for the Fe_3O_4 magnetization.

For the perpendicular interlayer coupling, we found two possible explanations: (i) as proposed by SLONCZEWSKY [141], roughness-driven fluctuations in the effective interlayer exchange coupling lead to perpendicular coupling. Note, that the spacer layer is an insulating antiferromagnet of high thickness (51 Å), which means that interlayer coupling is not a direct mechanism as assumed by SLONCZEWSKY, but mediated indirectly via the short-range superexchange in NiO. (ii) There is evidence, that Fe_3O_4 and cobalt exhibit a different coupling behaviour to NiO: while Fe_3O_4 couples collinearly – as found in our experiments – cobalt may exhibit a spin-flop coupling when evaporated onto NiO, as reported by [9].

This thesis uncovered some important aspects of the magnetic proximity effect in highly-ordered systems. There are, however, still many unanswered questions, and more work has to be done in the future to obtain a clearer picture. The main goal is to obtain more detailed information on the magnetoelastic contribution to the proximity effect, for example, by measuring samples under application of variable stress in well-defined crystallographic directions. The influence of epitaxial strain may be estimated by growth on substrates with variable lattice mismatch, too. Furthermore, more materials have to be investigated. A comparison of the simple antiferromagnets MnO, FeO and CoO, when coupled to suitable transition metal oxides, may provide more insights in to the interplay of exchange- and magnetoelastic coupling as-well.

For the first time, results have been presented concerning the micromagnetic order of constrained antiferromagnetic domain walls. These very exotic magnetic structures deserve a more detailed investigation, the major challenge being a microscopic study with higher resolution well below the domain wall width of ≈ 200 nm. On the background of the recent insights into the "anisotropic" nature of XMLD in single crystals, also the bulk NiO AF domain walls should be revisited, which up to now have only been investigated once by WEBER *et al.* [167]. Since their analysis was based on the "isotropic" XMLD theory, important details of the magnetic wall-structure might have been missed or misinterpreted.

Finally, the interlayer coupling across conducting and insulating antiferromagnetic spacer layers is a highly interesting topic, for which theories are just in their nascent state and experimental studies are still rare [158, 38, 21, 91]. By measurements in highly-ordered transition metal oxide systems, varying spacer thickness, interface-orientation and magnetoelastic strain, important new insights into the microscopic origins of interlayer coupling in highly correlated systems may be

gained, possibly with high technological value for the design of spin-valves or tunnelling devices.

All the ideas presented above may rely on soft x-ray photoemission microscopy as the main tool for structural, chemical and magnetic analysis with high resolution.

A. Appendix

A.1. Epitaxial strain and magnetoelastic distortions in different interface orientations of the $\text{Fe}_3\text{O}_4/\text{NiO}$ system

A.1.1. Epitaxial strain of the NiO layer

In the following, we derive the strain that is induced in NiO by epitaxial growth on magnetite in various crystallographic interface orientations. The epitaxial strain is determined by the lattice mismatch and the interface orientation induces a particular strain configuration in the crystal lattice of NiO, thereby lowering its symmetry. Due to the magnetoelastic anisotropy of NiO, which is linked to the crystal lattice, different magnetic properties will arise for different interface orientations. This has important consequences on the magnetic coupling of the two substances. We begin by writing down the formulae for the epitaxial in-plane and out-of-plane strain dependent on crystallographic orientation, as derived by SANDER in ref. [127]. For the (001) surface, the epitaxial strains are given by

$$\eta_3 = -\frac{c_{12}(\eta_1 + \eta_2)}{c_{11}}, \quad (\text{A.1})$$

where η_3 is the *out-of-plane* strain and η_1, η_2 are the *in-plane* strains. If we assume that the NiO assumes the maximum in-plane strain determined by the lattice mismatch of +0.005, then taking the elastic constants for NiO as given in table A.1, we yield $\eta_3 = 4.04 \cdot 10^{-3}$, a compression along the surface normal. Shear strain components are zero in this orientation, since the strain works along the C_4 axes. For the (110) surface, one obtains the following result after transforming the strain tensor into surface coordinates:

$$\hat{\boldsymbol{\eta}} = \begin{bmatrix} \frac{1}{2}\eta_1^{(s)} + \frac{1}{2}\eta_3^{(s)} & -1/2\eta_1^{(s)} + \frac{1}{2}\eta_3^{(s)} & 0 \\ -\frac{1}{2}\eta_1^{(s)} + \frac{1}{2}\eta_3^{(s)} & \frac{1}{2}\eta_1^{(s)} + \frac{1}{2}\eta_3^{(s)} & 0 \\ 0 & 0 & \eta_2^{(s)} \end{bmatrix}. \quad (\text{A.2})$$

What remains is to express the *out-of-plane* strain by the *in-plane* strain:

$$\eta_3^{(s)} = -\frac{(c_{11} + c_{12} - 2c_{44})\eta_1^{(s)} + 2c_{12}\eta_2^{(s)}}{c_{11} + c_{12} + 2c_{44}}. \quad (\text{A.3})$$

In the (110) orientation, the shear strain η_{12} is nonzero and the NiO film will have monoclinic symmetry. Assuming again the full in-plane lattice distortion of 0.5%, the film is compressed along the surface normal [110] by $-2.78 \cdot 10^{-3}$. Finally, for the (111) surface, the strain tensor and out-of-plane strain are defined as

$$\eta_3^{(s)} = -\frac{(c_{11} + 2c_{12} - 2c_{44})(\eta_1^{(s)} + \eta_2^{(s)})}{c_{11} + 2c_{12} + 4c_{44}} \quad (\text{A.4})$$

$$\hat{\boldsymbol{\eta}} = \begin{bmatrix} \frac{1}{2}\eta_1^{(s)} + \frac{1}{6}\eta_2^{(s)} + \frac{1}{3}\eta_3^{(s)} & -\frac{1}{2}\eta_1^{(s)} + \frac{1}{6}\eta_2^{(s)} + \frac{1}{3}\eta_3^{(s)} & -\frac{1}{3}\eta_2^{(s)} + \frac{1}{3}\eta_3^{(s)} \\ -\frac{1}{2}\eta_1^{(s)} + \frac{1}{6}\eta_2^{(s)} + \frac{1}{3}\eta_3^{(s)} & \frac{1}{2}\eta_1^{(s)} + \frac{1}{6}\eta_2^{(s)} + \frac{1}{3}\eta_3^{(s)} & -\frac{1}{3}\eta_2^{(s)} + \frac{1}{3}\eta_3^{(s)} \\ -\frac{1}{3}\eta_2^{(s)} + \frac{1}{3}\eta_3^{(s)} & -\frac{1}{3}\eta_2^{(s)} + \frac{1}{3}\eta_3^{(s)} & \frac{2}{3}\eta_2^{(s)} + \frac{1}{3}\eta_3^{(s)} \end{bmatrix}. \quad (\text{A.5})$$

The out-of-plane compression resulting from the epitaxial strain in the (111) orientation is $-2.44 \cdot 10^{-3}$, i.e. the NiO layer is compressed along the surface normal. Note that the distortion along arbitrary directions in the sample can be calculated if the complete strain tensor is known:

$$\eta_{\mathbf{n}} = \mathbf{n}^T \hat{\boldsymbol{\eta}} \mathbf{n}, \quad \mathbf{n} \text{ unit vector} \quad (\text{A.6})$$

A.1.2. Magnetoelastic coupling

The substrate, which has cubic symmetry in the paramagnetic state, will experience a deformation by magnetostriction in its ferromagnetic state, which leads to a (small) deviation from cubic symmetry. This deformation, as well as the epitaxial strain is then transferred to the NiO layer, in case of a non-relaxed pseudomorphic growth. Thus the NiO layer itself will experience an additional distortion, which changes its magnetoelastic energy. In cubic symmetry, the magnetoelastic strain in a sample with unit magnetization direction $\mathbf{M}' = (\alpha_1, \alpha_2, \alpha_3)$ along a particular direction $\mathbf{n} = (\beta_1, \beta_2, \beta_3)$ is defined as [73]

$$\lambda_{\mathbf{n}}(\mathbf{M}') = \frac{3}{2}\lambda_{100} \left(\alpha_1^2\beta_1^2 + \alpha_2^2\beta_2^2 + \alpha_3^2\beta_3^2 - \frac{1}{3} \right) + 3\lambda_{111} (\alpha_1\alpha_2\beta_1\beta_2 + \alpha_2\alpha_3\beta_2\beta_3 + \alpha_1\alpha_3\beta_1\beta_3). \quad (\text{A.7})$$

The magnetoelastic energy of the material as given in [127] is

$$E_{\text{me}}(\mathbf{M}') = B_1 (\eta_1 \alpha_1^2 + \eta_2 \alpha_2^2 + \eta_3 \alpha_3^2) + B_2 (\eta_4 \alpha_2 \alpha_3 + \eta_5 \alpha_1 \alpha_3 + \eta_6 \alpha_1 \alpha_2) + \dots, \quad (\text{A.8})$$

with the strain components denoted in VOIGT-notation η_l ($l = 9 - (i + k)$). The magnetoelastic coupling constants B_1 and B_2 are related to the magnetostrictive deformations λ_{100} and λ_{111} via the elastic constants:

$$B_1 = -\frac{3}{2} \lambda_{100} (c_{11} - c_{12}) \quad , \quad B_2 = -3 \lambda_{111} c_{44} \quad (\text{A.9})$$

In principle, the equilibrium strain in the material system should be calculated by the minimization of the magnetoelastic energy contributions of both constituent materials – the Fe_3O_4 substrate and the NiO layer. This is a very complex problem and exceeds the scope of this thesis, since in principle finite element or slab calculations have to be performed in order to account for inhomogeneous strain along the sample normal. Instead a simpler approach has been chosen by assuming the substrate magnetization direction as fixed along the surface easy-direction. The second simplifying assumption is that the substrate dominates the thin layer, which then experiences the same in-plane distortions as the substrate. An elastic feedback of the NiO layer on the substrate was neglected. If one grossly assumes the elastic constants of magnetite and NiO as equal (which indeed is the case), the true strain of the material (and E_{me} , which depends linearly on it) is overestimated roughly by a factor of 2.

This does not pose a major problem, since we are interested in the order of magnitude of the magnetoelastic energy – anyway, the microscopic magnetoelastic properties are expected to deviate from the continuum picture applied here. Since magnetoelastic effects are thought to be significant only for the (001) interface, where epitaxial strain does not lift the energetic degeneracy of different NiO T-domains, calculations have been restricted to this crystallographic orientation. For the calculations we use the elastic parameters and magnetostriction constants in table A.1.

Since the bulk easy directions in magnetite are $\langle 111 \rangle$, we assume the magnetization to point along $[110]$. Our goal is now to get an estimate of the magnetoelastic energy difference between a collinear and a perpendicular spin-arrangement of the two materials Fe_3O_4 and NiO. The strain along the C_4 axes is easy to calculate:

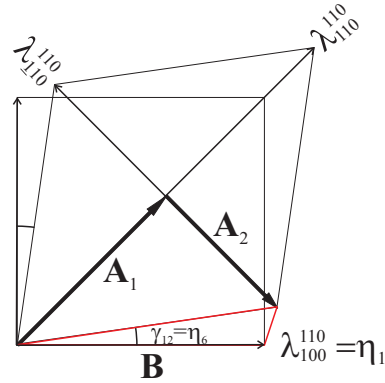


Figure A.1.: On the calculation of the shear strain.

material	c_{11}/GPa	c_{12}/GPa	c_{44}/GPa	Ref.	$\lambda_{100}/10^{-6}$	$\lambda_{111}/10^{-6}$	Ref.
NiO	270	105	125	[41]	-140	-79	[114]
NiFe ₂ O ₄	-	-	-	-	-46	-22	[145]
Fe ₃ O ₄	261	148	63	[123]	-20	80	[73]

Table A.1.: Elastic and magnetoelastic properties of NiO, NFO and magnetite.

$\eta_1 = \lambda_{100}^{110}$, $\eta_2 = \lambda_{010}^{110}$ and $\eta_3 = \lambda_{001}^{110}$. What remains is to calculate the shear strain. For this one needs the in-plane substrate distortions λ_n^M parallel and perpendicular to the magnetization, i.e. λ_{110}^{110} and $\lambda_{\bar{1}10}^{110}$ (see Fig. A.1). With those values, the shear strain η_6 in the NiO layer can be calculated as

$$\tan \gamma_{12} = \eta_6 \approx \frac{|\mathbf{A}_1 + \mathbf{A}_2 - \mathbf{B}|}{|\mathbf{B}|}, \quad (\text{A.10})$$

where the vectors are defined as shown in Fig. A.1:

$$\begin{aligned} \mathbf{A}_1 &= \frac{1}{2\sqrt{2}}[1 + \lambda_{110}^{110}, 1 + \lambda_{110}^{110}] \\ \mathbf{A}_2 &= \frac{1}{2\sqrt{2}}[1 + \lambda_{\bar{1}10}^{110}, -1 - \lambda_{\bar{1}10}^{110}] \\ \mathbf{B} &= [1, 0] \quad . \end{aligned} \quad (\text{A.11})$$

The remaining shear strain components are zero, since shearing is restricted to the surface plane. With the complete set of strain components inside the NiO layer, the magnetoelastic energy can be calculated for the NiO-spin parallel and perpendicular to the substrate magnetization. The values are $E_{me}^{\parallel} = -648 \text{ Jm}^{-3}$, $E_{me}^{\perp} = -4203 \text{ Jm}^{-3}$ and the the energy gain is $\Delta E_{me} = -3555 \text{ Jm}^{-3}$ as given in chapter 7.4.1.

A.2. Confusion and conversion – the SI and CGS systems

There is a lot of confusion caused by different systems of units used by experimentalists and theoreticians. While, for example, theoretical descriptions related to electrodynamics frequently make use of the CGS system (centimeter, gram, second), international conventions prefer the SI (MKS) system (meter, kilogram, second) to provide a standard for all physical quantities. Usually, we keep to the SI system, when presenting our experimental results. However, the theoretical explanations in Chap. 1 were carried out in CGS system, which is more convenient for electrodynamics. Therefore, we provide here some conversions between

SI and CGS systems for the relevant quantities. A more detailed discussion of the system-free MAXWELL equations can be found in Ref. [89]. Table A.2 summarizes the conversion constants and relevant quantities in system-free, CGS- and SI-definition.

quantity	general	CGS	SI
"JACKSON"-constant	k_E	1	$\frac{1}{4\pi\epsilon_0}$
"JACKSON"-constant	k_B	$\frac{1}{c}$	$\frac{\mu_0}{4\pi}$
"JACKSON"-constant	k_F	$\frac{1}{c}$	1
"JACKSON"-constant	k_D	1	ϵ_0
"JACKSON"-constant	k_M	c	1
"JACKSON"-constant	k_H	1	$\frac{1}{\mu_0}$
diel. displacement	$\mathbf{D} = k_D(\mathbf{E} + 4\pi k_E \mathbf{P})$ $= k_D \hat{\epsilon} \mathbf{E}$	$\mathbf{E} + 4\pi \mathbf{P}$ $\hat{\epsilon} \mathbf{E}$	$\epsilon_0 \mathbf{E} + \mathbf{P}$ $\epsilon_0 \hat{\epsilon} \mathbf{E}$
optical conductivity	$\hat{\sigma}$	$\hat{\sigma}$	$\hat{\sigma}$
diel. tensor	$\hat{\epsilon} = 1 + i4\pi k_E \hat{\sigma}$	$1 + i \frac{4\pi \hat{\sigma}}{\omega}$	$1 + i \frac{\hat{\sigma}}{\epsilon_0 \omega}$
fine structure constant	$\alpha = k_E \frac{e^2}{\hbar c}$	$\frac{e^2}{\hbar c}$	$\frac{e^2}{4\pi\epsilon_0 \hbar c}$
XAS-intens. normal. fact	$\mathcal{A} = 4\pi^2 \alpha \omega$	$4\pi^2 \frac{e^2}{\hbar c} \omega$	$4\pi^2 \frac{e^2}{4\pi\epsilon_0 \hbar c} \omega$
magnetic field	$\mathbf{H} = k_H(\mathbf{B} - 4\pi k_B k_M \mathbf{M})$	$\mathbf{B} - 4\pi \mathbf{M}$	$\frac{1}{\mu_0} \mathbf{B} - \frac{1}{4\pi} \mathbf{M}$

Table A.2.: Conversion of some important quantities from CGS to SI system.

Bibliography

- [1] V. M. AGRANOVICH AND V. L. GINZBURG, *Crystal Optics with Spatial Dispersion, and Excitons*, vol. 42, Springer, Berlin, 1984. 4
- [2] D. ALDERS, L. H. TJENG, F. C. VOOGT, T. HIBMA, G. A. SAWATZKY, C. T. CHEN, J. VOGEL, M. SACCHI, AND S. IACOBUCCI, *Temperature and thickness dependence of magnetic moments in NiO epitaxial films*, Phys. Rev. B, 57 (1998), p. 11623. 32, 33, 67, 82, 83, 86, 89, 123
- [3] D. ALDERS, C. VOGEL, J. LEVELUT, S. D. PEACOR, T. HIBMA, M. SACCHI, L. H. TJENG, C. T. CHEN, G. VAN DER LAAN, B. T. THOLE, AND G. A. SAWATZKY, *Magnetic x-ray dichroism study of the nearest-neighbor spin-spin correlation function and long-range magnetic order parameter in antiferromagnetic NiO*, Europhysics Letters (EPL), 32 (1995), pp. 259–265. 84, 86
- [4] S. ANDERS, H. A. PADMORE, R. M. DUARTE, T. RENNER, T. STAMMLER, A. SCHOLL, M. R. SCHEINFEIN, J. STÖHR, L. SÉVE, AND B. SINKOVIC, *Photoemission electron microscope for the study of magnetic materials*, Review of Scientific Instruments, 70 (1999), pp. 3973–81. 43
- [5] P. W. ANDERSON, *New approach to the theory of superexchange interactions*, Physical Review, 115 (1959), pp. 2–13. 35
- [6] P. W. ANDERSON AND H. HASEGAWA, *Considerations on double exchange*, Physical Review, 100 (1955), pp. 675–81. 39
- [7] E. ARAKAWA, K. MARUYAMA, K. MORI, H. NISHIGAITSU, AND N. AIZAWA, *Magnetostriction observed by x-ray diffraction in iron*, IEEE Trans. Magn., 41 (2005), p. 3718. 108
- [8] E. ARENHOLZ, G. VAN DER LAAN, R. CHOPDEKAR, AND Y. SUZUKI, *Anisotropic x-ray magnetic linear dichroism at the Fe $L_{2,3}$ edges in Fe_3O_4* , Physical Review B, 74 (2006), p. 094407. xviii, 31, 67, 112, 113, 125
- [9] E. ARENHOLZ, G. VAN DER LAAN, R. V. CHOPDEKAR, AND Y. SUZUKI, *Angle-dependent Ni^{2+} x-ray magnetic linear dichroism: Interfacial Coupling Revisited*, Phys. Rev. Lett., 98 (2007), p. 197201. xviii, 31, 32, 98, 112, 113, 125, 127

-
- [10] D. ATTWOOD, *Soft x-rays and extreme ultraviolet radiation, publisher = Cambridge University Press, Berkeley, CA, 2007.* 41
- [11] M. N. BAIBICH, J. M. BROTO, A. FERT, F. N. VAN DAU, F. PETROFF, P. EITENNE, G. CREUZET, A. FRIEDERICH, AND J. CHAZELAS, *Giant Magnetoresistance of (001)Fe/(001)Cr Magnetic Superlattices*, Physical Review Letters, 61 (1988), pp. 2472–2475. xvi
- [12] E. BAUER, *Photoelectron microscopy, 2001.* 42
- [13] G. BINASCH, P. GRÜNBERG, F. SAURENBACH, AND W. ZINN, *Enhanced magnetoresistance in layered magnetic structures with antiferromagnetic interlayer exchange*, Phys. Rev. B, 39 (1989), pp. 4828–4830. xvi
- [14] C. BINEK, A. HOCHSTRAT, AND W. KLEEMANN, *Exchange bias in a generalized Meiklejohn-Bean approach*, Journal of Magnetism and Magnetic Materials, 234 (2001), pp. 353–8. 54
- [15] M. BODE, E. VEDMEDENKO, K. VON BERGMANN, A. KUBETZKA, P. FERRIANI, S. HEINZE, AND R. WIESENDANGER, *Atomic spin structure of antiferromagnetic domain walls*, Nature Materials, 5 (2006), pp. 477–81. 112
- [16] J. A. BORCHERS, Y. IJIRI, D. M. LIND, P. G. IVANOV, R. W. ERWIN, S. H. LEE, AND C. F. MAJKRZAK, *Polarized neutron diffraction studies of exchange-coupled Fe_3O_4/NiO superlattices*, J. Appl. Phys., 85 (1999), pp. 5883–5. 96, 99, 111, 122
- [17] J. A. BORCHERS, Y. IJIRI, D. M. LIND, P. G. IVANOV, R. W. ERWIN, A. QASBA, S. LEE, K. V. O'DONOVAN, AND D. C. DENDER, *Detection of field-dependent antiferromagnetic domains in exchange-biased Fe_3O_4/NiO superlattices*, Appl. Phys. Lett., 77 (2000), pp. 4187–4189. 96, 99, 111
- [18] A. BRAMBILLA, P. BIAGIONI, M. PORTALUPI, M. ZANI, M. FINAZZI, L. DUÒ, P. VAVASSORI, R. BERTACCO, AND F. CICCACCI, *Magnetization reversal properties of $Fe/NiO/Fe(001)$ trilayers*, Physical Review B, 72 (2005), p. 144402. 122
- [19] M. BRÜCHE, *Zeitschrift für Naturforschung*, 11 (1934), p. 287. 43
- [20] J. CALLAWAY, *Quantum Theory of the Solid State*, Academic Press Inc., Boston, 1977. 3, 8

- [21] J. CAMARERO, Y. PENNEC, J. VOGEL, M. BONFIM, S. PIZZINI, F. ERNULT, F. FETTAR, F. GARCIA, F. LANCON, L. BILLARD, B. DIENY, A. TAGLIAFERRI, AND N. B. BROOKES, *Perpendicular Interlayer Coupling in $Ni_{80}Fe_{20}/NiO/Co$ Trilayers*, Physical Review Letters, 91 (2003), p. 027201. 121, 124, 127
- [22] M. J. CAREY AND A. E. BERKOWITZ, *Exchange anisotropy in coupled films of $Ni_{81}Fe_{19}$ with NiO and $Co_xNi_{1-x}O$* , Applied Physics Letters, 60 (1992), p. 3060. 86
- [23] P. CARRA, *X-ray natural circular dichroism*. <http://www.esrf.eu/UsersAndScience/Publications/Highlights/1999/magnetism/xncd.html>, 2007. 11
- [24] P. CARRA, B. T. THOLE, M. ALTARELLI, AND X. WANG, *X-ray circular dichroism and local magnetic fields*, Physical Review Letters, 70 (1993), p. 694. 16
- [25] B. CARTER-STIGLITZ, B. MOSKOWITZ, AND P. SOLHEID, *Fe_3O_4 smoked at 80K*, The IRM Quarterly, 15 (2005), pp. 1–12. 95
- [26] C. T. CHEN, Y. U. IDZERDA, H.-J. LIN, N. V. SMITH, G. MEIGS, E. CHABAN, G. H. HO, E. PELLEGRIN, AND F. SETTE, *Experimental confirmation of the x-ray magnetic circular dichroism sum rules for iron and cobalt*, Physical Review Letters, 75 (1995), p. 152. 16
- [27] C. T. CHEN, F. SETTE, Y. MA, AND S. MODESTI, *Soft x-ray magnetic circular dichroism at the $L_{2,3}$ edges of nickel*, Physical Review B - Rapid Communications, 42 (1990), p. 7262. 65
- [28] R. D. COWAN, *The Theory of Atomic Structure and Spectra*, UCLA Press, Berkeley, 1981. 13
- [29] S. CRAMM, *Synchrotron Radiation Sources and Beamlines: Overview*, in Probing the Nanoworld - IFF Spring School 2007, vol. 38, Jülich, 2007. 41
- [30] J. CROCOMBETTE, M. POLLAK, F. JOLLET, N. THROMAT, AND M. GAUTIER-SOYER, *X-ray-absorption spectroscopy at the $Fe L(2,3)$ threshold in iron-oxides*, Phys. Rev. B, 52 (1995), pp. 3143–3150. 93
- [31] S. I. CSISZAR, M. W. HAVERKORT, Z. HU, A. TANAKA, H. H. HSIEH, H. J. LIN, C. T. CHEN, T. HIBMA, AND L. H. TJENG, *Controlling orbital moment and spin orientation in CoO layers by strain*, Physical Review Letters, 95 (2005), p. 187205. 24, 55

- [32] S. CZEKAJ, F. NOLTING, L. J. HEYDERMAN, P. R. WILLMOTT, AND G. VAN DER LAAN, *Sign dependence of the x-ray magnetic linear dichroism on the antiferromagnetic spin axis in LaFeO₃ thin films*, Phys. Rev. B - Rapid Comm., 73 (2006), p. 020401(R). xviii, 31, 112, 125
- [33] A. L. DE BRITO AND T. P. EGGARTER, *Two useful identities involving spherical harmonics*, International Journal of Quantum Chemistry, 17 (1980), pp. 459–65. 13
- [34] *Desy milestones*. published on zms.desy.de. 41
- [35] S. S. DHESI, G. VAN DER LAAN, E. DUDZIK, AND A. B. SHICK, *Anisotropic spin-orbit coupling and magnetocrystalline anisotropy in Vicinal Co Films*, Phys. Rev. Lett., 87 (2001), p. 067201. 24
- [36] F. DÖRFLER, *X-ray Magnetic Dichroism*, PhD thesis, Stuttgart, 2006. 3, 8, 16
- [37] I. DZYALOSHINSKY, *A thermodynamic theory of "weak" ferromagnetism of antiferromagnetics*, Journal of Physics and Chemistry in Solids, 4 (1958), p. 241. xvii, 40, 47
- [38] F. ERNULT, B. DIENY, AND J. R. REGNARD, *Experimental study of the coupling between two ferromagnetic layers through an antiferromagnetic spacer*, Journal of Magnetism and Magnetic Materials, 242-5 (2002), pp. 515–7. 127
- [39] J. L. ERSKINE AND E. A. STERN, *Calculation of the M₂₃ magneto-optical absorption spectrum of ferromagnetic nickel*, Phys. Rev. B, 12 (1975), pp. 5016–5024. 11
- [40] P. G. EVANS, E. D. ISAACS, G. AEPPLI, Z. CAI, AND B. LAI, *X-ray microdiffraction images of antiferromagnetic domain evolution in chromium*, Science, 295 (2002), pp. 1042–5. 111
- [41] A. EVERY AND A. MCCURDY, *Elastic constants of cubic systems - binary compounds*, in Landolt Börnstein, vol. 29a, Springer, Berlin, 1992. 132
- [42] M. FINAZZI, *Interface coupling in a ferromagnet/antiferromagnet bilayer*, Phys. Rev. B, 69 (2004), p. 064405. 53, 54, 80
- [43] M. FINAZZI AND S. ALTIERI, *Magnetic dipolar anisotropy in strained antiferromagnetic films*, Phys. Rev. B, 68 (2003), p. 054420. 89, 99
- [44] M. FINAZZI, A. BRAMBILLA, P. BIAGIONI, J. GRAF, G.-H. GWEON, A. SCHOLL, A. LANZARA, AND L. DUÒ, *Interface coupling transition in a thin epitaxial antiferromagnetic film interacting with a ferromagnetic substrate*, Phys. Rev. Lett., 97 (2006), p. 097202. 107, 108

- [45] M. R. FITZSIMMONS, C. LEIGHTON, J. NOGUÉS, A. HOFFMANN, K. LIU, C. F. MAJKRZAK, J. A. DURA, J. R. GROVES, R. W. SPRINGER, P. N. ARENDT, V. LEINER, H. LAUTER, AND I. K. SCHULLER, *Influence of in-plane crystalline quality of an antiferromagnet on perpendicular exchange coupling and exchange bias*, Phys. Rev. B, 65 (2002), p. 134436. 53, 54
- [46] T. FLIESSBACH, *Elektrodynamik*, Spektrum, Heidelberg, 1997. 29, 41
- [47] J. FRIEDEL, P. LENGART, AND G. LEMAN, *Etude du couplage spin-orbite dans les métaux de transition. Application au platine*, J. Phys. Chem. Sol., 25 (1964), pp. 781–800. 24
- [48] J. FUJII, F. BORGATTI, G. PANACCIONE, M. HOCHSTRASSER, F. MACCHEROZZI, G. ROSSI, AND G. VAN DER LAAN, *Evidence for in-plane spin-flop orientation at the MnPt/Fe (100) interface revealed by x-ray magnetic linear dichroism*, Phys. Rev. B, 73 (2006), p. 214444. 74
- [49] J. GARCIA AND G. SUBIAS, *The Verwey transition - a new perspective*, JOURNAL OF PHYSICS-CONDENSED MATTER, 16 (2004), pp. R145–R178. 39
- [50] E. GOERING, S. GOLD, M. LAFKIOTI, AND G. SCHUTZ, *Vanishing Fe 3d orbital moments in single-crystalline magnetite*, Europhys. Lett., 73 (2006), pp. 97–103. 39, 85, 87, 95, 118
- [51] H. GOMONAJ. private communication. 75
- [52] H. V. GOMONAY AND V. M. LOKTEV, *Shape-induced phenomena in finite-size antiferromagnets*, Physical Review B, 75 (2007), p. 174439. 55, 112
- [53] A. GORTON, B. G., AND T. L. JOSEPH, *Thermal expansion coefficients for iron and its oxides from x-ray diffraction measurements at elevated temperatures*, Transactions of the metallurgical society of AIME, 233 (1965), p. 1519. 39
- [54] S. GOTA, M. GAUTIER-SOYER, AND M. SACCHI, *Fe 2p absorption in magnetic oxides: Quantifying angular-dependent saturation effects*, PHYSICAL REVIEW B, 62 (2000), pp. 4187–90. 118
- [55] J. GOULON, C. GOULON-GINET, A. ROGALEV, G. BENAYOUN, C. MALGRANGE, AND C. BROUDER, *X-ray natural circular dichroism (XNCD) in gyrotropic crystals (Proceedings Paper)*, SPIE Proceedings, 3773 (1999), pp. 316–25. 11

- [56] P. GRÜNBERG, R. SCHREIBER, Y. PANG, M. B. BRODSKY, AND H. SOWERS, *Layered Magnetic Structures: Evidence for Antiferromagnetic Coupling of Fe Layers across Cr Interlayers*, Physical Review Letters, 57 (1986), pp. 2442–5. xvi
- [57] M. GRUYTERS, *Structural and magnetic properties of transition metal oxide/metal bilayers prepared by in situ oxidation*, Journal of Magnetism and Magnetic Materials, 248 (2002), pp. 248–57. 86
- [58] J. GUTENBERG, ed., *The Gutenberg Bible (digital version of the original)*, Gutenberg, J., 1450. xv
- [59] M. HAVERKORT, *private communication*. 31
- [60] M. W. HAVERKORT, S. I. CSISZAR, Z. HU, S. ALTIERI, A. TANAKA, H. H. HSIEH, H. J. LIN, C. T. CHEN, T. HIBMA, AND L. H. TJENG, *Magnetic versus crystal-field linear dichroism in NiO thin films*, Phys. Rev. B - Rapid Comm., 69 (2004), p. 020408(R). 20, 21, 55, 67, 69, 89, 99, 113
- [61] B. HEINRICH, Z. CELINSKI, J. F. COCHRAN, A. S. ARROTT, K. MYRTLE, AND S. T. PURCELL, *Bilinear and biquadratic exchange coupling in bcc Fe/Cu/Fe trilayers: Ferromagnetic-resonance and surface magneto-optical Kerr-effect studies*, Phys. Rev. B, 47 (1993), pp. 5077–5089. 121
- [62] F. U. HILLEBRECHT, H. OHLDAG, N. B. WEBER, C. BETHKE, U. MICK, M. WEISS, AND J. BAHRDT, *Magnetic moments at the surface of antiferromagnetic NiO(100)*, Phys. Rev. Lett., 86 (2001), p. 3419. 112
- [63] L. L. HINCHEY AND D. L. MILLS, *Magnetic properties of ferromagnet-antiferromagnet superlattice structures with mixed-spin antiferromagnetic sheets*, Physical Review B, 34 (1986), pp. 1689–99. 52
- [64] A. HOFFMANN, *Symmetry driven irreversibilities at ferromagnetic-antiferromagnetic interfaces*, Physical Review Letters, 93 (2004), p. 097203. 54
- [65] Y. IJIRI, J. BORCHERS, R. ERWIN, S. LEE, P. VAN DER ZAAG, AND R. WOLF, *Role of the antiferromagnet in exchange-biased Fe₃O₄/CoO superlattices*, Journal of Applied Physics, 83 (1998), pp. 6882–7. 96, 111
- [66] Y. IJIRI, J. A. BORCHERS, R. W. ERWIN, S. H. LEE, P. J. VAN DER ZAAG, AND R. M. WOLF, *Perpendicular coupling in exchange-biased Fe₃O₄/CoO superlattices*, Phys. Rev. Lett., 80 (1998), pp. 608–611. 96, 111

- [67] R. JANSEN, V. A. M. BRABERS, AND H. VAN KEMPEN, *One-dimensional reconstruction observed on $Fe_3O_4(110)$ by scanning tunneling microscopy*, Surface Science, 3 (1995), pp. 237–47. 59, 108, 109, 119
- [68] P. J. JENSEN, H. DREYSSÉ, AND M. KIWI, *Magnetic reordering in the vicinity of a ferromagnetic/antiferromagnetic interface*, Eur. J. Phys. B, 46 (2005), pp. 541–551. 54, 80, 91
- [69] R. JUNGLUT, R. COEHOORN, M. T. JOHNSON, C. SAUER, P. J. VAN DER ZAAG, A. R. BALL, T. G. S. M. RIJKS, J. AAN DE STEGGE, AND A. REINDERS, *Exchange biasing in MBE-grown $Ni_{80}Fe_{20}/Fe_{50}Mn_{50}$ bilayers*, Journal of Magnetism and Magnetic Materials, 148 (1995), pp. 300–6. 52
- [70] C. KIM AND Y. C. CHUNG, *First-principles calculations on magnetic properties of interface-rippled $Co/\alpha-Al_2O_3/Co$* , Applied Physics Letters, 88 (2006), p. 132512. 47
- [71] S. J. KIM, W. C. KIM, C. S. KIM, AND S. W. LEE, *Mossbauer studies of superexchange interactions in $NiFe_2O_4$* , J. Kor. Phys. Soc., 36 (2000), pp. 430–434. 107
- [72] M. KIWI, *Origin of the magnetic proximity effect*, Mat. Res. Soc. Symp. Proc., 746 (2003), pp. Q.5.2.1–11. 47, 89, 90
- [73] G. D. KLAPEL AND P. N. SHIVE, *High-temperature magnetostriction of magnetite*, J. Geophys. Res., 79 (1974), p. 2629. 106, 130, 132
- [74] H. KONDOH AND T. TAKEDA, *Observation of antiferromagnetic domains in Nickel Oxide*, Journal of the Physical Society of Japan, 19 (1964), pp. 2041–51. 36
- [75] N. C. KOON, *Calculations of exchange bias in thin films with ferromagnetic/antiferromagnetic interfaces*, Phys. Rev. Lett., 78 (1997), p. 4865. xix, 74, 90, 104, 123, 125
- [76] S. KRISHNAKUMAR, M. LIBERATI, C. GRAZIOLI, M. VERONESE, S. TURCHINI, P. LUCHES, V. S., AND C. CARBONE, *Magnetic linear dichroism studies of in situ grown NiO thin films*, J. Magn. Magn. Mat., 310 (2007), pp. 8–12. 107, 108
- [77] I. KRUG, U. HILLEBRECHT, H. GOMONAJ, M. HAVERKORT, A. TANAKA, L. H. TJENG, AND C. M. SCHNEIDER, submitted to EPL, (2007). 31, 118, 122, 123
- [78] I. KRUG AND *et al.* submitted to PRB. 96

- [79] ——. the detailed discussion of this issue exceeds the scope of this article and will be published separately. 106
- [80] I. P. KRUG, F. U. HILLEBRECHT, AND F. NOLTING, *PEEM imaging of antiferromagnetic domain walls in single crystalline nickel oxide*, SLS Annual Reports, (2003). 112
- [81] P. KUIPER, B. G. SEARLE, P. RUDOLF, L. H. TJENG, AND C. T. CHEN, *X-ray magnetic dichroism of antiferromagnet Fe_2O_3 : The orientation of magnetic moments observed by Fe 2p x-ray absorption spectroscopy*, Physical Review Letters, 70 (1993), p. 1549. 21
- [82] J. KUNES AND P. M. OPPENEER, *Anisotropic x-ray magnetic linear dichroism at the $L_{2,3}$ edges of cubic Fe, Co, and Ni: Ab initio calculations and model theory*, Phys. Rev. B, 67 (2003), p. 024431. xviii, 22, 26, 28, 31, 112, 125
- [83] J. KUNEŠ, P. M. OPPENEER, S. VALENCIA, D. ABRAMSOHN, H.-C. MERTINS, W. GUDAT, M. HECKER, AND C. SCHNEIDER, *Understanding the XMLD and its magnetocrystalline anisotropy at the L 2,3-edges of 3d transition metals*, J. Magn. and Magn. Mat., 272-6 (2004), pp. 2146–7. 27, 31, 112, 125
- [84] R. J. LAD AND H. V. E., *Structure of α - Fe_2O_3 single crystal surfaces following Ar^+ ion bombardment and annealing in O_2* , Surf. Sci., 193 (1988), p. 81. 91
- [85] C. H. LAI, T. MING, R. ERWIN, AND J. BORCHERS, *Exchange anisotropy between single twin domain NiO and NiFe*, J. Appl Phys., 91 (2002), pp. 7751–3. 104
- [86] V. K. LAZAROV, M. WEINERT, S. A. CHAMBERS, AND M. GAJDARDZISKA-JOSIFOVSKA, *Atomic and electronic structure of the $Fe_3O_4(111)/MgO(111)$ model polar oxide interface*, Physical Review B, 72 (2005), p. 195401. 47, 96
- [87] R. LEFEVER, *$Fe^{2+}Fe^{3+}$ spinels*, in Part B: Spinels, Fe Oxides, and Fe-Me-O Compounds, vol. 12b, Springer, 0000, p. 58. 40, 86
- [88] ———, *Wüstite $Fe_{1-x}O$ and wüstite with substitutions*, vol. 4a, Springer, Berlin, 0000, pp. 3–7. 40
- [89] P. T. LEUNG, *A note on the 'system-free' expressions of Maxwell's equations*, European Journal of Physics, 25 (2004), pp. N1–4. 133

- [90] Z. Y. LIU AND S. ADENWALLA, *Closely linear temperature dependence of exchange bias and coercivity in out-of-plane exchange-biased [Pt/Co](3)/NiO(11 angstrom) multilayer*, Journal of Applied Physics, 94 (2003), pp. 1105–9. 86
- [91] Z. Y. LIU, L. YUE, D. J. KEAVNEY, AND S. ADENWALLA, *Oscillatory interlayer exchange coupling in [Pt/Co]_n/NiO/[Co/Pt]_n multilayers with perpendicular anisotropy: Dependence on NiO and Pt layer thicknesses*, Physical Review B (Condensed Matter and Materials Physics), 70 (2004), p. 224423. 127
- [92] A. P. MALOZEMOFF, *Random-field model of exchange anisotropy at rough ferromagnetic-antiferromagnetic interfaces*, Physical Review B, 35 (1987), pp. 3679–82. 50
- [93] G. MARIOTTO, S. MURPHY, AND I. V. SHVETS, *Charge ordering on the surface of Fe₃O₄(001)*, Physical Review B, 66 (2002), p. 245426. 95
- [94] G. K. L. MARX, H. J. ELMERS, AND G. SCHÖNHENSE, *Magneto-optical linear dichroism in threshold photoemission electron microscopy of polycrystalline Fe films*, Phys. Rev. Lett., 84 (2000), pp. 5888–5891. 45
- [95] M. MARYNOWSKI, W. FRANZEN, AND M. EL-BATANOUNY, *Observation of an extraordinary antiferromagnetic transition on the NiO(100) surface by metastable helium atom diffraction*, Physical Review B, 60 (1999), pp. 6053–67. 35, 60
- [96] D. MAURI, H. C. SIEGMANN, B. P. S., AND E. KAY, *Simple-model for thin ferromagnetic-films exchange coupled to an antiferromagnetic substrate*, J. Appl. Phys., 62 (1987), pp. 3047–9. 49
- [97] W. H. MEIKLEJOHN AND C. P. BEAN, *New magnetic anisotropy*, Physical Review, 105 (1957), pp. 904–13. xvi
- [98] H.-C. MERTINS, P. M. OPPENEER, J. KUNEŠ, A. GAUPP, D. ABRAMSOHN, AND F. SCHÄFERS, *Observation of the x-ray magneto-optical Voigt effect*, Phys. Rev. Lett., 87 (2001), p. 047401. 23
- [99] D. L. MILLS, *Surface effects in magnetic crystals near the ordering temperature*, Physical Review B, 3 (1971), pp. 3887–95. 84
- [100] T. J. MORAN, J. NOGUÉS, D. LEDERMAN, AND I. K. SCHULLER, *Perpendicular coupling at Fe-FeF₂ interfaces*, Appl. Phys. Lett., 72 (1998), p. 617. 52, 55
- [101] T. MORIYA, *Anisotropic superexchange interaction and weak ferromagnetism*, Physical Review, 120 (1960), p. 91. 40, 47

- [102] S. MURPHY, S. F. CEBALLOS, G. MARIOTTO, N. BERDUNOV, K. JORDAN, S. I. V., AND Y. M. MUKOVSKII, *Atomic scale spin-dependent STM on magnetite using antiferromagnetic STM tips*, *Microsc. Res. Techn.*, 66 (2005), pp. 85–92. 94
- [103] K. NAKAHIGASHI, N. FUKUOKA, AND Y. SHIMOMURA, *Crystal-structure of antiferromagnetic NiO determined by x-ray topography*, *Journal of the Physical Society of Japan*, 38 (1975), pp. 1634–1640. 35, 36
- [104] R. NAKAJIMA, *X-ray magnetic circular dichroism spectroscopy in transition metal thin films*, PhD thesis, Stanford, 1998. 16
- [105] K. NAMIKAWA, *LEED investigation on temperature-dependence of sublattice magnetization of NiO (001) surface-layers*, *Journal of the Physical Society of Japan*, 44 (1978), pp. 165–171. 84
- [106] J. NOGUES, T. J. MORAN, D. LEDERMAN, I. K. SCHULLER, AND K. V. RAO, *Role of interfacial structure on exchange-biased FeF₂-Fe*, *Phys. Rev. B*, 59 (1999), pp. 6984–6993. 89
- [107] J. NOGUES AND I. K. SCHULLER, *Exchange bias*, *J. Magn. Magn. Mat.*, 192 (1999), pp. 203–232. xvi, 49, 107
- [108] J. NOGUÉS, D. LEDERMAN, T. J. MORAN, I. K. SCHULLER, AND K. V. RAO, *Large exchange bias and its connection to interface structure in FeF₂-Fe bilayers*, *Applied Physics Letters*, 68 (1996), p. 3186. 52
- [109] T. NOYES AND W. E. DICKINSON, *The Random Access Memory Accounting Machine*, *IBM Journal of Research and Development*, 1 (1957), pp. 72–5. xv
- [110] T. OGUCHI AND T. SHISHIDOU, *Anisotropic property of magnetic dipole in bulk, surface, and overlayer systems*, *Physical Review B*, 70 (2004), p. 024412. 18
- [111] H. OHLDAG, H. SHI, E. ARENHOLZ, J. STÖHR, AND D. LEDERMAN, *Parallel versus antiparallel interfacial coupling in exchange biased Co/FeF₂*, *Phys. Rev. Lett.*, 96 (2006), p. 027203. 105
- [112] P. M. OPPENEER, *Magneto-Optical Kerr Spectra*, vol. 13, Elsevier, Amsterdam, 2001. 8
- [113] *The invention of paper*. published on www.Wikipedia.org. xv
- [114] T. G. PHILLIPS AND R. L. WHITE, *Single-ion magnetostriction in the iron group monoxides from the strain dependence of electron-paramagnetic-resonance Spectra*, *Phys. Rev.*, 153 (1967), pp. 616–20. 106, 107, 132

- [115] S. P. POGOSSIAN, D. SPENATO, D. T. DEKADJEVI, AND J. B. YOUSSEF, *Experimental method to determine the misalignment of the easy axis of ferromagnetic and antiferromagnetic films in exchange biased bilayers*, Phys. Rev. B, 73 (2006), p. 174414. 106
- [116] D. L. PORTIGAL AND E. BURSTEIN, *Magneto-spatial dispersion effects on the propagation of electro-magnetic radiation in crystals*, Journal of Physics and Chemistry of Solids, 32 (1971), pp. 603–8. 4
- [117] D. POTHMAN, *History of paper*. published on www.paperhistory.org. xv
- [118] *The history of book printing*. published on www.Wikipedia.org. xv
- [119] X. QIAN AND W. HUBNER, *Symmetry and substrate effects on magnetic interactions from first principles: A comparison between Fe/W(100) and Fe/W(110)*, Phys. Rev. B, 67 (2003), p. 184414. 47, 69, 90
- [120] F. RADU, A. NEFEDOV, J. GRABIS, G. NOWAK, A. BERGMANN, AND H. ZABEL, *Soft x-ray resonant magnetic scattering studies on Fe/CoO exchange bias system*, J. Magn. Magn. Mater., 300 (2006), pp. 206–10. 105
- [121] A. RECNİK, D. L. CARROLL, K. A. SHAW, D. M. LIND, AND M. RUHLE, *Structural characterization of Fe₃O₄-NiO superlattices using high-resolution transmission electron microscopy*, J. Mater. Res., 12 (1997), pp. 2143–2151. 60, 96, 122
- [122] T. J. REGAN, H. OHLDAG, C. STAMM, F. NOLTING, J. LUNING, J. STOHR, AND R. L. WHITE, *Chemical effects at metal/oxide interfaces studied by x-ray-absorption spectroscopy*, Phys. Rev. B, 64 (2001), p. 214422. 103
- [123] H. J. REICHMANN AND S. D. JACOBSEN, *High-pressure elasticity of a natural magnetite crystal*, American Mineralogist, 89 (2004), pp. 1061–1066. 132
- [124] W. L. ROTH, *Neutron and optical studies of domains in NiO*, J. Appl. Phys., 31 (1960), p. 2000. 104
- [125] S. ROY, M. R. FITZSIMMONS, S. PARK, M. DORN, O. PETRACIC, I. V. ROSHCHIN, Z.-P. LI, X. BATLLE, R. MORALES, A. MISRA, X. ZHANG, K. CHESNEL, J. B. KORTRIGHT, S. K. SINHA, AND I. K. SCHULLER, *Depth profile of uncompensated spins in an exchange bias system*, Phys. Rev. Lett., 95 (2005), p. 047201. 50
- [126] S. SAITO, M. MIURA, AND K. KUROSAWA, *Magnetic torque measurements on NiO (111) platelets*, Journal of Physics C: Solid State Physics, 13 (1980), pp. 1521–7. 104

- [127] D. SANDER, *The correlation between mechanical stress and magnetic anisotropy in ultrathin films*, Rep. Prog. Phys., 62 (1999), pp. 809–58. 104, 107, 129, 131
- [128] S. SASAKI, K. KAKUNO, T. TAKADA, T. SHIMADA, K. YANAGIDA, AND Y. MIYAHARA, *Design of a new type of planar undulator for generating variably polarized radiation*, Nuclear Instruments and Methods in Physics Research A, 331 (1993), pp. 763–7. 42
- [129] F. SCHEDIN, E. W. HILL, G. VAN DER LAAN, AND G. THORNTON, *Magnetic properties of stoichiometric and nonstoichiometric ultrathin $Fe_3O_4(111)$ films on $Al_2O_3(0001)$* , J. Appl. Phys., 96 (2004), pp. 1165–9. 60, 61, 91, 94
- [130] C. SCHNEIDER, O. DE HAAS, U. MUSCHIOL, N. CRAMER, A. OELSNER, AND M. KLAIS, *Photoemission microscopy from magnetically coupled thin films*, Journal of Magnetism and Magnetic Materials, 233 (2001), pp. 14–20. 42
- [131] C. M. SCHNEIDER, *Electron Emission and Photoemission Microscopy*, in Probing the Nanoworld - IFF Spring School 2007, vol. 38, Research Centre Jülich, Jülich, 2007. 42, 44
- [132] A. SCHOLL, M. LIBERATI, E. ARENHOLZ, H. OHLDAG, AND J. STOHR, *Creation of an antiferromagnetic exchange spring*, Phys. Rev. Lett., 92 (2004), p. 247201. 50
- [133] I. K. SCHULLER AND G. GÜNTHERODT, *The Exchange-Bias Manifesto*, 2002. xvi
- [134] T. C. SCHULTHESS AND W. H. BUTLER, *Consequences of spin-flop coupling in exchange biased films*, Phys. Rev. Lett., 81 (1998), pp. 4516–4519. 53
- [135] G. SCHÜTZ, W. WAGNER, W. WILHELM, P. KIENLE, R. ZELLER, R. FRAHM, AND G. MATERLIK, *Absorption of circularly polarized x rays in iron*, Phys. Rev. Lett., 58 (1987), pp. 737–740. 11
- [136] F. SCHWABL, *Quantenmechanik I*, Springer, Berlin, 1998. 14
- [137] M. M. SCHWICKERT, G. Y. GUO, M. A. TOMAZ, W. L. O'BRIEN, AND G. R. HARP, *X-ray magnetic linear dichroism in absorption at the L edge of metallic Co, Fe, Cr, and V*, Physical Review B - Rapid Communications, 58 (1998), p. R4292. 21, 22

- [138] J. SCHWITALLA AND H. EBERT, *Electron Core-Hole Interaction in the X-Ray Absorption Spectroscopy of 3d Transition Metals*, Phys. Rev. Lett., 80 (1998), pp. 4586–4589. 18
- [139] M. S. SEEHRA AND T. M. GIEBULTOWICZ, *Magnetic structures of fcc systems with nearest-neighbor and next-nearest-neighbor exchange interactions*, Physical Review B, 38 (1988), pp. 11898–900. 36
- [140] G. A. SLACK, *Crystallography and domain walls in antiferromagnetic NiO crystals*, Journal of Applied Physics, 31 (1960), p. 1571. 36, 104
- [141] J. C. SLONCZEWSKI, *Fluctuation mechanism for biquadratic exchange coupling in magnetic multilayers*, Physical Review Letters, 67 (1991), pp. 3172–5. 120, 124, 127
- [142] —, *Origin of biquadratic exchange in magnetic multilayers*, Journal of Applied Physics, 73 (1993), pp. 5957–62. 120
- [143] —, *Overview of interlayer exchange theory*, Journal of Magnetism and Magnetic Materials, 150 (1995), pp. 13–74. 120
- [144] J. C. A. SLONCZEWSKI, *Conductance and exchange coupling of two ferromagnets separated by a tunneling barrier*, Physical Review B, 39 (1989), pp. 6995–7002. 120
- [145] A. B. SMITH AND R. V. JONES, *Magnetostriction in Nickel ferrite and Cobalt-Nickel ferrite*, J. Appl. Phys., 37 (1966), pp. 1001–2. 106, 132
- [146] P. V. SMITH, *The inclusion of spin-orbit interaction into the electronic structure of dilute transitional impurities in transition metal hosts*, Journal of Physics F: Metal Physics, 11 (1981), pp. 1063–73. 24
- [147] D. SPANKE, V. SOLINUS, D. KNABBEN, F. U. HILLEBRECHT, F. CICCACCI, L. GREGORATTI, AND M. MARSÌ, *Evidence for in-plane antiferromagnetic domains in ultrathin NiO films*, Physical Review B, 58 (1998), pp. 5201–4. 112
- [148] G. SRINIVASAN AND M. S. SEEHRA, *Magnetic susceptibilities, their temperature variation, and exchange constants of NiO*, Physical Review B, 29 (1984), pp. 6295–8. 35
- [149] J. STÖHR, *Exploring the microscopic origin of magnetic anisotropies with x-ray magnetic circular dichroism (XMCD) spectroscopy*, Journal of Magnetism and Magnetic Materials, 200 (1999), pp. 470–97. 78
- [150] J. STÖHR AND H. KÖNIG, *Determination of spin- and orbital-moment anisotropies in transition metals by angle-dependent x-ray magnetic circular dichroism*, Physical Review Letters, 75 (1995), p. 3748. 16, 18, 62

- [151] J. STÖHR AND H. C. SIEGMANN, *Magnetism - From Fundamentals to Nanoscale Dynamics*, Springer, Berlin, 2006. xv, 19, 27, 35, 41, 42, 114
- [152] P. E. TANNENWALD AND R. WEBER, *Exchange Integral in Cobalt from Spin-Wave Resonance*, Physical Review, 131 (1961), p. 715. 49
- [153] B. T. THOLE, P. CARRA, F. SETTE, AND G. VAN DER LAAN, *X-ray circular dichroism as a probe of orbital magnetization*, Physical Review Letters, 68 (1992), p. 1943. 16
- [154] B. T. THOLE, G. VAN DER LAAN, AND G. A. SAWATZKY, *Strong Magnetic Dichroism Predicted in the $M_{4,5}$ X-Ray Absorption Spectra of Magnetic Rare-Earth Materials*, Physical Review Letters, 55 (1985), pp. 2086–88. 21, 84
- [155] R. TYER, G. VAN DER LAAN, W. M. TEMMERMAN, Z. SZOTEK, AND H. EBERT, *Systematic theoretical study of the spin and orbital magnetic moments of 4d and 5d interfaces with Fe films*, Phys. Rev. B, 67 (2003), p. 104409. 47
- [156] UNKNOWN, *Timeline of Electricity and Magnetism: Introduction*. Website of the magnetic high-field laboratory, State University Florida, 1995. xv
- [157] N. A. USOV AND S. A. GUDOSHNIKOV, *Numerical simulation of magnetization process in antiferromagnetic-ferromagnetic bilayer with compensated interface*, J. Magn. Magn. Mat., 300 (2006), pp. 164–9. 53
- [158] P. A. A. VAN DER HEIJDEN, C. H. W. SWÜSTE, AND W. J. M. DE JONGE, *Evidence for roughness driven 90° coupling in $Fe_3O_4/NiO/Fe_3O_4$ trilayers*, Physical Review Letters, 5 (1999), p. 1020. 122, 124, 127
- [159] G. VAN DER LAAN, *Magnetic linear x-ray dichroism as a probe of the magnetocrystalline anisotropy*, Physical Review Letters, 82 (1999), pp. 640–4. 24, 28
- [160] G. VAN DER LAAN, C. M. B. HENDERSON, R. A. D. PATTRICK, S. S. DHESI, P. F. SCHOFIELD, E. DUDZIK, AND D. J. VAUGHAN, *Orbital polarization in $NiFe_2O_4$ measured by Ni-2p x-ray magnetic circular dichroism*, Phys. Rev. B, 59 (1999), p. 4314. 65, 66, 78, 80, 87
- [161] G. VAN DER LAAN, B. THOLE, G. A. SAWATZKY, J. B. GOEDKOOP, J. C. FUGGLE, J.-M. ESTEVA, R. KARNATAK, J. P. REMEIKA, AND H. A. DABKOWSKA, *Experimental proof of magnetic x-ray dichroism*, Physical Review B, 34 (1986), p. 6529. 21

- [162] G. VAN DER LAAN AND B. T. THOLE, *Local probe for spin-orbit interaction*, Physical Review Letters, 60 (1988), pp. 1977–80. 10
- [163] P. J. VAN DER ZAAG, Y. IJIRI, J. A. BORCHERS, L. F. FEINER, R. M. WOLF, J. M. GAINES, R. W. ERWIN, AND M. A. VERHEIJEN, *Difference between blocking and Néel temperatures in the exchange biased Fe_3O_4/CoO System*, Physical Review Letters, 84 (2000), p. 6102. 86
- [164] J. VOGEL, *NO_2 -assisted molecular beam epitaxy of iron oxide films*, 1998. 40
- [165] F. WALZ, *The Verwey transition - a topical review*, Journal of Physics: Condensed Matter, 14 (2002), pp. R285–R340. 39
- [166] H. Q. WANG, W. GAO, E. I. ALTMAN, AND V. E. HENRICH, *Studies of the electronic structure at the Fe_3O_4-NiO interface*, J. Vac. Sci. Technol. A, 22 (2004), pp. 1675–81. 96, 122
- [167] N. B. WEBER, H. OHLDAG, H. GOMONAJ, AND F. HILLEBRECHT, *Magnetostrictive domain walls in antiferromagnetic NiO* , Phys. Rev. Lett., 91 (2003), p. 237205. 37, 39, 112, 127
- [168] L. WEE, R. L. STAMPS, L. MALKINSKI, Z. CELINSKI, AND D. SKRZYPEK, *Thermal training of exchange bias in epitaxial $Fe/KNiF_3$* , Physical Review B (Condensed Matter and Materials Physics), 69 (2004), p. 134425. 84
- [169] P. WEISS AND R. FORRER, Ann. Phys. (Paris), 12 (1929), p. 279. 39
- [170] D. WELLER, J. STÖHR, R. NAKAJIMA, A. CARL, M. G. SAMANT, C. CHAPPERT, R. MÉGY, P. BEAUVILLAIN, P. VEILLET, AND G. A. HELD, *Microscopic origin of magnetic anisotropy in $Au/Co/Au$ probed with X-Ray Magnetic Circular Dichroism*, Physical Review Letters, 75 (1995), pp. 3752–55. 47
- [171] T. YAMADA, *Antiferromagnetic domain walls in Nickel Oxide*, J. Phys. Soc. Jpn., 18 (1963), p. 520. 37, 38, 104, 112
- [172] —, *Magnetic anisotropy, magnetostriction, and magnetic domain walls in NiO . I. Theory*, J. Phys. Soc. Jpn., 21 (1966), pp. 664–71. 38, 71, 104, 112
- [173] —, *Spin configuration in antiferromagnetic domain walls of the NiO -type crystals*, J. Phys. Soc. Jpn., 21 (1966), p. 650. 38, 112
- [174] T. YAMADA, S. SAITO, AND Y. SHIMOMURA, *Magnetic anisotropy, magnetostriction, and magnetic domain walls in NiO . II. Experiment*, J. Phys. Soc. Jpn., 21 (1966), pp. 672–80. 38, 71, 104

-
- [175] F. Y. YANG AND C. L. CHIEN, *Spiraling spin structure in an exchange-coupled antiferromagnetic layer*, Physical Review Letters, 85 (2000), pp. 2597–600. 50
- [176] A. T. YOUNG, E. ARENHOLZ, S. MARKS, R. SCHLUETER, C. STEIER, H. A. PADMORE, A. P. HITCHCOCK, AND D. G. CASTNER, *A soft x-ray undulator beamline at the Advanced Light Source with circular and variable linear polarization for the spectroscopy and microscopy of magnetic materials.*, Journal of Synchrotron Radiation, 9 (2002), p. 270. 42
- [177] O. ÖZDEMİR, S. XU, AND D. J. DUNLOP, *Closure domains in magnetite*, J. Geophys. Res.-Sol. Ea., 100 (1995), pp. 2193–2209. 92, 94, 104, 118

Danksagung

An dieser Stelle möchte ich allen danken, die auf verschiedenste Weise zum Gelingen meiner Dissertation beigetragen haben

Herrn PROF. CLAUS MICHAEL SCHNEIDER möchte ich für die Motivation und Unterstützung danken, die ich von ihm während meiner Zeit in Jülich erhalten habe. Ich bin ihm überaus verbunden für die Möglichkeit, dass ich zusammen mit Ulrich Hillebrecht von Karlsruhe nach Jülich wechseln konnte.

In Dankbarkeit blicke ich zurück auf die Zeit mit PRIV.-DOZ. DR. FRANZ ULRICH HILLEBRECHT, der mir seit Beginn meiner Doktorarbeit als Mentor zur Seite stand. Ich habe die Arbeit mit ihm, die vielen Diskussionen und Anregungen sehr geschätzt. Heute haben viele Dinge, die wir gemeinsam begonnen haben, Früchte getragen, und ich wünschte mir sehr, er könnte all das noch erleben. Am meisten vermisse ich seinen Humor – sein schmetterndes „Bon Giorno!“ und die kleinen „Injektions-Pausen“ bei Messzeiten („Lust auf a Kafeetscherl?“), wo wir uns über Gott und die Welt unterhielten (meistens das letztere), oder uns gegenseitig unser Elend klarmachten, wenn’s Probleme gab („Yo mei, des is a Graiz, Geh!“). Uli war weder Italiener noch Österreicher oder Bayer, aber seine Intonationen waren stets authentisch! Ganz zu schweigen von seinem Hamburger Original-Akzent („Büschn schaddich hoite!“). Und wenn die Messung mal wirklich nicht mehr zu retten war, bewies er Optimismus und konstatierte „Let’s declare victory and go home!“.

DR. MAURITS HAVERKORT gilt mein ganz besonderer Dank: Nachdem die Auswertung meiner experimentellen Domänenwandprofile mittels isotropem XMLD fehlschlug, wurde mir schnell klar, dass eine völlig neue Herangehensweise für die Auswertung notwendig war. Für vektorielle Magnetometrie muss die vollständige Winkelabhängigkeit des – wie sich herausstellte – anisotropen XMLD bekannt sein. Glücklicherweise erklärte Maurits sich bereit, Atomare Multiplettrechnungen für verschiedene Spin-Quantisierungsachsen durchzuführen – und kam auch gleich mit einer Formel daher, was mehr war als ich mir erhofft hatte. Letztere erwies sich für meine Auswertung von größtem Wert, da sie es nunmehr ermöglichte, auch in einkristallinen Systemen die Orientierung der Spinachse zu ermitteln. In den darauffolgenden Diskussionen mit Maurits habe ich sehr viel dazugelernt, und die Arbeit mit ihm hat jede Menge Spaß gemacht.

PROF. PAUL BECHTHOLD möchte ich herzlich danken für die Zeit, die er

dem Lesen meiner Doktorarbeit gewidmet hat, ebenso wie für die fruchtbaren Diskussionen über XAS und Magnetooptik.

Frau PROF. DR. HELEN GOMOMAY danke ich für die vielen Diskussionen und die Hilfe bezüglich theoretischer Modelle des Magnetischen Proximity Effektes. Ferner hat mir ihr seelischer Beistand nach dem Tode Uli's sehr geholfen.

DR. STEFAN CRAMM möchte ich für den live- und Telefonsupport an der UE-56/1 SGM Beamline in Berlin danken. Seine Tipps und Tricks und so manche Diskussion haben die Problemlösung oft enorm beschleunigt. Auch habe ich von ihm zu meiner Beruhigung erfahren, dass Selbstgespräche in einsamen Nachtschichten wohl ganz normal und kein Anzeichen von Wahnsinn sind.

FRITHJOF NOLTING, CHRISTOPH QUITMANN und ARANTXA-FRAILE-RODRÍGUEZ möchte ich für den exorbitant guten Support und die Stabilität der SIM Beamline an der Swiss Light Source danken.

DR. DIANA RATA bin ich dankbar für die Hilfe bei der Schichtdickencharakterisierung mittels XRD, sowie für die Herstellung des Kontakts zu Maurits Haverkort, der sich als wesentlich für meine Arbeit herausstellen sollte.

Unsern Technikern KONRAD BICKMANN und BERND KÜPPER danke ich für die Unterstützung bei Planung und Konstruktion apparativer Dinge. Bernd hat mich außerdem gut beraten bei der Wahl des geeigneten Pfeifentabaks. Die Hausmischung Neumarkt Special" war wirklich gut! HEINZ PFEIFER danke ich für schnelle Hilfe bei elektronischen Problemen. JÜRGEN LAUER bin ich sehr verbunden auf Grund seiner tollen Beamline-Software, die wirklich tadellos funktionierte (wenn's mal hakete, lag's eigentlich immer woanders).

Allen Mitarbeitern, des Forschungszentrums, bei BESSY und an der SLS, denen ich begegnet bin, danke ich für den freundlichen und hilfsbereiten Umgang sowie eine angenehme Arbeitsatmosphäre.

Dem SFB 491 "*Magnetische Heteroschichten*" der Deutschen Forschungsgemeinschaft gilt mein Dank für die teilweise Finanzierung dieses Projektes.

JUTTA GOLLNICK möchte ich für ihre Hilfe bei allen administrativen Fragen danken, außerdem fand ich ihre lustigen Kaffeerunden-Stories sehr bereichernd.

Allen guten Freunden, die da wären FRANK WEBER, JOCHEN MAURER, MONIQUE CASPARY, LISA PETER und ASTRID KRONENBERGER danke ich für ihr Verständnis dafür, dass ich mal für eine Zeit von der Bildfläche

verschwinden musste und „mich ja niemand mehr zu sehen bekam“. Das wird auch wieder besser!

CHRISTIAN KLEIN danke ich besonders für seine moralische Unterstützung auf den letzten Metern meiner Dissertation. Sehr gefreut hat mich auch sein Besuch an der Beamline in Berlin. Auch wenn er bis heute nicht versteht, warum zwei fast identische PEEM Bilder bei mir solche Begeisterung auslösen, hat er doch sofort die essentiell wichtigen Dinge eines X-PEEMers am Synchrotron ausgemacht: Kaffeetasse, UV-Schutzbrille und Gehörschutz. Danke für diese Erkenntnis!

ANJA RABER danke ich für unserer gemeinsame Zeit und die Erkenntnis, dass man seinen Weg gehen muss, auch, wenn es schwer fällt. Am Ende wird alles gut!

meinen Eltern CHRISTEL und GERT KRUG danke ich dafür, dass sie stets für mich da waren, für ihre große Liebe und ihr Verständnis.

Curriculum Vitae

Personal data

Name	Ingo Peter Krug
Birthdate	13.09.1975
Birthplace	St. Wendel
nationality	german

Education

Oct 2004 – Feb 2008	Continuation of PhD at IFF, Research Centre Jülich, date of graduation: February 21st 2008
Dec 2002	Start of PhD phase at IFP, Research Centre Karlsruhe
2001 – 2005	Correspondence studies of Medical Physics and Technology, University of Kaiserslautern, Zentrum für Fernstudien und Universitäre Weiterbildung (ZFUW)
Oct 2001 – Oct 2002	Diploma thesis: <i>Characterization of Ion Beam Patterned Magnetic Layer Systems by Magnetic Force Microscopy</i>
Oct 1996 – Oct 2002	Physics studies at University Kaiserslautern. Qualification: Physics Diploma
1995 – 1996	Civilian Service at the Steyl Mission Congregations branch St. Wendel
Sep 1986 – May 1995	High-school time at Arnold-Janssen-Gymnasium, St. Wendel. Qualification: Abitur (high-school degree)
1982 – 1986	Primary School, St. Wendel

Publications

published

- D. ENGEL, I. KRUG, H. SCHMORANZER, A. EHRESMANN, A. PAETZOLD, K. RÖLL, B. OCKER, W. MAASS, *Alteration of exchange anisotropy and magnetoresistance in Co/Cu/Co/FeMn spin valves by ion bombardment*, J. of App. Phy., **94** (2003) pp. 5925-9.
- A. EHRESMANN, I. KRUG, A. KRONENBERGER; A. EHLERS AND D. ENGEL, *In-plane magnetic pattern separation in NiFe/NiO and Co/NiO exchange biased bilayers investigated by magnetic force microscopy*, J. Magn. Mat. **280** (2004) pp. 369-76
- F. WEGELIN, D. VALDAITSEV, A. KRASYUK, S. A. NEPIJKO, G. SCHÖNHENSE, H. J. ELMERS, I. KRUG, AND C. M. SCHNEIDER, *Magnetization dynamics in microscopic spin-valve elements: Shortcomings of the macrospin picture*, Phys. Rev. B, in print
- I. P. KRUG, F. U. HILLEBRECHT, M. W. HAVERKORT, H. GOMONAY, A. TANAKA, L. H. TJENG AND C. M. SCHNEIDER, *Magnetic coupling in highly-ordered NiO/Fe₃O₄(110): Ultrasharp magnetic interfaces vs. long-range magnetoelastic interactions*, Europhys. Lett., **81** (2008) 17005. *Contains part of this thesis.*

submitted

- I. P. KRUG, F. U. HILLEBRECHT, M. W. HAVERKORT, A. TANAKA, L. H. TJENG, H. GOMONAY, A. FRAILE-RODRIGUEZ, F. NOLTING, S. CRAMM AND C. M. SCHNEIDER, *Impact of the interface orientation on the magnetic coupling in highly ordered systems - a case study of the low-indexed Fe₃O₄/NiO interfaces*, submitted to Phys. Rev. B. . *Contains part of this thesis.*

other

- I. P. KRUG, F. U. HILLEBRECHT AND F. NOLTING, *PEEM Imaging of Antiferromagnetic Domain Walls in Single Crystalline Nickel Oxide*, SLS Annual Reports (2003)

Conference contributions

- DPG Frühjahrstagung 2005 (poster): *EXAFS Untersuchungen der Festphasen-Löslichkeit von Mn und Fe in epitaktischen Ge-Filmen auf GaAs (EXAFS investigations on the solid-state solubility of Mn and Fe in epitaxial Ge-layers on GaAs)*, I. P. KRUG, H. BRAAK, HILLEBRECHT, F. U., S. CRAMM, R. R. GAREEV, M. BOESE, M. LUYSBERG, D. RATA, D. E. BÜRGLER, K. CLEMENTIEV AND C. M. SCHNEIDER
- ICMFS 2006 & SNI 2006 (poster): *Competition of interface exchange- and magnetoelastic coupling in Fe_3O_4 -NiO and -CoO*, I. KRUG, F. U. HILLEBRECHT, H. GOMONAY, F. NOLTING, A. FRAILE-RODRIGUEZ, AND C. M. SCHNEIDER
- DPG Frühjahrstagung 2007 (oral): *Borderline magnetism - magnetic proximity effects at the highly ordered $Fe_3O_4(110)/NiO$ interface*, I. P. KRUG, F. U. HILLEBRECHT, H. GOMONAJ, M. W. HAVERKORT, A. TANAKA, L. H. TJENG AND C. M. SCHNEIDER
- VUV XV 2007 (oral): *Magnetic proximity effects at the highly ordered $Fe_3O_4(110)/NiO$ interface*, I. P. KRUG, F. U. HILLEBRECHT, H. GOMONAJ, M. W. HAVERKORT, A. TANAKA, L. H. TJENG AND C. M. SCHNEIDER

Awards

- 2003: price of the Savings Bank Foundation Kaiserslautern for excellent achievements in the diploma thesis